République Algérienne Démocratique et Populaire
Université de Blida 01
Faculté de Technologie
Département des Énergies Renouvelables

Thèse de Doctorat LMD

Spécialité : Énergies Renouvelables en Électronique

Stratégies de Contrôle pour l'Amélioration des Systèmes Micro-Réseaux

Par

AIT HAMMOUDA Camelia

Soutenu publiquement devant un jury composé de :

HAMID Abdelkader	Professeur	USDB 1	Président
HAFAIFA Ahmed	Professeur	UZAD	Examinateur
CHEGGAGA Nawal	Professeur	USDB 1	Examinateur
BRADAI Rafik	Professeur	USDB 1	Directeur de thèse
BOUKENOUI Rachid	MCB	USDB 1	Co-directeur de thèse

Blida,2024

People's Democratic Republic of Algeria
University of Blida 01
Faculty of Technology
Renewable Energies Department

LMD Doctoral Thesis

Specialty: Renewable Energies on Electronics

Control Strategies for Improving the Performance of Micro-grid Systems

By

AIT HAMMOUDA Camelia

Defended in public ahead of a jury composed of:

HAMID Abdelkader	Professor	USDB 1	President
HAFAIFA Ahmed	Professor	UZAD	Examiner
CHEGGAGA Nawal	Professor	USDB 1	Examiner
BRADAI Rafik	Professor	USDB 1	Thesis Supervisor
BOUKENOUI Rachid	MCB	USDB 1	Thesis Co-Supervisor

Blida,2024

Abstract

A Microgrid (MG) is commonly described as a distribution network operating at low or medium voltage levels, comprising various Distributed Generation (DG) sources, energy storage elements, and controllable loads. The majority of DG sources rely on Renewable Energy Sources (RESs) like wind and photovoltaics (PVs). MGs are designed to connect/disconnect to/from the main grid as needed. Typically, these MGs are managed using a hierarchical control structure with primary, secondary, and tertiary control levels. Two levels can be further distinguished within the primary control. The first level, also referred to as the inner control or zero level, includes an external voltage control loop and an internal current control loop, tasked with maintaining the power stage's voltage and frequency within desired references. The second level, known as power-sharing control, is responsible for sharing power among multiple parallel-connected converters feeding a common load. During this stage, the MG's key parameters, such as: frequency and amplitude, may deviate; hence, the role of the secondary level is to restore them to their nominal values, facilitating synchronization with the grid. The tertiary, being the last level, plays a crucial role in regulating power flow between the MG and the main grid. The present thesis focuses on the design, modeling, analysis, and control of parallel-connected three-phase VSIs within an AC MG system, specifically on the design of the Photovoltaic MG (PVMG) system based on the hierarchical control. It involves the design of advanced control schemes, developing accurate modeling approaches, and providing systematic guidelines for tuning the parameters of the proposed controllers. Additionally, it covers the adaptation stage, involving the DC-DC converter with a Maximum Power Point Tracker (MPPT) controller, between the PV Generator (PVG) and the inverter. The main objective of these approaches is to ensure effective and optimal control of the PVMG. Simulations and tests are conducted to validate the performance of the proposed control strategies for three-phase PVMG, demonstrating their effectiveness in achieving frequency and amplitude references, restoration, seamless synchronization, and optimal power flow control under various operating conditions.

Keywords: Three-Phase Microgrid (MG), Hierarchical Control, Controlled VSI, Modeling, Tuning Procedure, Photovoltaic (PV) System.

Résumé

Un Micro-réseau (MR) est communément décrit comme un réseau de distribution fonctionnant à des niveaux de tension basse ou moyenne, comprenant diverses sources de génération distribuée, des éléments de stockage d'énergie et des charges contrôlables. La majorité des sources reposent sur des sources d’énergie renouvelable telles que l'éolien et le photovoltaïque. Les MR sont conçus pour se connecter/déconnecter du réseau principal selon les besoins. Généralement, ces MR sont gérés à l'aide d'une structure de contrôle hiérarchique avec des niveaux de contrôle primaire, secondaire et tertiaire. Deux niveaux peuvent être distingués au sein du contrôle primaire. Le premier niveau, également appelé contrôle interne ou niveau zéro, comprend une boucle de contrôle de tension externe et une boucle de contrôle de courant interne, chargées de maintenir la tension et la fréquence de l’étage de puissance dans les références désirées. Le deuxième niveau, connu sous le nom de contrôle de partage de puissance, est responsable de la répartition de la puissance entre plusieurs convertisseurs connectés en parallèle alimentant une charge commune. Pendant cette étape, les paramètres clés du MR, tels que la fréquence et l'amplitude, peuvent dévier ; donc, le rôle du niveau secondaire est de les ramener à leurs valeurs nominales, facilitant la synchronisation avec le réseau. Le niveau tertiaire, étant le dernier niveau, joue un rôle crucial dans la régulation du flux de puissance entre le MR et le réseau principal. La présente thèse porte sur la conception et le contrôle d'un système MR AC, plus précisément sur la conception du système MG photovoltaïque basé sur le contrôle hiérarchique. Elle implique le développement de démarches de modélisation précises et la fourniture de directives systématiques pour ajuster les paramètres des contrôleurs proposés. De plus, elle couvre l'étage d'adaptation, impliquant le convertisseur DC-DC avec le contrôleur MPPT, entre le Générateur Photovoltaïque (GPV) et l'onduleur. L'objectif principal de ces approches est de garantir un contrôle efficace et optimal du MR PV. Des simulations et des tests sont réalisés pour valider les performances des stratégies de contrôle proposées pour le MRPV triphasé, démontrant leur efficacité dans l'atteinte des références de fréquence et d'amplitude, la restauration, la synchronisation sans faille et le contrôle optimal du flux de puissance dans diverses conditions de fonctionnement.

Mots clés : Micro-Réseau Triphasé, Contrôle Hiérarchique, Convertisseur Contrôlé, Modélisation, Procédure De Réglage, System Photovoltaïque.

ملخص

الشبكة المصغرة (MG) يتم وصفها عادة كشبكة توزيع تعمل على مستويات الجهد المنخفض أو المتوسط، تتألف من مصادر متوزعة متنوعة(DG) لتوليد الطاقة، وعناصر لتخزينها بالإضافة إلى أحمال قابلة للتحكم. تعتمد معظم مصادر التوليد DG على مصادر الطاقة المتجددة مثل الرياح والخلايا الشمسية. تم تصميم للاتصال/الفصل بـ/عن الشبكة الرئيسية حسب الحاجة. عادة ما يتم إدارة هذه الشبكات باستخدام هيكل تحكم هرمي مع مستويات تحكم أساسية وثانوية وثالثية. يمكن تمييز مستويين إضافيين داخل التحكم الأساسي، يتضمن المستوى الأول، المعروف أيضا باسم التحكم الداخلي أو المستوى صفر، الحلقة الخارجية للتحكم بالجهد والحلقة الداخلية للتحكم بالتيار، وهي مكلفة بالحفاظ على جهد وتردد الشبكة ضمن المراجع المرغوبة. في حين أن المستوى الثاني المعروف بموزع الطاقة، مسؤول عن توزيع الطاقة بين عدة محولات موازية تغذي حمولة مشتركة. خلال مرحلة التحكم الأساسي هاته، قد تنحرف المعلمات الرئيسية للشبكةMG ، مثل التردد وقمة الجهد، وبالتالي، فإن دور المتحكم الثانوي هو استعادتها إلى قيمتها المرجعية، مما يسهل مزامنة الربط مع الشبكة العامة. المتحكم الثالث، كونه المستوى الأخير، يلعب دورا حاسما في تنظيم تدفق الطاقة بين الشبكة المصغرة والشبكة العامة. تركز الأطروحة الحالية على تصميم متحكم في نظام الشبكة بتيار متناوب، وبالتحديد على تصميم نظام شبكة كهروضوئية مصغرة (PVMG)استنادا إلى التحكم الهرمي. تتضمن تطوير نهج النمذجة الدقيقة وتوفير الإرشادات النظامية لضبط معاملات المتحكمات المقترحة. بالإضافة إلى ذلك، تغطي مرحلة التكيف، التي تشمل محول مستمر-مستمر (DC-DC) مع المتحكم المراقب لنقطة الطاقة القصوى (MPPT)، بين المصدر والمحول. الهدف الرئيسي هو ضمان التحكم الفعال والأمثل للشبكة الكهروضوئية المصغرة ثلاثية الاطوار. تتم إجراء المحاكاة والاختبارات لتحقيق أداء الاستراتيجيات المقترحة للتحكم بـ PVMG، مما يظهر فعاليتها في تحقيق المراجع للتردد والجهد، الاستعادة، التزامن السلس والتحكم الأمثل في تدفق الطاقة تحت ظروف تشغيل مختلفة.

الكلمات الرئيسية: شبكة مصغرة ثلاثية الأطوار، تحكم هرمي، متحكم المحول، نمذجة، إجراءات ضبط المعاملات، شبكة كهروضوئية مصغرة.

Dedication

To my beloved parents ***Tarik*** and ***Fetta***, your unwavering love, boundless support, and endless encouragement have been the guiding light throughout my academic journey. Your sacrifices, both seen and unseen, have paved the way for my success. This thesis stands as a testament to your enduring belief in me and your dedication to my dreams. I am eternally grateful for all that you have done, and this work is dedicated to you with all my love and appreciation.

A special dedication goes to my loving brothers ***Aghiles*** and ***Koceila***, your support, encouragement and love have been my constant source of strength throughout this challenging journey.

To my dedicated advisor ***Pr. Rafik BRADAI***, whose guidance and expertise have shaped my research and intellectual growth. Your mentorship has been invaluable.

To my best friend ***Nour El Houda BOUGHEDAOUI***, who has shared in the ups and downs of this academic adventure. I will treasure our friendship forever.

To all my family members, I dedicate this work to each of you, with heartfelt gratitude and deep appreciation for all that you mean to me.

And finally, with self-appreciation and determination, I dedicate this work to myself, ***Camelia***. Through the challenges and triumphs of this journey, I have discovered my strength, resilience, and the boundless potential within me. This work stands as a tribute to the continuous pursuit of knowledge, self-improvement, and unwavering belief in my own capabilities. May this thesis contribute, in some small way, to the betterment of our understanding of the world.

With heartfelt gratitude and dedication,

Camelia AIT HAMMOUDA

Acknowledgment

In the name of ***ALLAH***, the Most Compassionate and the Most Merciful. I express my gratitude to ***ALLAH***, the ultimate source of knowledge in this world, for providing me with the strength and guidance to complete this thesis.

This research was conducted with the support of various institutions and individuals, and I am grateful to all those who have played a part in this academic journey. I would like to seize this moment to express my gratitude to all those who have offered their assistance in various capacities. Without their support, the completion of this thesis would not have been feasible.

First of all, I would like to express my deepest gratitude to my doctoral supervisor, ***Pr. Rafik BRADAI***, his expertise, patience, and dedication have been instrumental in shaping this thesis and in fostering my growth as a researcher. His assistance went beyond scientific guidance and extended to simplifying various administrative matters. I am deeply grateful for everything he has accomplished on my behalf.

And of course, my co-supervisor ***Dr. Rachid BOUKENOUI***, for his unwavering support, guidance, and mentorship throughout the course of my doctoral research.

I am indebted to the ***University of Quebec at Rimouski (UQAR)*** and my supervisor there ***Pr. Nourredine BARKA*** , as well as my colleague ***Dr. Abdellah BENALLAL*** for providing the resources, research facilities, and financial assistance that made this doctoral journey possible.

I would like to extend my appreciation to my fellow researcher ***Dr. Abdelhamid KHERBACHI*** at ***Renewable Energies Development Center (CDER)*** and his colleague ***Dr. Ahmed BENDIB***, whose collaboration and discussions enriched my understanding and contributed to the success of my research endeavors.

I am thankful to the members of my thesis committee, for their valuable insights, constructive feedback, and contributions to the development of this work.

I want to acknowledge the support of my parents who stood by me, offered encouragement, made sacrifices, and provided the necessary balance in my life during this demanding period. Their prayers and blessings were no doubt the true reason behind any success I have realized in my life.

Camelia AIT HAMMOUDA

Publications and Conferences

Conferences

- C. A. Hammouda, R. Bradai, R. Boukenoui, A. Kherbachi and A. Bendib, "Modeling and Design of Primary Control's Inner Loops for Droop-Controlled Three-Phase Inverters within a Microgrid System," *2023 International Conference on Advances in Electronics, Control and Communication Systems (ICAECCS)*, BLIDA, Algeria, 2023, pp. 1-6, doi: 10.1109/ICAECCS56710.2023.10105047.

- C. A. Hammouda, R. Bradai, A. Bendib, A . Kherbachi, R. Boukenoui and K. Kara, " ESOGI-Based Virtual Impedance Control Scheme with Performance Improvement for Droop-Operated Three-Phase VSIs in Islanded AC Microgrid," *2023 International Conference on Renewable Solutions for Ecosystems: Towards a Sustainable Energy Transition ICRSEtoSET)*, DJELFA, Algeria, 2023.

Publications

- AitHammouda, C., Bradai, R., Bendib, A., Kherbachi, A., Kara, K., Boukenoui , R., Ahmed, H.: Modelling, control design, and analysis of the inner control's loops intended for single-phase voltage-controlled inverter-based microgrid. IET Gener. Transm. Distrib. 18, 568–584 (2024). https://doi.org/10.1049/gtd2.13095

- Benallal, A.; Cheggaga, N.; Ilinca, A.; Tchoketch-Kebir, S.; Ait Hammouda, C.; Barka, N. Bayesian Inference-Based Energy Management Strategy for Techno-Economic Optimization of a Hybrid Microgrid. *Energies* 2024, *17*, 114. https://doi.org/10.3390/en17010114

Table of Contents

List of Acronyms

AC	Alternative Current
APF	Active Power Filter
AREP	Algerian Renewable Energy Program
CAGR	Compound Annual Growth Rate
CB	Circuit Breaker
CCL	Current Control Loop
CERTS	Consortium for Electric Reliability Technology Solution
CIGRE	Conseil International Des Grands Réseaux Électriques (International Council on Large Electric Systems)
CLB	Common Load Bus
CSI	Current-Source Inverter
DC	Direct Current
DER	Distributed Energy Resource
DG	Distributed Generation
DNO	Distribution Network Operator
DOE	Department of Energy
DSOGI	Double Second-Order Generalized Integrator
DSP	Digital Signal Processor
ESOGI	Enhanced Second-Order Generalized Integrator
ESS	Energy Storage System
EVs	Electric Vehicles
FF	Full Factor
FLC	Fuzzy Logic Control
FLL	Frequency Locked Loop
FP	Functional Point
FPGA	Field Programmable Gate Array
HMG	Hybrid Microgrid
HOGI	High Order Generalized Integrator
HV	High Voltage
HVAC	Heating, Ventilation and Air Conditioning
IEEE	Institute of Electrical and Electronics Engineers
IGBT	Insulated-Gate Bipolar Transistor
IGCT	Insulated-Gate Controlled Thyristors
KCL	Kirchoff's Current Law
KVL	Kirchoff's Voltage Law
LPF	Low-Pass Filter
LV	Low Voltage
MEG	Microgrid Exchange Group
MG	Microgrid
MOSFET	Metal-Oxide-Semiconductor Field-Effect Transistors
MPC	Model Predictive Control

MPP	Maximum Power Point
MPPT	Maximum Power Point Tracker
MSOGI	Multiple Second-Order Generalized Integrator
MV	Medium Voltage
n-SOGI	n-Order Generalized Integrator
P&O	Perturb and observation
PCC	Point Of Common Coupling
PE	Power Electronics
PI	Proportional–Integral
PID	Proportional-Integral Derivative
PIL	Processor In the Loop
PLL	Phase Locked Loop
PR	Proportional Resonant
PV	Photovoltaic
PVG	Photovoltaic Generator
PVMG	Photovoltaic Microgrid
PWM	Pulse Width Modulation
QSG	Quadrature Signal Generator
RES	Renewable Energy Sources
RMS	Root Mean Square
SC	Secondary Control
SG	Smart Grid
SMC	Sliding Mode Control
SOGI	Second-Order Generalized Integrator
STC	Standard Test Conditions
STS	Static Transfer Switch
TC	Tertiary Control
THD	Total Harmonic Distortion
TOGI	Third-Order Generalized Integrator
VCL	Voltage Control Loop
VI	Virtual Impedance
VIC	Virtual Impedance Control
VICL	Virtual Impedance Control Loop
VSC	Voltage Source Converter
VSI	Voltage Source Inverter

List of figures

Introduction

Chapter I

Chapter II

Chapter III

Chapter IV

List of tables

General Introduction

Context and research motivation

Due to the growing energy demand, global warming, along with the exponential limited availability of fossil fuels, the development of new production strategies by integrating Renewable Energy Sources (RESs) has become more than a necessity for the future of modern electrical systems[1]. In fact, the latter are complex and non-linear, and must supply the load at a constant frequency and constant voltage [2, 3]. The analysis and control of such a system are extremely difficult. Deploying a global control strategy on the current electricity grid is proving to be a real challenge. From here, the concept of Microgrid (MG) systems has been introduced by the Consortium for Electric Reliability Technology Solution (CERTS) by breaking down the network into interconnected sub-networks, and now they are gaining significant momentum.

Many nations have carried out the implementation of MGs in laboratories as well as real-world experiments. As shown in Fig.1 published by Statista research department [4], the global MG market reached a value of about 14.3 billion U.S dollars in 2021, up by 13% from the previous year. Between 2022 and 2028, the market is expected to expand at a Compound Annual Growth Rate (CAGR) of 17.9%, reaching a total value of 43.9 billion dollars. Exactly like other countries, Algeria's electricity market is constantly growing, and its current intention is to preserve and protect our planet. In relation to its potential, especially on solar energy, Algeria has implemented a national program AREP (Algerian Renewable Energy Program) that can be summarized in Fig.2, which was recently approved by the government and released by the Ministry of Energy. It intends to support Algeria's National Renewable Energy Development Strategy 2015–2030 objectives to diversify the energy mix, draw in private investment in the power industry, and maximize the country's high solar energy potential (2,000 kWh/m^2 annual average irradiation) to provide consistently 22,000 MW for the local market [5], with a goal of reaching a penetration rate of 40% based on renewable energy sources in order to decrease the use of traditional power plants.

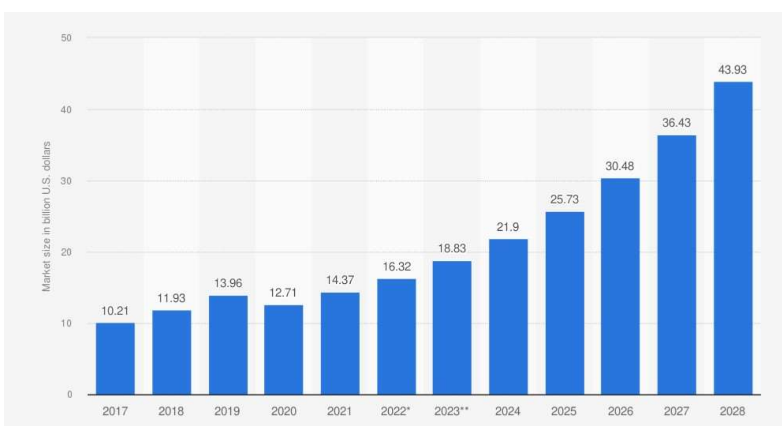

Fig. 1 : MG worldwide market size from 2017-2021, with forecast from 2022-2028[4].

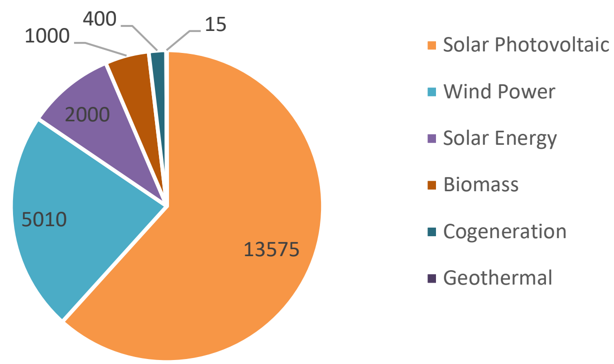

Fig. 2 : Algerian Renewable Energy Program from 2015-2030 [6] en MW

The MGs are small-scale electrical networks characterized by their localized power generation and distribution capabilities, designed to utilize Distributed Generation (DG) units with more efficiency and reliability. This offers a flexible and efficient solution for integrating RESs, and Energy Storage Systems (ESSs) and enhances the resilience of the power grid [7-9].

The majority of DGs, including microturbines, solar systems, and energy storage systems, need to be connected to the MGs and the utility grid at the Point of Common Coupling (PCC) through a Power Electronic (PE) interface enabling the seamless operation of MGs in both grid-connected and islanded modes[10] [11]. However, they could possibly expose the system to network disturbances because of their insignificant physical inertia [12, 13]. This PE interface can be a Voltage-Source Inverter (VSI) working in parallel to create isolated or autonomous MGs, or a Current-Source Inverter (CSI) used to inject current into the grid in grid linked mode. They serve as a significant component in converting DC power generated by RESs to AC power suitable for local loads. However, it is imperative to design an efficient and robust control system for the VSI to avoid possible MG problems [14], such as: power quality, stability, and reliability as well as achieving accurate power sharing and power flow among all kinds of sources. To this end, the regulatory bodies have set standards where a minimum requirement for electricity quality indicators (Total Harmonic Distortion (THD) rate, imbalance rate, etc.) is required.

To tackle the MG challenges, the design of control schemes for three-phase inverters in islanded or grid-connected AC MG systems has been the subject of extensive research. Most published works adopt a hierarchical control strategy, which consists of three control levels: primary, secondary, and tertiary [15, 16]. This strategy strikes a balance between decentralized, centralized, and distributed control structures[17]. The primary control can be further divided into two levels [1, 18]. The first level, also known as the inner control or zero level, is responsible for maintaining the voltage and frequency of the power stage at the desired references. It comprises an internal Current Control Loop (CCL) and an external Voltage Control Loop (VCL). The second level, known as power-sharing control, manages the power allocation among multiple parallel converters. Power-sharing methods are categorized based on their dependence on communication links. While the secondary and tertiary control levels are responsible for restoring the voltage and frequency to their nominal values and power flow, respectively.

Problem statement

As mentioned above, in order to meet the MG criteria for power quality, stability, and resilience, hierarchical control schemes modeling, and analysis have been widely used and developed.

Though a great deal of research into the design, modeling, and analysis of control strategies considering all control levels for both single- and three-phase MGs, the literature evaluation does not contain enough examples of efficient control structures that incorporate improved systems based on traditional PI regulators, and there still large gaps and difficult problems to overcome. Some of the main challenges related to MG hierarchical control modeling in three-phase MGs are as follows:

- Lack of proper tuning procedures for Proportional-Integral (PI) controllers, which are necessary for an accurate control process.
- Inaccurate Active and Reactive power sharing against various abnormal conditions (frequency, voltage variations, load changes, DGs connection/disconnection …)
- Difficult nominal parameters restoration achievement since the related associated estimations involve unknown dynamics.

Therefore, the present research work addresses these difficult concerns of developing, modeling, and parameter tuning of the primary, secondary, and tertiary control layers for three-phase MGs. Hence, MG's resilience and reliability may be increased by integrating an estimation scheme with improved performance. This will result in a system that can adapt effectively to changes in load demand and VSI outputs without sacrificing stability or performance. Additionally, effective evaluation of the stability of the MGs and the development of control strategies that can achieve the desired control transient performance may be ensured by the modeling approach development that makes it possible to derive correct mathematical models. The efficiency of the thesis proposal will be confirmed by the analysis and performance evaluation that have been presented along with the simulation outcomes that have been carried out.

However, the issue at hand is whether PVMG can operate steadily and robustly with improved performance using the proposed primary, secondary, and tertiary control schemes and the suggested modeling approach with inherent dynamics-based analysis.

Research objectives

Motivated by the issues and limitations faced by the DGs-based MG systems as mentioned above, this research provides a comprehensive study of these limitations, resulting in several key objectives:

- Improvement and development of DG-s based MG controllers.

- Addressing and solving problems related to the modeling and control of a VSI, specifically focusing on robustness and stability to ensure optimal power sharing among electrical loads with separate sources. Another major objective of this work is to operate DG units in a MG with fixed amplitude and frequency.

The operational objective of this work includes:

- Developing a precise mathematical model for designing the inner loop controller for voltage and current cascaded loops.
- Implementing a robust control method for the inner loop to ensure reference tracking, disturbance rejection, and noise suppression while guaranteeing system robustness margins.
- Applying a control method for the primary loop that accurately ensures power-sharing under various operating conditions, along with key functionalities such as fixed-frequency operation, rapid dynamic response, compatibility with the resistive nature of the grid impedance, and a simple control structure.
- Developing a secondary control based on the DESOGI-FLL to restore voltage amplitude at the PCC.
- Investigating the synchronization between the DGs and the utility grid.
- Designing a tertiary control level to ensure a stable power flow in three-phase MGs.
- Applying the proposed hierarchical control to a PVMG system to confirm its reliability.

Research contributions and outcomes

This thesis presents a viable and efficient solution for designing, analyzing, and modeling the hierarchical control layers of a three-phase MG based on the droop method during both islanded and grid-connected modes. Furthermore, it outlines a systematic and efficient methodology for tuning the parameters of their controllers. The effectiveness of the proposed control strategies is assessed through simulation studies covering diverse operational scenarios. Additionally, the PVMG system is performed to validate the efficacy and resilience of the proposed control approach. The specific key contributions of this thesis are outlined as follows:

For primary

- Mathematical modeling and systematic design of the LC-filtered inverter, as well as VCL and CCL models.
- Providing a detailed guideline for proper parameters' tuning of PI controllers.
- Stability examination and analysis of system behavior, considering settling time and variations in system parameters.
- Investigating the benefits and impacts of decoupling and compensation terms on VSI control response.
- Proposing an ESOGI-based virtual impedance control scheme for improving the power-sharing among droop-operated three-phase inverters.
- Simulation and results evaluation under various scenarios.

For secondary

- Proposing a secondary control framework based on an enhanced estimation method (DESOGI-FLL) for three-phase droop-controlled VSIs in islanded MG.
- Suggesting the Frequency-Locked Loop (FLL) linearized model as a model for frequency estimation, serving as feedback in the frequency restoration control loop.
- Conducting a comprehensive and effective guideline for proper parameter tuning of the secondary PI regulators.
- Evaluating the resilience of the designed controller under numerous variations in load and disturbances in system parameters based on the obtained models.
- Investigating control design and synchronization modeling, facilitating a smooth switch from islanded mode to grid-connected mode operation.

For tertiary

- Designing a tertiary control for three-phase MG based on DESOGI-FLL.
- Introducing a calculation block to achieve the best active and reactive power control.
- Investigating grid-tied mode for the proposed tertiary control.
- Checking the tertiary controller's resistance to different types of disruptions.

While the general contribution was the evaluation of the whole model's accuracy and stability under various case studies for PVMG.

Thesis organization

Along with the general introduction, where the work problematics, objectives, and outcomes were presented, the remainder of this thesis is organized as follows:

Chapter 01: introduces the MG technology and hierarchical control scheme; and gives an introduction to a survey of previous work concentrating on the hierarchical control layers design and modeling.

Chapter 02: describes the primary control scheme of a three-phase VSI-based MG. In addition, it provides the modeling, design, and analysis of VCL and CCL, along with their closed-loop models, considering the effects of compensation and decoupling terms. Then, the power- sharing loop based on ESOGI-FLL is provided in detail. Finally, it presents and discusses simulation and experimental results, and summarizes the main conclusions of the two first contributions of the thesis.

Chapter 03: explains the DESOGI-FLL scheme used to build the secondary control for two parallel connected VSIs in an islanded AC MG. Control design and modeling of synchronization loops are also covered in this chapter. In addition, it focuses on the modeling and design of the tertiary control layer in a three-phase AC MG to achieve optimal power flow. Last but not least, the chapter conclusions are provided, and the robustness of both secondary and tertiary controllers is validated using simulation implementations.

Chapter 04: is dedicated to the study of PVMG considering the hierarchical control studied in the previous chapters. Where the PV arrays connect to the DC bus through a DC-DC power converter modeled as a current source, driven by a Perturb and Observe (P&O) Maximum Power Point Tracker (MPPT) algorithm. For that, each component is discussed solely in this chapter. Furthermore, simulation tests are carried out to confirm the stability and resilience of the proposed control strategy.

Further discussion and conclusions of this thesis along with suggestions for future work are presented at the end of this research work.

Chapter I: Introduction to Microgrid Technology and Control

- Literature Review -

I.1 Introduction

In today's world, the growing implementation of conventional power generation facilities can be primarily attributed to the growth in global electrical energy demand. Simultaneously, the depletion of fossil and fissile resources, the imperative to reduce greenhouse gas emissions, and the drive to improve energy efficiency have become ever more pressing challenges [14, 19]. In this context, the integration of renewable energies [20] emerges as a transformative solution that is already in play within modern power grids, promising to reshape our future energy landscape. PV, wind, and hydroelectric energy have emerged as the three main RES, renowned for their environmental sustainability and inexhaustible nature. These RESs have experienced rapid technological development, making them not only clean (eco-friendly) but also affordable (economically feasible). This transition towards renewables enhances the energy security of countries, reduces dependence on fossil fuel imports, and extends electricity grid accessibility to remote and rural areas.

One notable advantage associated with the adoption of renewable energies is the transition from the conventional centralized production model to a decentralized one. DG units have become more common in recent years, and this has played an important role in integrating and improving the local use of various types of Distributed Energy Resources (DERs), providing important support to the large-scale power system. A major advantage of DG remains in its significant reduction of transportation costs. However, the extensive use of DG units also brings certain challenges for the distribution power grid, including issues related to power flows, voltage drops, and voltage fluctuations. In order to effectively handle these challenges, DG units are frequently clustered together into a basic building block what is known as a Microgrid (MG), an important concept that has been under consideration for several years ago and is attracting more and more attention.

MGs are gaining popularity due to their ability to improve the quality of the power supply system and address local energy issues, and thereby increasing overall flexibility. However, Energy Storage Systems (ESSs) are integrated into the system to deliver continuous power to the loads despite the stochastic behavior of the RES [21]. Moreover, as depicted in Fig.I.1, these networks typically include loads as well as protection and control equipment that can operate in two fundamental modes: islanded and grid-connected modes [22]. For instance, the ability to intentionally island is advantageous when, for example, the grid experiences a fault because the MG can continue to function due to the availability of numerous DGs and ESSs [21] to ensure that the loads are always supplied. Furthermore, different types of common buses may allow the existence of AC, DC or hybrid, MGs [23].

In fact, due to the stochastic behavior of the prime mover, such as the sun and wind [24], it is becoming more challenging to deliver constant power in response to the demands of the loads when the power generation is not constant. Consequently, Power Electronics (PE) interfaces have been used in connecting DGs to both MG and the main grid, offering more flexible operation and control. These PE interfaces can take the form of a Current-Source Inverter (CSI) used to inject current into the grid when operating in grid-connected mode, or a

Voltage-Source Inverter (VSI) when operating in parallel in established autonomous or isolated MGs. However, it's important to note that, owing to their negligible physical inertia, they can make the system potentially vulnerable to network disturbances. Additionally, by employing the appropriate control measures, such as compensating for voltage harmonics [25], it is feasible to enhance the power quality.

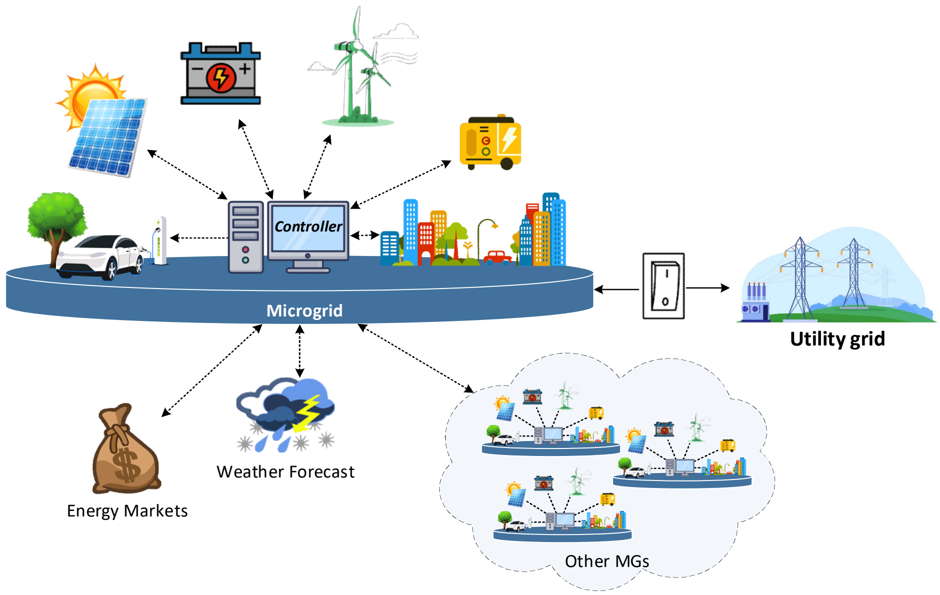

Fig.I. 1 Typical Microgrid Structure

Building upon this brief introduction, this chapter gives some basic and essential concepts related to MG systems. It provides detailed descriptions of its definitions, advantages, and evolution, delves into various MG architectures and components, and states a survey review on control methods for both MGs and DGs as documented in the literature. Special emphasis is placed on the hierarchical control of MGs including primary, secondary, and tertiary control levels as well as the considered challenges and problem statement related to frequency and voltage control, along with power management issues.

I.2 Microgrids definition

A MG has been given a number of definitions; the most significant ones are mentioned in Table I.1.

Table I. 1 Microgrid definitions

Reference	Definition
IEEE standard 2030.7 [26] and the Microgrid Exchange Group (MEG) of the federal U.S. Department of Energy (DOE) [14],[27]	A group of interconnected loads and DERs within clearly defined electrical boundaries that acts as a single controllable entity with respect to the grid. A microgrid can connect and disconnect from the grid to enable it to operate in both grid-connected or island mode.
[14],[28],[29]	A typical hybrid electric network comprising DERs, local loads, and ESSs for supplying power to specific areas or

	remote localities. The main function is to ensure the system's stability under different network faults.
[16]	A small-scale power grid that consists of DERs, loads, and controllers. One of the major advantages of an MG is that it can operate in grid-connected or islanded modes that can generate, distribute, and regulate the power flow to local consumers.
International Council on Large Electric Systems (Conseil international des grands réseaux électriques) CIGRE [15],[30]	Sections of electricity distribution systems containing loads and DERs (such as DGs, storage devices, or controllable loads) that can be operated in a controlled, coordinated way, either while connected to the main power network and/or while islanded
[31]	A network of low voltage power generating units, storage devices and loads capable of supplying a local area such a suburban area, industry or any commercial area with electric power and heat.

A MG is therefore defined as a small network fed by groups of small capacities through DGs, including PV power plants, micro-wind turbines, diesel generators...etc. It is clear that all these definitions only took into account the physical layer of an MG when one considers that an MG has cyber (communication), control, and physical levels.

A significant adoption of MGs holds substantial promise for the future, aligning with the idea of a smarter, more effective, dependable, and technologically advanced grid, dubbed a "Smart Grid" (SG) [32]. Furthermore, when it comes to a small electrical domain connected to the grid of no greater than 100 kW and limited to a single building structure or primary load or network of off-grid loads not exceeding 5 kW, both categories representing devices (such as DG, batteries, Electric Vehicles (EVs), and smart loads) capable of islanding and/or energy self-sufficiency through some level of intelligent DER management or controls, we are talking about a Nanogrid, which is a term originated by Lawrence Berkeley National Laboratory.

I.3 Microgrid advantages

MGs offer numerous advantages; to local and distribution systems; over traditional distribution systems, making their study and investigation imperative. The most significant benefits are outlined in Table I.2 [14],[16].

Table I. 2 MG advantages

Advantage	Explanation
Stability enhancement	Due to MGs' unique characteristics, main grid stability can be increased by integrating MGs into the system.
Efficiency increase and faster response	All generators are controlled as dispatched sources, situated close to the customers, which lowers the need for complex transmission systems [33], and consequently reduces transmission and distribution lines losses .

Higher RESs integration	RESs are low-carbon technologies, as a result, the potential for fuel use decreases, thereby reducing CO2 emissions and contributing to the mitigation of global warming and pollution.
Continuous loads supply in islanded mode	Unlike conventional distribution systems, MGs can offer loads during their autonomous/islanded mode a continuous and independent supply.
Reliability and power quality improvement	Supporting the local power grid and facilitating the generation increase, allowing the use of flexible loads, and ensuring more precise matching of production and consumption [34]
Plug-and-play capability	MGs can switch seamlessly either to grid-tied or islanded modes.
Back-up supply source	Under the main grid's power supply failure, MGs can play the role of a backup supply source.
Increase security and tolerance to main grid failures	the ability to disconnect from the main grid during faults [15] while still maintaining the energy supply and *V/f* stability for all local loads by operating in the islanded mode [16].
Bidirectional power flow path	The idea of unidirectional power flow in the conventional distribution (from the substation to the load specified) can be transformed into a bidirectional structure.
Cost effective way	To facilitate rural electrification, as no main power system is needed to operate the MG. The consumption price is optimized due to the design of several types of generators. Easy maintenance of MG devices

I.4 Microgrids classification

It is noteworthy that, depending on the papers in the literature, MGs can be in several ways. However, in terms of the DERs' connection way, they can be divided into three main types: parallel, cascaded (series), and hybrid cascaded–parallel MGs [35-38], respectively shown in Fig.I.2 [39]. In addition, in terms of their voltage level, MGs are classified into Low Voltage (LV), Medium Voltage (MV), and High Voltage (HV) systems. Further, MGS may also be single or three-phase systems.

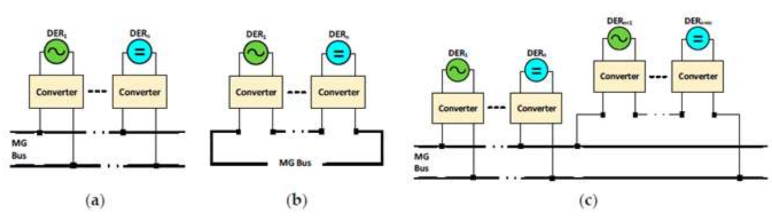

Fig.I. 2 Simple diagrams of different MG structures (a) parallel (b) cascaded (c) hybrid

Besides the aforementioned classifications, according to their current type (direct and alternative) and manner of linking at the PCC [31], MGs are divided into three types: AC MGs, DC MGs, and Hybrid MGs (HMGs) or AC/DC MGs [40, 41], In the next subsections, each type is subjected to a detailed investigation of its unique characteristics and viability.

I.4.1 AC microgrids

The typical structure of an AC MG (AC MG) is illustrated in Fig.I.3. It features a common AC bus connecting various components of the MG and linking to the main utility grid through the Point of Common Coupling (PCC). This design facilitates the integration of DGs into the conventional AC main grid without requiring significant modifications, enhancing controllability and flexibility compared to other types of MGs [42].

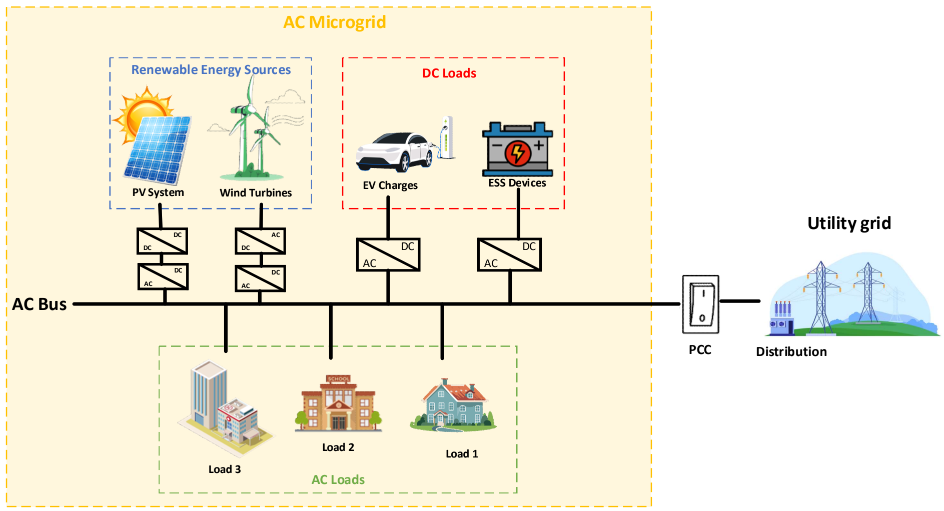

Fig.I. 3 Schematic diagram of a typical ACMG

With this configuration, achieving a high level of fault management capability is feasible, thanks to a wide range of available protection mechanisms. Additionally, voltage levels can be conveniently adjusted using low-frequency transformers. AC MGs are expected to fulfill various tasks and objectives, including frequency and voltage regulation for DG units, improving power quality, managing active and reactive power flow, system recovery, energy management, and grid synchronization [43].

However, MGs' ability to operate both connected (i.e., with the utility grid) and disconnected poses a challenge in ensuring seamless transitions between these operating modes. Additionally, the need for synchronization and the circulation of reactive power, leading to losses in the network grid, can be downsides for this type of MG.

In this architecture, electronic power grid-tied inverters (DC/AC converters) are commonly used to interface between DC RES and/or storage devices and the AC common bus [44], which may reduce the overall system efficiency [45-47]. Moreover, connecting DG units in parallel increases the overall system complexity and may present challenges related to system stability.

I.4.1 DC microgrids

In the context of DCMG topology, depicted in Fig.I.4, a common DC bus interconnects its various components. They are linked to the primary grid via a DC/AC power converter. This structure is capable of supplying both DC and AC loads at varying voltage levels through power electronic devices. DCMGs offer an economical and more efficient alternative to AC systems, as they eliminate the need for synchronization and reactive power production/circulation [45, 48-50]. This design facilitates a high penetration of DC DERs like PV systems and fuel cells [45, 48-50]. Additionally, DCMGs exhibit reduced power conversion losses, requiring fewer power conversion stages, resulting in improved efficiency, cost-effectiveness, and a smaller footprint. Common DCMG structures include bipolar, monopolar, and homopolar configurations [46, 51]. In terms of operational principles, DC and AC MGs share similarities. Nonetheless, the protection protocol of the DC MG network poses a formidable obstacle.

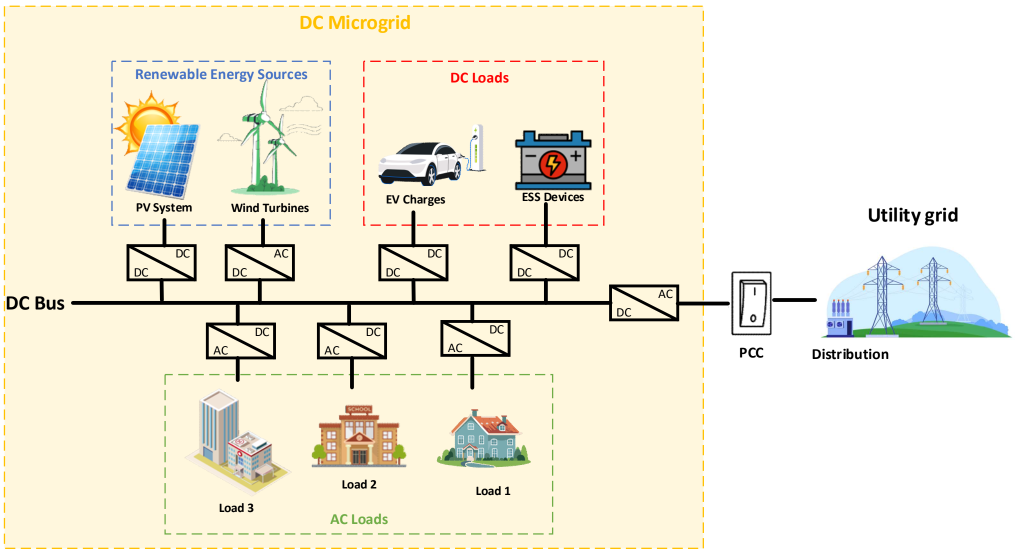

Fig.I. 4 Schematic diagram of a typical DCMG

I.4.2 Hybrid AC/DC microgrids

The HMG, shown in Fig.I.5, is the result of merging ACMGs and DCMGs within a unified distribution system, thus combining their respective attributes and benefits, such as a reduced number of interface devices, facilitated DER integration, fewer conversion stages, diminished power losses, cost savings, and heightened reliability. It was designed to enhance the connectivity of DC MGs with the AC electrical network, thereby contributing to overall network development. In this structure, AC and DC components, including DGs, ESSs, and loads, can be directly integrated and connected to AC and DC buses, eliminating the need for synchronization in generation and storage units [42, 52, 53]. However, it's worth noting that, as previously mentioned, the protection of the DC MG network remains a concern. Furthermore, managing such a configuration proves to be more complex due to the control requirements of devices linked to both the AC and DC networks and the interface power converter [54].

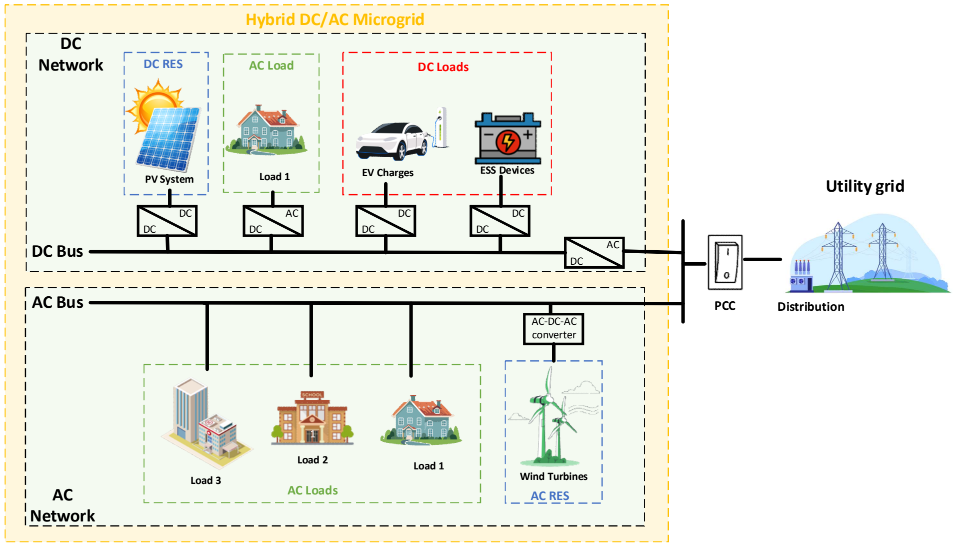

Fig.I. 5 Schematic diagram of a typical HMG

Due to the ease of integration within the existing transmission network, in this project, the focus is on the AC MGs

I.5 Architecture / structure of a Microgrid

In academic literature, various structural frameworks have been suggested for MGs. The most prevalent configuration is visualized in Figs.I.3-I.5. In this structure, RES, such as PV panels, micro-turbines, fuel cells, and diesel generators, serve as electricity sources for the load. However, to ensure a consistent power supply despite the variable nature of RESs, ESSs are incorporated into the system. The energy sources are connected to a singular electrical interface point, called the PCC, through electronic power converters. This allows power to flow as required, either to the loads, storage systems, or the grid, depending on the MG's power production and demand. MGs can be disconnected from the distribution system, typically facilitated by a singular protective switch. Centralized control systems often oversee MG management. Each component is thoroughly examined in subsequent subsections.

I.5.1 Prime movers

They are energy sources, and they highly depend on geographic conditions and resource availability. Geographic factors influence the use of RESs, including options such as wind turbines, PV panels, and tidal or wave power, among others. Resource availability, on the other hand, dictates the use of non-renewable energy sources, such as diesel generators, fuel cells, microturbines, and more.

I.5.2 Loads

They may vary depending on the magnitude of power required, whether for residential, commercial, or industrial use. Another distinguishing factor is the imperative need for uninterrupted electricity supply, with notable distinctions between a private home, a medical facility like a hospital, or a critical data center. In the context of healthcare, a constant power supply is vital to ensure patient care and surgical procedures, while in the case of a data center, any power outage could lead to the loss of vital and sensitive data.

Additionally, loads can be categorized based on their linearity. A non-linear load is one that exhibits changes in its impedance concerning applied voltage, resulting in the presence of harmonics within the load's current waveform. Even when connected to a sinusoidal voltage source, these non-linear loads produce non-sinusoidal current waveforms. Furthermore, these harmonic currents can interact with the grid's impedance, ultimately causing voltage distortions [9].

I.5.3 Control Unit

The effective operation of a MG relies on the seamless coordination of its system components, ensuring compliance with various constraints. One essential part of this is the individual inverters operating in parallel within the MG. These inverters share the total electricity demand fairly and prevent overloads. of DGs. Additionally, they facilitate the power exchange within the MG, as well as between the MG and the main power network. This control process is instrumental in guaranteeing the stable, reliable, and safe operation of MG.

A critical piece of hardware that helps coordinate all of this is called the control unit. Depending on the MG's needs, this control unit can be a Digital Signal Processor (DSP) or a Field Programmable Gate Array (FPGA). The choice depends on how big the MG is, how complex the control tasks are, and how much computational power is needed for it to work properly.

There are three fundamental configurations for inverter controls, referred to as [5, 6]:

a) Grid-forming: This design functions as a constant voltage provider, establishing a reference voltage and frequency value through a well-regulated control system. In standalone mode, it is essential to have at least one source utilizing grid-forming control within the MG.

b) Grid-feeding: Its primary function is to extract the maximum active power from the primary energy source.

c) Grid-supporting: This unit adjusts its active and reactive power output based on power distribution strategies and is adaptable to variations in frequency and voltage brought about by changes in the load profile.

In MG contexts, it is important to blend the grid-forming and grid-supporting configurations to enable inverters to function in parallel. Droop control mechanisms can deliver steady sharing of active and reactive power when interacting with other voltage or current sources, or they can produce consistent active and reactive power output in parallel with a fixed voltage source. Further elaboration is provided in the subsequent subsection.

PE converters comprise various controlled and uncontrolled switches, typically diodes for uncontrolled switches and Insulated-Gate Bipolar Transistors (IGBTs), Metal-Oxide-Semiconductor Field-Effect Transistors (MOSFETs), Insulated-Gate Controlled Thyristors

(IGCTs), etc., for controlled switches. These switches, along with passive elements like capacitors and inductors, shape the output AC voltage. By manipulating these switches, the converter's output voltage waveform is controlled, resulting in different converter topologies based on switch disposition and arrangement.

I.5.4 Protection System

Considering the emergence of distributed energy sources in medium- and low-voltage networks and the transition from a historically radial distribution system, characterized by unidirectional power flow from substations to end-users through transmission and distribution lines, to a more dynamic and bidirectional power flow system, the need for an essential shift in protection mechanisms becomes evident. This evolving landscape has given rise to the development of innovative protection approaches, making it a central focus of current research endeavors, as indicated in the existing literature [55].

I.6 Microgrid Operation Modes

After analyzing the fundamental characteristics of a MG, it is interesting to examine how it interacts with the primary grid while supplying critical loads. Essentially, it can function either connected to the grid or disconnected from it, commonly termed grid-connected mode, and islanded mode, respectively [56, 57].

Moreover, the transition between these operational modes can be executed seamlessly. This flexibility is made possible through a clever switch called a Static Transfer Switch (STS). This switch can intelligently determine, by assessing the conditions of both the grid and the MG through feedback measurements, whether it's appropriate for the MG to be connected to the main power network or not [58] .

I.6.1 Islanded Mode

In islanded mode, MGs operate independently, without being connected to the main power grid, which means the main grid doesn't affect them. However, this mode involves more complex control because the MG has to take on roles usually handled by the main grid. Firstly, DGs have to manage their voltage and frequency independently, based on their local information, making sure they stay within specified limits (typically ± 5% for voltage and ±2% for frequency). Secondly, they need to meet the active and reactive power balance between power supply and demand [59, 60], avoiding overproduction or underproduction. ESSs can help in case of overproduction or mismatch, but underproduction can lead to voltage drops, causing power outages or even blackouts. Lastly, the MG must also ensure power quality, which is crucial for the proper operation of connected devices. If the supplied voltage doesn't meet the specified limits for voltage and frequency and has excessive distortion (THD exceeding 5%), the loads may malfunction, wear out prematurely, or not work at all. Additionally, the MG components need to communicate effectively [43, 61].

Islanded operation mode can be quite beneficial in various situations. It's especially useful in remote areas that are hard to reach or where the distance from the main power grid is so great that connecting to it would be too expensive compared to the potential earnings for the

Distribution Network Operator (DNO). In such cases, running independently is the best way to provide electricity to customers [30].

Another important scenario where islanded operation is not just advantageous but also essential is when a grid fault happens. In this situation, the smart switch STS continuously monitors the grid status. When it detects an unusual condition, it disconnects the MG from the main grid, ensuring a continuous power supply to local users and safeguarding distributed generators and storage systems. This not only enhances grid reliability but also reduces the number of consumers affected by voltage outages. It's important to note that the STS initiates the switching operation mode not only during faults but also when the grid is weak, ensuring the necessary power quality and without disrupting the MG's stable operation, for the smooth operation of the connected devices [31].

However, due to differences in power line properties (impedances), voltage levels, or local energy demand [22], the challenges in this mode arise when it comes to distributing power among multiple DG units.

I.6.2 Grid-Connected Mode

When MGs are connected to the grid, they can either act as a controlled power consumer or a controlled power supplier. This means they can either draw electricity from the main grid or provide power to the local distribution network. In this mode, the voltage and frequency settings at the PCC are managed by the main grid, and it also imposes the flow of active and reactive power within the MG through communication channels. Therefore, the primary responsibility of the MG is to manage its power output in a way that maximizes local power generation, reducing the reliance on grid-supplied electricity [62]. This, in turn, eases the load on the distribution grid, leading to decreased energy transmission losses.

I.7 Microgrid control

There are two main categories of controlling MGs: centralized [11]and decentralized [12]. due to the presence of different types of loads at the distribution and high penetration of renewable energies. the stability of the operation of the MGs is ensured by the realization of the main points [7-12]:

- Voltage and frequency regulation.
- Adequate sharing of power between decentralized production systems (DGs).
- Resynchronization of the mg with the main grid.
- Control of the energy flow between the mg and the main grid.
- Optimize the operating cost of MG.
- Correct regulation of transitional regimes and restoration of desired conditions when changing mode

Several control strategies have been suggested in order to satisfy the requirements cited, each one with its advantages and drawbacks, the most used are detailed in the following subsections.

I.7.1 Centralized And Decentralized Control Approaches

In the past, the standard way of managing energy was centered around using fossil fuels like coal, oil, and gas, or nuclear power. It was made based on a centralized approach; it considers two main aspects: information flow and energy flow. When it comes to information flow, a central controller receives data about electricity consumption through high-speed communication. It does all the calculations and directs power sources on how much electricity to produce in order to maintain a balance [10]. Regarding energy flow, electricity flows from power plants to end users through a network of transmission and distribution systems.

On the other hand, in decentralized control, each power source has its own controller that makes calculations and gives control commands based on local measurements, without knowing the other units' actions [10]. However, some level of communication is still required to coordinate the operations of the inverters [13].

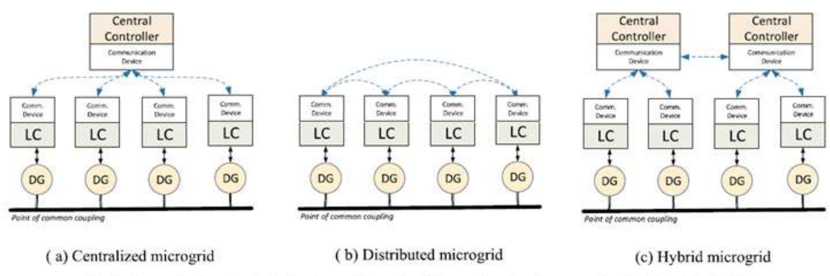

Fig.I. 6 Different MG control topologies

I.7.2 AC Microgrid Hierarchical Control

One common method for monitoring the operation of developed AC MGs is a hierarchical control structure. It serves as a compromise between fully decentralized and fully centralized approaches. This control structure consists of three levels: primary, secondary, and tertiary, as suggested in [43]. The provided Fig.I.7 illustrates the multilevel hierarchical control with brief descriptions of the key responsibilities at each control level.

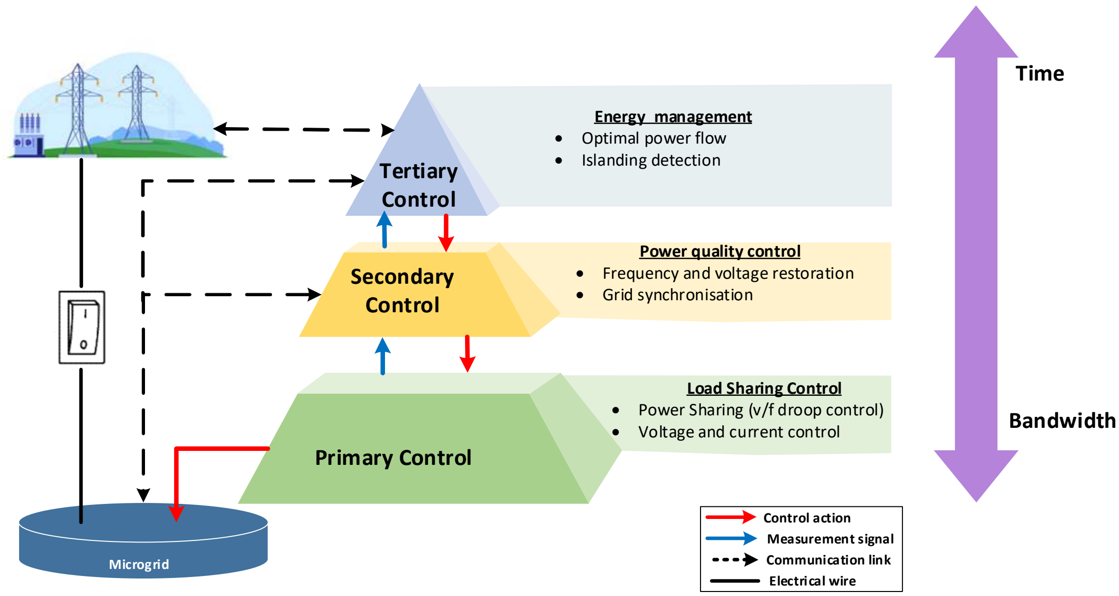

Fig.I. 7 Simplified diagram of multilevel hierarchical control.

It's important to note that all these tasks need to be managed concurrently, even though they operate on different timescales. For example, tasks like frequency and voltage regulation, power-sharing, and island detection must be addressed almost instantly (within a few milliseconds) due to the rapid response of power converters. On the other hand, tasks related to power quality may take a few milliseconds to a minute. Power dispatch can be managed within a few minutes, while economic dispatching and market participation typically occur on timescales ranging from a few minutes to an hour. Additionally, this approach allows for supervisory control over lower-level systems without compromising stability and robust performance. Consequently, the control bandwidth should decrease as you move up the control hierarchy [63].

The hierarchical control as a whole relies on local measurements made by the primary control at the PCC or Circuit Breaker (CB). These measurements include voltage and current at each converter's output. It's worth mentioning that the simplified architecture shown in the given figure can be improved by introducing further parameters like total harmonic distortion [64] or voltage unbalance factor [65] to handle power quality issues, or temperature sensor signals to regulate the HVAC (Heating, Ventilation and Air Conditioning) system [66-68]. Many hierarchical control approaches have been provided in the literature, including the traditional PI-hierarchical control [69], hierarchical multi-agent systems [70, 71], hierarchical predictive control [72, 73], and stochastic hierarchical control [74, 75].

The hierarchical control system, as depicted in Fig.I.8, includes the three control levels for AC MGs with parallel-connected VSIs, operating in grid-connected and islanded modes. The primary control layer is designed for decentralized operation, ensuring power sharing among DG units and MG stability. It often relies on a droop control approach to achieve a proper and fast power balance in a decentralized manner [76-82]. However, the primary control based on droop has its limitations, leading to voltage and frequency deviations, as well as imprecise reactive power sharing among DG units [43], [83], [84].

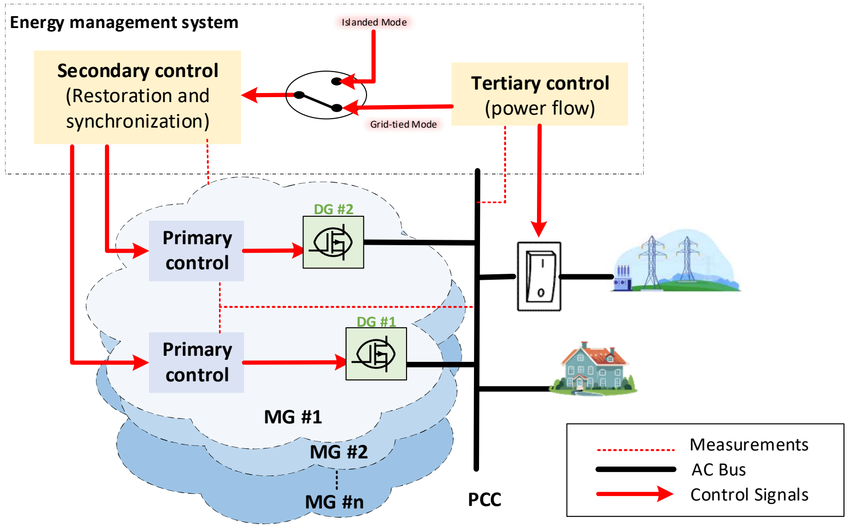

Fig.I. 8 Schematic diagram of AC MG hierarchical control

To address these issues, the secondary control layer, whether centralized or distributed, is introduced to rectify these deviations and enhance power quality by restoring MG voltage frequency and amplitude to their nominal set points. Additionally, the secondary control aims to synchronize the MG with the main utility grid before establishing the connection between them [85].

The tertiary control is typically centralized and functions as the slowest controller, primarily active when connecting the MG to the main grid. This level manages bidirectional power flow between the MG and the main grid, and it also includes islanding detection as part of its responsibilities [83]. It's worth noting that the term 'energy management system' refers to both the secondary and tertiary control layers. The subsequent subsections will provide an overview of the fundamental structures of each control level and a detailed description of their functions.

I.7.2.1 Primary Control / Local Control

In a MG system, the primary control level is the lowest in the hierarchy. Its main role is to manage any sudden changes in the power load [86] , whether those loads are linear or nonlinear. This control is local and decentralized, meaning it relies solely on local measurements with each inverter having its dedicated control stage, enabling each DG unit to function independently, without the need for communication during normal operation. It plays a crucial role in guaranteeing the reliability of the MG and enhancing its overall performance and stability [3,4]. It's responsible for adjusting the frequency and voltage output of inverters to serve as a reference for the inner multiloop controller. This helps reduce circulating currents that can occur when multiple converters are connected in parallel [15,16]. Additionally, it ensures the precise sharing of active and reactive power among these converters. It can function in both grid-connected and autonomous modes, with a seamless transition between them.

The control structure for this level, based on a single inverter unit, is depicted in Fig.I.9. This setup comprises two key components:

a) The cascaded inner loop, that compromises the current and voltage control loops, which are responsible for stabilizing the inverter voltage frequency and amplitude.

b) The external power control loop based on the droop control method, along with a virtual impedance loop and a power calculation block. Meanwhile, the droop control is for controlling the active and reactive power outputs of the DG.

As depicted in Fig.I.9, before droop control was put into place, the power calculation stage utilizes the filter output currents and voltages, which are transformed into the αβ-frame and detected by the Second-Order Generalized Integrator-Frequency Locked Loop (SOGI-FLL), to compute the average values of real and reactive power.

Dealing with mismatched inductive/ resistive feeder impedance, the optional virtual impedance loop improves power quality and power-sharing accuracy within the MG [87].

Further details about these components will be elaborated upon in the subsequent sections.

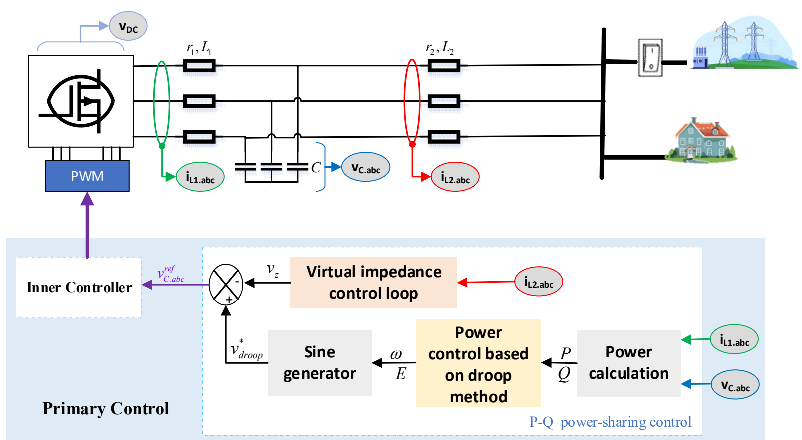

Fig.I. 9 Primary control configuration

a. Power Calculation Block

Adding the power calculation component to the main control setup plays a vital role in figuring out the average levels of active (P_i) and reactive (Q_i) powers. Generally, when dealing with three-phase MGs, they can easily be calculated by converting the three-phase voltages and currents (in *abc* frame) to the *αβ* (or *dq*) reference frame. This involves applying established equations such as in Eq. (I.1) as appropriate.

$$\begin{cases} P_i = \left(v_{c.\alpha} \times i_{L_2.\alpha} + v_{C.\beta} \times i_{L_2.\beta}\right) \\ Q_i = \left(v_{C.\beta} \times i_{L_2.\alpha} - v_{C.\alpha} \times i_{L_2.\beta}\right) \end{cases} \quad \begin{cases} P_i = \left(v_{C.d} \times i_{L_2.d} + v_{C.q} \times i_{L_2.q}\right) \\ Q_i = \left(v_{C.q} \times i_{L_2.d} - v_{C.d} \times i_{L_2.q}\right) \end{cases} \tag{I.1}$$

where $v_{C.\alpha\beta}$ ($v_{C.dq}$) and $i_{L1.\alpha\beta}$ ($i_{L1.dq}$) essentially stand for the in-phase and quadrature-phase aspects of both the inverter's output voltage and current.

Fig.I.10 illustrates the schematic designs for the power calculations for three-phase systems. After the determination of the instantaneous active and reactive powers, the data are processed through a Low-Pass Filter (LPF) to produce the corresponding average values.

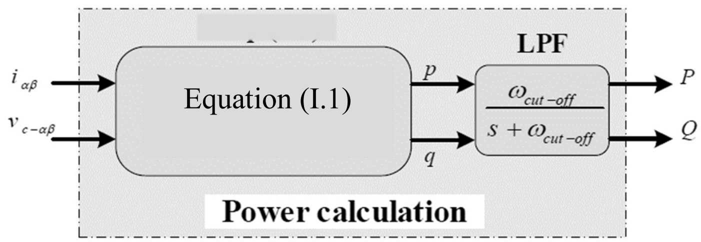

Fig.I. 10 Power calculation block diagram.

The LPF's transfer function ($G_{LPF}(s)$) can be described as follows in the s-domain:

$$G_{LPF}(s) = \frac{\omega_{cutt.off}}{s + \omega_{cutt.off}} \tag{I.2}$$

$\omega_{cutt.off}$ in this context is the LPF’s cut-off frequency. Usually, it is set to a relatively low value to get rid of any underlying harmonic components [66].

b. Droop Control Strategy

In AC MGs with multiple DG systems operating in parallel, ensuring optimal power sharing becomes a complex task. The goal is to allocate each DG its share of active and reactive power, meeting the overall load demand without overloading any particular DER. This should also maintain stable voltage and frequency levels, thus upholding MG stability.

In MG literature, centralized architectures are often considered to enhance power-sharing due to their accuracy and reduced voltage and frequency deviations. Two common centralized power-sharing strategies are the master-slave approach [88, 89] and concentration methods [90].

Additionally, there is a preference for controlling numerous parallel VSIs, while preventing the circulation of current among them [43, 77, 85, 91], in a distributed manner using droop control considered as the heart of the primary control [78, 79, 91-94]. This approach demands less external communication, relies on local measurements, and offers flexibility for various plug-and-play MG devices [43, 95-99]. Droop control is based on the principle of power flow in traditional power systems with parallel synchronous generators which distribute any load increases based on their rated capacities. When there's a sudden surge in power demand, it can be offset by the mechanical power of the rotor. This very same concept is utilized in the exciter control of synchronous machines, where the voltage decreases as reactive power rises. These principles are integrated into power electronic MGs through the use of droop functions [80, 100-102]. The droop control operates within a range of 100 milliseconds to 1 second. It assigns individual frequency and voltage setpoints to each inverter based on power-sharing needs. While effective in maintaining stability and power balance, it has limitations concerning voltage regulation and harmonic compensation. Various control schemes and configurations of droop control exist to enable efficient power sharing for both linear and nonlinear loads.

The conventional droop control, often referred to as $P-\omega$ and $Q-E$ droops, since it uses the Active Power/Frequency (P/f) control and Reactive Power/Voltage (Q/V) control to realize decoupling control of active and reactive power. A comprehensive review of droop control strategies is summarized in [82]. Further discussions about power-sharing control algorithms are detailed in [82]

However, DG systems often have different output impedances, which require specific adaptations of droop control. they can be resistive($R/inverters$), capacitive($C/inverters$), resistive-capacitive($RC/inverters$), or resistive-inductive($RL/$ $inverters$). It's reported in [10] that it is not feasible to operate an inverter with an inductive output in parallel with another inverter having a capacitive output. In most cases, the output impedance is inductive ($L/inverters$), especially around the fundamental frequency. Nonetheless, for low-voltage MGs, where the equivalent impedance between any two DG systems can be either resistive or inductive (with a DG coupling transformer or a grid side inductor), the impedance resistance R becomes essential and no longer be neglected [11].

This mechanism guarantees that DG units distribute the workload by tuning the frequency of each VSI according to the supplied real power. Consequently, each generator adjusts to variations in the overall load, adhering to its distinctive frequency droop characteristic, and all of this is achieved without the necessity for inter-unit communication. Similarly, a reduction in voltage amplitude (E) coupled with reactive power (Q) is utilized to facilitate the equitable sharing of reactive power.

In the droop control loop, the frequency (ω) and voltage amplitude (E) of the inverter output are set based on the average active power (P) and reactive power (Q) supplied by the VSI to the MG. To put it in simpler terms, these connections can be articulated as follows:

$$\begin{cases} \omega_i = \omega^* + m\left(P^* - P\right) \\ E_i = E^* + n\left(Q^* - Q\right) \end{cases} \tag{I.3}$$

Here, ω^* and E^* refer to the frequency and amplitude of the output voltage when there's no load. P^* and Q^* stand for the reference for active and reactive power, and during island operation mode [79], these references are set to zero.

The control parameters, represented by n and m, are linked to the inclines of the frequency and amplitude functions. These figures are established considering the allowed frequency and voltage deviations ($\Delta\omega$ and ΔE), along with the maximum active and reactive powers ($P_{\max}$ and $Q_{\max}$), respectively. This relationship can be expressed as follows:

$$m = \frac{\Delta\omega}{P_{\max}} \quad , \quad n = \frac{\Delta E}{Q_{\max}} \qquad \text{(I.4)}$$

Fig.I.11 represents the droop control loop block design. As shown, a sinusoidal signal generator receives the frequency and voltage produced by the droop controller. This generator is responsible for producing the reference output voltage ($v_{droop}^*(t)$) for the VSI. The relationship governing this can be expressed by the following equation:

$$v_{droop}^*(t) = E_i \times \sin\left(\omega_i \times t \begin{bmatrix} 0 & \frac{2\pi}{3} & -\frac{2\pi}{3} \end{bmatrix}^T\right) \qquad \text{(I.5)}$$

The voltage reference set by the droop control is then directed into the input of the inner voltage and current control loops.

Fig.I.12 provides a visual representation of the droop control characteristics for two VSIs. It can be observed that the droop slopes play a role as a negative correlation between P/Q and ω/E, respectively. It's important to note that in steady-state conditions, the frequency and amplitude match in both VSIs, where the same slope parameters align, meaning n1=n2 and m1=m2. This synchronization ensures that the two DG units achieve effective and balanced active and reactive power sharing.

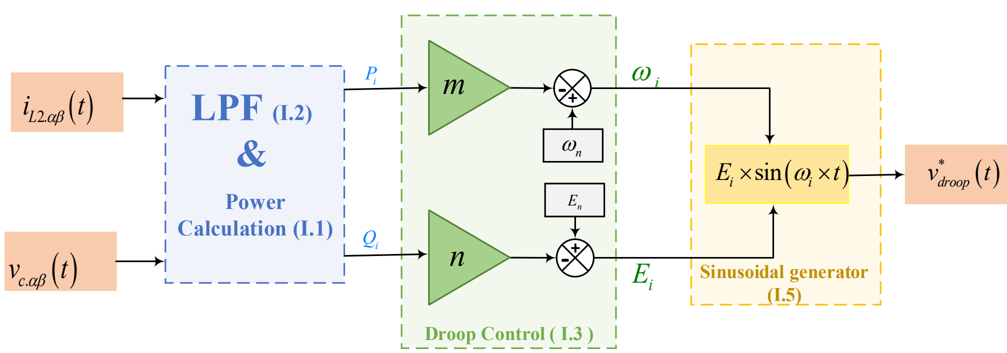

Fig.I. 11 Droop control schematic diagram

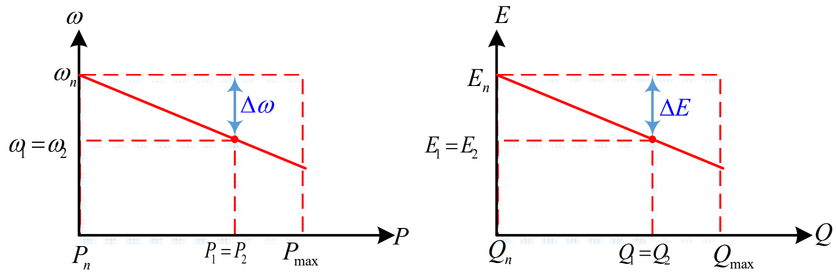

Fig.I. 12 Droop control characteristics

The droop control method discussed earlier plays a crucial role in MG operation, particularly in islanded mode. However, despite its effectiveness in balancing the distribution of active and reactive powers, it faces challenges in terms of current sharing. This is due to the fact that the output current from the inverters depends on their output impedance ratios. Additionally, the presence of harmonic currents can induce voltage distortion at the PCC, especially when VSIs are powering non-linear loads.

To address these limitations and improve power-sharing accuracy, droop coefficients are compensated [103] and tuned [104]. In addition, researchers have explored advanced control strategies such as Model Predictive Control (MPC), Sliding Mode Control (SMC), and Virtual Impedance Control (VIC). MPC uses a mathematical model to optimize control actions, considering system dynamics and constraints. SMC provides robustness against uncertainties and disturbances, ensuring precise voltage and frequency regulation. Virtual impedance control employs virtual impedances to mimic the behavior of a resistive network, improving voltage regulation and damping low-frequency oscillations, and consequently, ensuring precise sharing of current harmonic components when DG units are providing power to non-linear loads.

c. Virtual Impedance Loop

As it was mentioned earlier, despite the effectiveness of the primary control approach based on this technique in achieving an average power distribution, it does come with certain limitations when it comes to proper reactive power and harmonics sharing [84, 105, 106] due to the mismatch of the DGs' line impedance. The droop control method isn't well-suited for distributing current harmonics, especially in cases where VSIs are supplying power to nonlinear loads. Consequently, there have been advancements in the field of droop control that aim to enhance the precision of harmonics sharing [102]. In this regard, the Virtual Impedance Control (VIC) concept has been adopted to achieve more accurate harmonic-current sharing, improve the reactive power-sharing accuracy, and enhance MG stability by standardizing their output impedance [107, 108].

Various approaches have been explored in the literature for three-phase MGs [111], offering valuable insights into their control and performance enhancement. The classical method involves multiplying the current derivative with an inductance and has been widely adopted in the context of three-phase VSIs. This control approach has contributed to enhancing reactive power sharing among DERs.

In [112] researchers investigated the realm of Virtual Impedance (VI) values to improve the overall performance of the MGs. In [113] VI concept was introduced to ensure power decoupling and sharing challenges by increasing the line impedance between the inverter and common bus. Furthermore, [114] provides a thorough design, analysis, and implementation aspects for VI-based control for DGs within a MG setting. In [115-117] VI-based control is employed to enhance power sharing among DGs. Notably, adaptive VI control approaches have been brought out, including communication [118], consensus [119], and sliding-based [120] approaches. These innovations aim to provide accurate harmonic power sharing and voltage harmonic compensation in islanded MGs. On a distributed level, authors in [121] proposed a strategy to achieve robust power sharing and maximize the power transfer through the feeder. The research community has also explored in detail the effects of communication delays and failure on MG performance in [122]. Additionally, in pursuit of better reactive power sharing, novel concepts like the Active Power Filter (APF) [123] and voltage compensation methods [124-125] were proposed to enhance voltage profiles during unbalanced conditions. A dynamic virtual inductance loop was proposed in [126] to compensate for the line impedance voltage drops.

Another concept for the implementation of VI involves the use of the Second-Order General-Integrator (SOGI) strategy, which has seen further development in [127-128], and enhancements with the Enhanced SOGI (ESOGI)-based in [129, 130], Moreover, the High Order Generalized Integrator (HOGI) algorithm has gained prominence in addressing power quality issues in [131,132]. Many studies in the literature provide more analysis of related techniques, such as the Third-Order Generalized Integrator (TOGI), Double SOGI (DSOGI), and n-SOGI. These diverse approaches collectively aim to reduce the output distortions at selected harmonic frequencies caused by current-inherent noise and nonlinear loads, ultimately resulting in improved THD.

This virtual output impedance loop incorporates a fast control loop designed to derive a pure inductive equivalent impedance. This impedance is formed by the series connection of the MG impedances as perceived by the VSI and the virtual impedance as shown in Fig1.9, illustrating the equivalent circuit of VSIs with line and virtual impedances. The process of establishing this virtual output impedance involves adjusting the output-voltage reference in proportion to the time derivative of the inverter output current. This adjustment has the effect of increasing the inverter's output inductive impedance, which, in turn, raises the impedance between the VSI and the common bus line. Consequently, it reduces the circulating current within the MG. The expression for implementing this virtual inductive output impedance can be stated as follows [109] :

$$Z_v(s) = s.L_v \qquad \text{(I.6)}$$

Here, L_v represents the inductor value of the virtual output impedance, and s is the Laplace operator.

Figure 1.10. illustrates the block diagram of the programmed droop control scheme based on virtual output impedance. In this setup, a virtual impedance unit calculates the voltage of the virtual output impedance, taking the inverter output current as input. This virtual impedance voltage is subsequently incorporated as an additional element in the output voltage reference, seamlessly provided by the droop control loop, as depicted below:

$$v_C^*(s) = v_{droop}^*(s) - Z_v(s) i_{L2}(s) \qquad (I.7)$$

The equation provided above outlines the updated output voltage reference by incorporating the virtual output impedance. In fact, each inverter's control loop includes a similar loop.

It's important to note that when the virtual output impedance is programmed as the time derivative of the inverter current, the system becomes quite responsive to output current noise and non-linear loads with a slow rate of change. In response to this challenge, an implementation of the virtual impedance based on the SOGI-Quadrature Signal Generator (SOGI-QSG) scheme has been proposed in the literature, as depicted in Fig.I.13 [109]. This implementation capitalizes on the SOGI method's features to establish a virtual impedance control scheme offering several advantages: i) reduced sensitivity to output current noise; ii) elimination of the need for time derivative calculations; iii) improved total harmonic distortion of the output voltage, and iv) enhanced handling of nonlinear loads [110]. This concept seamlessly integrates into our hierarchical control scheme, where the SOGI-FLL scheme becomes an integral part of all three control levels.

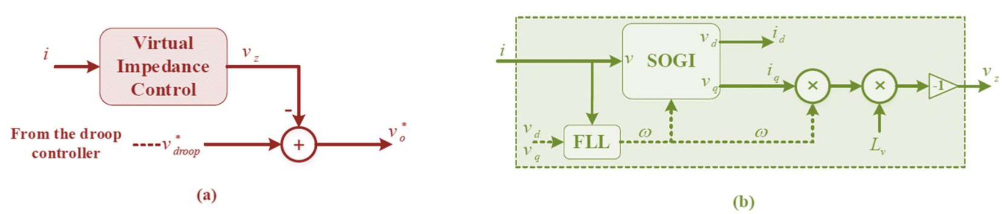

Fig.I. 13 Virtual impedance (a) based reference generation and (b) implementation using the SOGI approach.

d. Inner Control Loops

Level zero or the inner control loop, often referred to as the low-level voltage and current controller, serves to establish the operational state of the DG units. It plays a crucial role in maintaining stable control over the inverter's output voltage and current, even when faced with disturbances. This objective is accomplished by adjusting the inverter's output voltage to match the desired reference value.

Fig.I.14 (a) shows the schematic diagram of the inner controller designed for VSIs, which typically consists of a voltage loop and an inner current loop. These two control loops work together to regulate the inverter's output voltage and control the current while maintaining system stability with high bandwidth and performance, ensuring a rapid response under various operating conditions. The outcomes of this inner loop dictate the gating signals for the IGBTs in the VSI. For more detailed insights into this control level, refer to [8, 9].

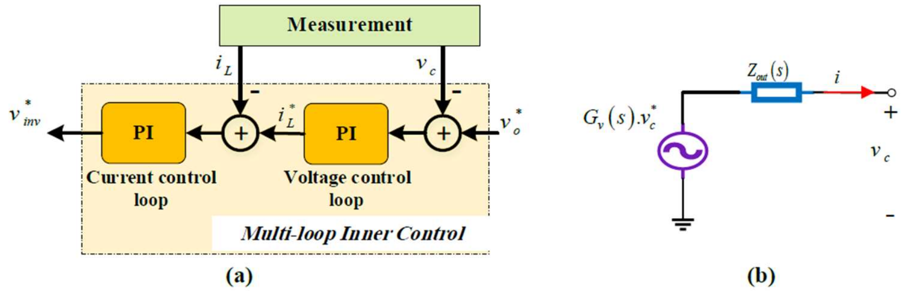

Fig.I. 14 Block diagram of (a) the inner control loop. (b) the equivalent circuit

In a three-phase system, the inner control loop design is very important for the MG performance. Recently, the Proportional Resonant (PR) controllers have been developed to alleviate the tracking uncertainty in some control approaches, as well as offer independent voltage control for grid-forming VSIs. Additionally, in the presence of non-linear loads, they have significantly reduced THD by allowing for selective harmonic rejection. The fundamental drawback of this controller is the sensitivity of the provided signals to the phase and frequency changes [13]. Model Predictive Controllers (MPCs) have been introduced to improve VSI control performance [14, 15]. The MPC uses a model of the system to predict system operation, thus, the variation in system parameters reduces the control system's effectiveness. The neural network and fuzzy controllers are the popular intelligent-based control methods [16, 17] proposed in the literature, aiming to cope with system parameters deviation without requiring a precise mathematical model of the system. Except, training these approaches is not an easy process. Besides, the repetitive-based control strategy [18, 19] performs admirably in the presence of non-linear loads by reducing output voltage and current THD; nevertheless, it suffers from poor tracking accuracy and dynamic performance, and it requires a higher memory compared to other strategies [20]. Sliding-mode control [21–23] is also proposed for controlling VSIs, it has a fast time response and great tolerance to the VSI and filter parameters' fluctuations. This approach, on the other hand, has a high sensitivity to load fluctuations and produces poor steady-state tracking. Another conventional control strategy that is gaining much attention is a simple Proportional-Integral (PI) controller [24,25], which ensures fast time response with minimal steady-state tracking error [21]. PI regulators are commonly proposed in both αβ-frame and *dq*-frame [26-29] to regulate the active power and reactive power independently. By designing separate PI controllers for the d-axis and q-axis variables, independent regulation of voltage and frequency can be achieved.

Therefore, the primary control, with the integration of the droop control method, effectively maintains accurate power load sharing by regulating voltage frequency and amplitude. However, as previously mentioned, it does have its limitations, primarily in the form of steady-state errors and variations in frequency and voltage amplitude. To address these challenges and rectify the deviations in frequency and voltage, an extra control layer, referred to as the secondary control, is introduced [76, 111] .

I.7.2.2 Secondary Control Layer

The secondary controller (SC), our third focus in this thesis, assumes a critical role in rectifying the frequency and amplitude deviations that may occur due to the primary control's droop-based approach [114,120]. This helps enhance power quality by restoring the MG's voltage, frequency, and amplitude to their nominal values. Moreover, it is in charge of synchronizing the MG with the main grid when transitioning from islanded to grid-connected modes [121,122]. Additionally, during islanded mode operation, the SC serves as the MG's Energy Management System (EMS), controlling power flow and power quality[23], which includes tasks like suppressing circulating currents and eliminating harmonics within the MG [112, 113].

Whether centralized or distributed [114], the SC operates with a lower bandwidth compared to the primary control. The schematic representations of these structures are depicted in Fig.I.15. As shown in Fig.I.15 (a), a central control unit in the centralized SC structure manages the DGs and restores the frequency and voltages of the MG. All of the required specifications for this arrangement, including the DG unit voltages and frequencies, are usually sent over a high-speed communication channel. However, the single point of failure is a problem for the centralized control structure [114].

However, Every DG unit in the distributed architecture measures its own voltage and frequency as shown in Fig.I.15(b), and it shares this information with other DG units. A peer-to-peer network is frequently needed for this communication in order to communicate information between each DG unit and its surrounding units.

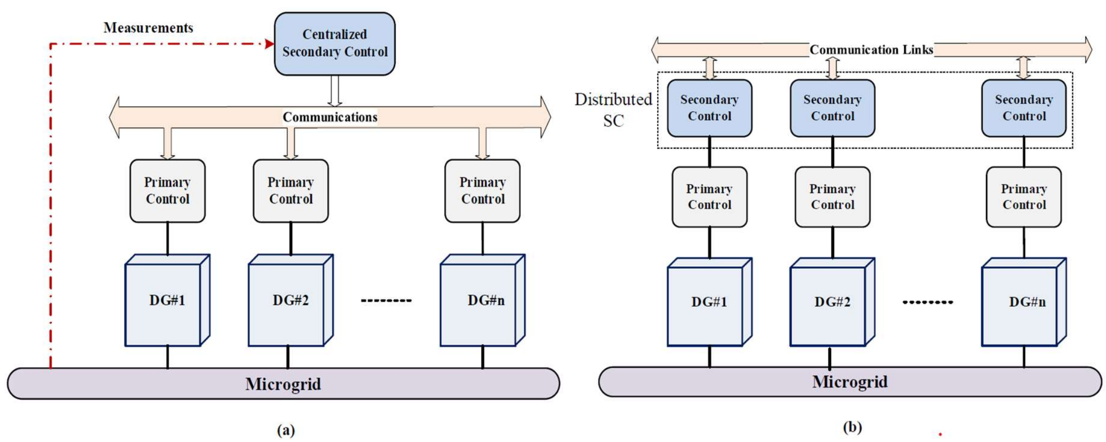

Fig.I. 15 Secondary control (a) centralized and (b) distributed architectures.

The MG's voltage frequency and amplitude (ω_{MG} and E_{MG}) are monitored by both distributed and centralized secondary control systems, which are then compared to their references (ω_{MG}^* and E_{MG}^*) and are transmitted to every unit in order to modify the output voltage [76, 115]. This is achieved by using a PI regulator, whose inputs are the amplitude and frequency variations of the voltage.

Additionally, the phase alignment between the main grid and the MG is carefully monitored and shared across all modules to ensure synchronization of the MG phase. These control systems often integrate a Phase Locked Loop (PLL), which is an integral component, as it helps estimate essential parameters like frequency, amplitude, and phase, which are crucial for the operation of the secondary control loops.

Within the literature, two fundamental approaches for the secondary control layer have been identified: centralized and distributed approaches [116] [117-121].

Under the centralized control approach, the control signals of DGs are generated by a central controller, using estimated MG parameters notably frequency and amplitude. This approach necessitates a strong communication network to effectively transfer the relevant control signals to each DG's primary control unit. Conversely, each DG locally implements the distributed secondary control aiming to increase system reliability. This approach depends on measurable parameters as well as local estimations of other DG units, which are easily shared via a sparse network. The goal is to produce the necessary setpoints for the primary control, thereby enhancing the MG system's overall performance.

The methods mentioned earlier typically employ the PLL technique to measure the frequency and amplitude of the MG at the PCC as well as those of other DG units. However, in the presence of voltage distortions, especially the DC component, resulting from various factors within the MG , these PLLs' efficacy may be limited [122]. While there are methods in the literature that address these issues [123-126], there are currently very few applications that incorporate these solutions into the secondary control layer. This gap offers a fascinating direction for research and practical use in the field of secondary control. Conversely, dynamic models for secondary control aimed at the restoration of frequency and amplitude have been developed using the small-signal model of the PLL, which is considered as an estimator. In order to express the frequency estimate dynamics for frequency restoration, the authors in [76] for example, delved into modeling the centralized secondary control of a three-phase MG, incorporating the PLL transfer function. For the amplitude restoration, the amplitude estimation is modeled as a unity gain. Similar to this, in [118], the frequency recovery model used the PLL model to support two different control strategies: the Smith predictor-based PI controller and the model predictive controller. On the other hand, reported modeling related to voltage recovery is notably lacking. Adopting a parallel concept, [110], [119] and [120] have modeled distributed secondary control for frequency and amplitude restoration. In [121], the state-space modeling of distributed voltage control took into account unity voltage feedback. It is important to remember that all current modeling techniques are designed for three-phase MGs, where amplitude estimate is represented as a unity gain and only frequency estimate dynamics are considered. This method works for three-phase MGs, where the PLL predicts the frequency, and the amplitude can be directly calculated using the αβ voltage components based on the abc/αβ coordinate transformation. On the other hand, with single-phase MGs, a single-phase input voltage is used to estimate both frequency and amplitude using the PLL. Consequently, both variable's estimation dynamics must be taken into account when modeling frequency and amplitude restoration. Addressing this, authors in [87] proposed a schematic diagram for the secondary control model that was intended to restore the amplitude in a single-phase MG, where the dynamics of the amplitude estimation are described by a first-order transfer function. Interestingly, this stands as the sole work in the literature addressing this specific problem. It is important to acknowledge, nonetheless, that the authors did not go into detail about the derivation of this transfer function or the selection of its parameters. This can be attributable to the complexity of expressing amplitude estimation dynamics from the PLL's small-signal model. As such, analyses of amplitude restoration control based on this model lack precision, which could compromise appropriate control parameter tuning and, in turn, the MG's stability.

The secondary control plays a critical role in restoring the MG's voltage frequency and amplitude to their rated values while ensuring synchronization with the main grid. As previously mentioned, secondary control can be categorized into two main architectures: centralized and distributed, designed for both three- and single-phase MGs. These architectures have been implemented in various research studies, such as [127] and [115] for centralized control, and [115] for distributed control. Additionally, numerous advanced control techniques have been introduced in the literature to meet the objectives of secondary control with optimal performance, including Fuzzy Logic Control (FLC) [127], $H\infty$ control [128], and Model Predictive Control (MPC) [129], among others.

In the secondary control layer, a communication network is essential for transmitting the required parameters to the primary control. This communication network stands as a defining feature that distinguishes between different secondary control architectures. Furthermore, the impact of communication delays has been extensively explored in the literature [130], [131]. For instance, [130] delves into the stability issues related to communication delay in the distributed secondary frequency and voltage control of three-phase islanded MGs, offering integrated modeling and analysis. Similarly, [131] investigates the influence of communication delay on system dynamic performance in the context of distributed secondary control for single-phase MGs.

However, in all the aforementioned works, conventional PLLs are predominantly employed for estimating the frequency, amplitude, and phase angle of the MG voltage. It's important to note that conventional PLL schemes, particularly with respect to parameter estimation, are highly susceptible to load variations, harmonic issues, and DC component disturbances [132]. These factors can significantly impact the performance of frequency and amplitude restoration control loops, potentially jeopardizing the overall stability of the MG. Additionally, the use of sine and cosine computing functions in PLLs adds complexity to their implementation, especially in single-phase systems, which can result in longer computational times. Moreover, the presence of a DC component in the input of the PLL can affect its estimation performance and, consequently, the stability of the system.

To address these issues, especially in three-phase systems, advanced solutions such as the SOGI-FLL and more advanced variants capable of DC-offset rejection (ESOGI-FLL [110]) have been proposed in the literature to enhance estimation characteristics [126]. These advanced schemes are recognized for their simplicity in implementation and their high DC-offset rejection capabilities, and they have proven effective in various MG applications [110].

Despite extensive research into the performance of PLLs in secondary control from a dynamic perspective, there is a noticeable gap in the literature concerning the integration of enhanced estimation schemes into the secondary control layer for droop-controlled VSIs.

Additionally, from a modeling standpoint, since PLLs are a part of the secondary control, it's expected that their estimation dynamics will be incorporated into the frequency and amplitude restoration models. Some research studies have indeed addressed this aspect. For instance, small-signal modeling of distributed secondary control for frequency and amplitude restoration in an islanded MG has been discussed in [115]. In this work, the PLL dynamics of the frequency estimate are included in the frequency restoration model, and unity feedback is considered for the amplitude estimate in the amplitude restoration model. A similar concept is adopted in the modeling of centralized secondary control for two three-phase VSIs forming an islanded MG in [131], where only the dynamics of the frequency estimation are involved. In [133], the authors have modeled the frequency restoration control stage for a three-phase MG, focusing only on the dynamic aspects of frequency estimation. Moreover, in [134], a first-order transfer function is introduced to represent the PLL estimation dynamic in the frequency restoration control model, while the amplitude restoration model is not presented.

For three-phase MG applications, few studies addressing the modeling of centralized secondary control are available in the literature, unlike for single-phase MGs, such as in [130]. In this work, the same concept model the frequency restoration control for three-phase MG is introduced, where a first-order transfer function is used to account for the PLL estimation dynamics, while unity feedback is proposed for the amplitude restoration model.

However, it's crucial to note that the concept adopted in these studies may be valid for three-phase applications, where the amplitude can be computed in the αβ frame by using the αβ voltage components. Nonetheless, in single-phase MGs, the amplitude must be estimated in the same way as frequency, from a single input voltage. As a result, the amplitude estimation dynamics should be incorporated into the amplitude restoration control model. The models derived in [135], based on this concept, may raise questions regarding their accuracy and stability implications, which could compromise the overall stability of the MG system.

Furthermore, it's worth mentioning that a comprehensive control design for tuning the parameters of the secondary controller is notably absent in the literature.

I.7.2.3 Tertiary Control

The tertiary control level, our fourth and last focus in this thesis, is specifically designed to oversee and regulate the flow of active and reactive power between the primary grid and the entire MG at the PCC. It is the last level of control in grid-tied mode, it is typically centralized and operates at a slower pace. This control level handles maintaining load balance [43] and islanding detection, so its primary role is regulating power when the MG connects to the main grid [124], as well as ensuring efficient management of the bidirectional power flow between them Additionally, the power references provided to the secondary control can be determined through an optimal analysis that considers market prices, weather forecasts (especially when using sources with unpredictable behavior like solar panels), and agreements between the customer and the grid operator .

In grid-connected mode, the MG's operation entails exporting and importing energy to and from the primary grid. This not only ensures a balanced power flow between the MG and the primary grid but also supports various grid services. To fulfill these objectives, the tertiary control acts as a central controller, orchestrating the optimal bidirectional control of active and reactive power flow, managing power distribution, and coordinating DG units to operate at optimal set points.

In MG systems that are interconnected with the utility grid, the primary aim of the tertiary control is to manage power flow effectively. It accomplishes this by allowing any energy deficit in the MG to be supplied by the utility grid and by diverting any surplus energy in the MG to the primary grid [65, 83, 135]. Consequently, the tertiary control enables bi-directional power flow control by defining the desired active and reactive power values and providing voltage amplitude and frequency set points to the lower control levels [97, 135, 136].

Fig.I.16 provides a block diagram illustrating the tertiary control level for a MG consisting of multiple DG units connected to the main AC grid. By measuring the current and voltage in the grid, it becomes possible to calculate the active and reactive power injected into the grid (P_g and Q_g). These computed values are then compared to their desired counterparts, P_g^* and Q_g^*, and PI controllers generate the new voltage frequency and amplitude set points.

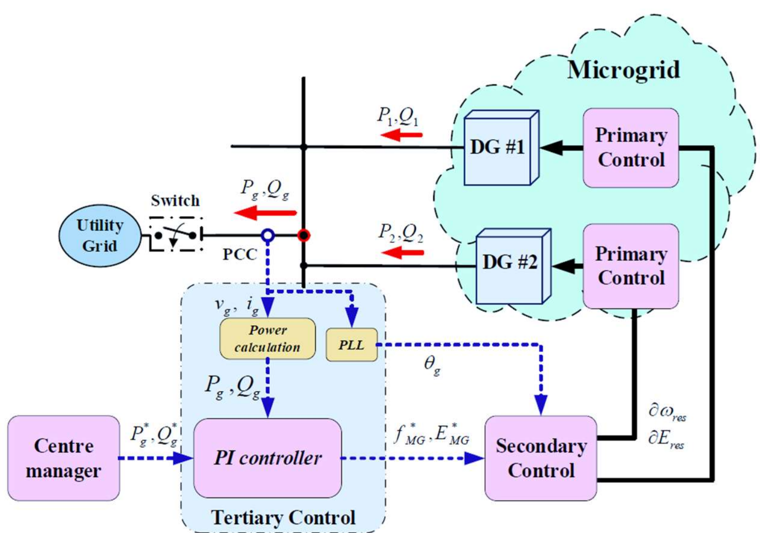

Fig.I. 16 Tertiary control block diagram.

The frequency and amplitude references obtained are subsequently transmitted to the secondary control layer, where they play a pivotal role in power flow control at the inverter level. In this control layer, the employment of a PLL is essential for estimating the frequency, amplitude, and phase angle of the grid voltage, which ensures the synchronization of the MG with the grid during the transition from island to grid-connected modes.

It's important to note that the actions of the tertiary control should be temporarily suspended when the system detects an islanding mode, signifying the disconnection of the utility grid from the MG.

The tertiary control layer functions as a centralized controller responsible for managing power flow between the MG and the grid. It enables this by enabling real and reactive power reference tracking in all DG units, and it comes into play when a grid-connected mode is anticipated. Various research studies have explored the implementation of tertiary control in droop-controlled s during grid-connected mode [97, 137-140].

While extensive research has been conducted on designing tertiary control for three-phase grid-connected MGs, there remains a lack of clarity regarding single-phase MGs. In the tertiary control stage, a PLL is commonly integrated to estimate crucial grid parameters needed by the controller. Furthermore, since active and reactive powers from the grid are required, they need to be calculated. In a three-phase system, these powers can be directly calculated in the $\alpha\beta$ frame, as indicated in Eq. (I.1), followed by low-pass filtering to obtain average active and reactive powers from instantaneous values. However, in single-phase MGs, a power calculation unit with low-pass filtering is generally integrated into the tertiary control level to compute average powers, with the estimation of the voltage orthogonal component being a primary concern.

It's essential to recognize that the integration of a LPF, as is often done, can reduce the dynamic response of the control system, impacting MG stability. Additionally, the presence of a DC component in the PLL input signal can influence system stability. As a result, advanced power calculation methods, including SOGI-based schemes, have been proposed to address these issues and have demonstrated their effectiveness. Yet, these advanced structures have not been widely implemented in the tertiary control-based grid-connected MGs.

From a modeling perspective, power flow modeling in the MG, designed for the tertiary control level, closely resembles that used for the droop control, differing primarily in the closed-loop control model. Various modeling approaches have been developed to derive small-signal models for power flow control in MG systems. However, the number of works related to power flow modeling in grid-tied MGs with tertiary control, particularly in single-phase systems, is limited. Furthermore, researchers have predominantly focused on decoupling active and reactive power in the control system, with few addressing coupling concepts. The incorporation of coupling concepts could contribute to more accurate MG modeling for hierarchical control.

As for power calculation, previous works have primarily employed a low-pass filter transfer function to describe the power calculation dynamics in power flow models. However, the inclusion of an additional block to extract the orthogonal component voltage in single-phase MGs, along with its dynamics, is often overlooked. This oversight can impact the accuracy of stability analyses based on these models. Moreover, a comprehensive and clear tuning procedure for selecting appropriate tertiary controller parameters is rarely found in the literature. These issues could lead to improper power injection into the grid, questioning the overall system's stability.

In summary, the DESOGI-FLL method, which excels at estimating key voltage parameters and the synchronization process, has the potential to enhance both secondary and tertiary control, particularly for single-phase MG applications. This method is characterized by its precise estimation capabilities, ease of implementation, and robustness to various load disturbances. Inspired by the features of the DESOGI-FLL, this thesis focuses on designing and modeling the primary, secondary and tertiary control layers with DESOGI-FLL-based estimation structures. These control layers are intended for droop-controlled MGs operating in grid-connected and islanded modes. The research work also includes in-depth analysis and comprehensive tuning procedures to optimize MG control performance. The implementation of the complete hierarchical control for a three-phase grid-tied and islanded PVMG is conducted to validate the thesis proposal.

I.8 Conclusion

This chapter has conducted an in-depth exploration of MGs, including their definition, advantages, challenges, diverse operational modes, structural composition, and a comprehensive array of control strategies. Particular emphasis has been placed on the hierarchical control strategy, which, within the context of this thesis, is of major concern. Furthermore, a state-of-the-art review of the latest scholarly contributions in the field has been provided.

The next chapter will delve into the specifics of primary control, offering a more profound understanding of how it plays a crucial role within the MG framework. It will entail a comprehensive explanation of each control loop, complemented by the analysis of simulation results, fostering a comprehensive exploration of this crucial component.

Chapter II: Modeling and Analysis of Primary Control: Inner & Power Sharing Control Loops

II.1 Introduction

In line with the previous chapter, most existing studies utilize a hierarchical control approach, involving three control tiers: primary, secondary, and tertiary. These tiers strike a balance between decentralized, centralized, and distributed control frameworks. The primary control can be divided into two blocks. The first one, often referred to as inner control or zero level, manages voltage and frequency to meet the desired references at the power stage. It comprises an internal CCL and an external VCL. The second one deals with power sharing, distributing power among multiple parallel converters.

With the goal of addressing challenges related to power quality, stability, dynamic response, and load sharing in VSIs under different operating conditions, this chapter conducts a comprehensive examination of primary control in a three-phase VSI within an islanded AC MG system, encompassing both inner and power-sharing control loops. It establishes mathematical closed-loop models for the designed outer voltage and inner current control schemes, using PI and P controllers, respectively. A systematic control design approach is then developed to effectively tune the controller parameters. Additionally, this chapter introduces an advanced virtual impedance control based on the Enhanced-SOGI (ESOGI) method for three-phase droop-controlled VSIs connected in parallel to create an islanded MG. The MSOGI method accurately estimates current fundamental and harmonic components required for computing the VI output voltage, which in turn may reduce circulating current. Consequently, it is expected that the MSOGI-based Virtual Impedance Control Loop (VICL) may enhance the accuracy of active, reactive, and harmonic power sharing.

To evaluate the performance of the proposed control strategy, a series of simulations are carried out in the MATLAB/SimPowerSystem environment.

II.2 System Under Study Presentation

As we have seen in the previous chapter, the primary control is a local controller. It is the first level in the MG hierarchical control, responsible for improving the MG system performance, stability, and reliability; meanwhile adjusting the frequency and the amplitude of the inverter output voltage to get the reference of the inner cascaded controller, which is the focus of the current work.

The schematic diagram of the studied control scheme in this research work, intended for the three-phase VSIs, is shown in Fig. II.1. As shown, the AC bus or the PCC is connected to the DG unit, which consists of a DC source and an LC-filtered VSI, through a line impedance. Additionally, this PCC joins the grid and both linear and nonlinear loads. Where:

- $L1$, $r1$ and C are the filter inductor, resistor and capacitor, respectively, while $L2$ and r_2 are the line impedance inductor and resistor.
- i_{L1abc} and i_{L2abc} are the measured filter inductor and the inverter output currents, respectively.

- $v_{C.abc}$, $v_{inv.abc}$ and U_{DC} are the capacitor, the output, and the DC source voltages.

The proposed controller comprises:

a) A double-loop inner controller, consisting of the cascaded current and voltage control loops.

b) A power-sharing control unit includes the droop-based power control unit and the virtual impedance control loop.

Each of these loops is explained separately in the following subsections.

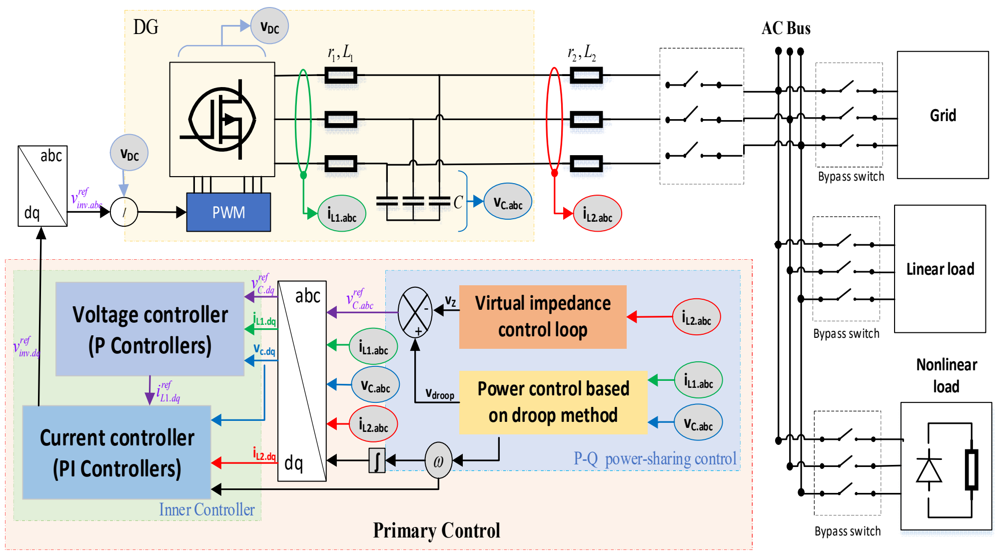

Fig.II. 1 Block diagram of the primary control

II.3 Double-Loop Inner Controller

To improve the inverter output control, the inner controller, as seen in Fig.II.1, is introduced with two cascaded loops. (i) an external VCL that regulates the capacitor voltage and produces the filter inductor current reference to the second loop, which is (ii) the internal CCL that aims to adjust the inductor current to that reference. It uses the voltage reference provided by the power-sharing controller in the *dq* rotating reference frame ($V^*_{C.dq}$), the measured inverter output voltage and current as well as the filter inductor current to generate the inverter side voltage reference signal. The latter is then received by a Pulse Width Modulation (PWM) generator, which in turn transmits switching control signals to the inverter.

The trends in control in recent research works went towards the implementation in the rotating reference frame (*dq*), i,e, controlling both the direct and quadrature components. This requires two regulators in each loop. In our study, two PI controllers are proposed for the VCL, and two P controllers for the CCL for the purpose of ensuring high-tracking performance with simple implementation.

Besides, in the section, the mathematical models and schemes of the proposed VCL and CCL based on PI and P controllers, respectively, in *dq*-coordinates are first derived. A systematic and effective control design is suggested for the proper tune of the controllers' parameters, in which the stability is analyzed considering the settling time and the damping factor variations. In addition, the effect of the compensation and decoupling terms is demonstrated by analytical and frequency analyses. Moreover, the robustness of the proposed controller against the controller parameters is elaborated.

II.3.1 Modeling of a Stand-Alone LC-Filtered Three-Phase VSI

Based on the electrical circuit of the VSI shown in Fig. II. 2, and by applying Kirchoff's Voltage and Current Laws (KVL and KCL) in the output of the DG unit, the average mathematical model describing the LC-filtered VSI can be obtained by:

$$\begin{cases} \dfrac{d\, i_{L1.abc}}{dt} = -\dfrac{r_1}{L_1} i_{L1.abc} + \dfrac{1}{L_1}\overline{v}_{ref.abc} - \dfrac{1}{L_1} v_{C.abc} \\ \dfrac{d\, v_{C.abc}}{dt} = \dfrac{1}{C} i_{L1.abc} - \dfrac{1}{C} i_{L2.abc} \end{cases} \qquad \text{(II.1)}$$

$$v_{inv.abc} = DU_{DC} \qquad \text{(II.2)}$$

where $i_{L1.abc}$ and $i_{L2.abc}$ are the filter Inductor and the inverter output currents. $v_{C.abc}$, $v_{inv.abc}$ and U_{DC} are the capacitor, inverter output and DC source voltages, while D is the duty cycle.

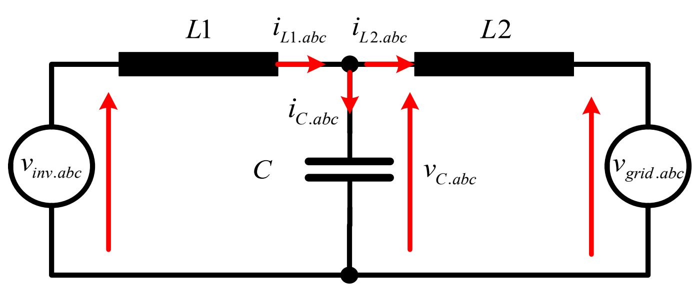

Fig.II. 2 Electrical scheme of an LC-filtered VSI.

Considering the park transformation matrix (II.3), and a symmetrical three-phase system, the system of equation (II.1) can be written in the *dq* frame as follows:

$$\sqrt{\frac{2}{3}}\begin{pmatrix} \cos(\theta) & \cos(\theta-\frac{2\pi}{3}) & \cos(\theta-\frac{4\pi}{3}) \\ -\sin(\theta) & -\sin(\theta-\frac{2\pi}{3}) & -\sin(\theta-\frac{4\pi}{3}) \\ \frac{1}{\sqrt{2}} & \frac{1}{\sqrt{2}} & \frac{1}{\sqrt{2}} \end{pmatrix} \qquad \text{(II.3)}$$

$$\begin{cases} \dfrac{d\ i_{L1.d}}{dt} = -\dfrac{r_1}{L_1} i_{L1.d} + \dfrac{1}{L_1} v_d - \dfrac{1}{L_1} v_{C.d} + \omega_x i_{L1.q} \\ \dfrac{d\ i_{L1.q}}{dt} = -\dfrac{r_1}{L_1} i_{L1.q} + \dfrac{1}{L_1} v_q - \dfrac{1}{L_1} v_{C.q} - \omega_x i_{L1.d} \\ \dfrac{d\ v_{C.d}}{dt} = \dfrac{1}{C} i_{L1.d} - \dfrac{1}{C} i_{L2.d} + \omega_x v_{C.q} \\ \dfrac{d\ v_{C.q}}{dt} = \dfrac{1}{C} i_{L1.q} - \dfrac{1}{C} i_{L2.q} - \omega_x v_{C.d} \end{cases} \qquad \text{(II.4)}$$

where $\theta = \int \omega_x \mathrm{dt}$ is the voltage phase angle reference obtained by the droop equations, and ω_x is the angular frequency of the *dq*-frame.

In Laplace (s-domain), equation (II.4) can be expressed as follows:

$$\begin{cases} i_{L1.d} = \left[\dfrac{1}{L_1 s + r_1}\right]\left[v_d - v_{C.d} + L_1\ \omega_x i_{L1.q}\right] \\ i_{L1.q} = \left[\dfrac{1}{L_1 s + r_1}\right]\left[v_q - v_{C.q} - L_1\ \omega_x i_{L1.d}\right] \\ v_{C.d} = \dfrac{1}{C\ s}\left[i_{L1.d} - i_{L2.d} + C\ \omega_x v_{C.q}\right] \\ v_{C.q} = \dfrac{1}{C\ s}\left[i_{L1.q} - i_{L2.q} - C\ \omega_x v_{C.d}\right] \end{cases} \qquad \text{(II.5)}$$

Based on those equations, the block diagram of the LC-filtered VSI in the *dq*-frame can be obtained as shown in Fig. II. 3, where the filter inductor and capacitor transfer functions G_i and G_v are involved.

$$\begin{cases} G_i = \dfrac{1}{r_1 + L_1 s} \\ G_v = \dfrac{1}{Cs} \end{cases} \qquad \text{(II.6)}$$

It can be observed that the d-axis and q-axis inductor current and capacitor voltage are coupled by $(L\omega_x)$ and $(C\omega_x)$, respectively. While ($v_{C.d}$) ($v_{C.q}$) and ($i_{L2.d}$) ($i_{L2.q}$) represent compensation terms. Hence, these terms have to be taken into consideration for the design of the VCL and CCL.

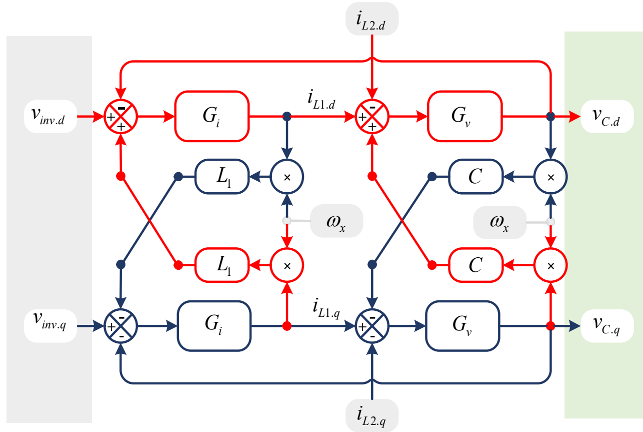

Fig.II. 3 linearized LC-filtered model in dq-reference frame

II.3.2 Internal Current Control Loop

As noted before, current and voltage signals are converted to direct components in the synchronous reference frame, allowing them to be controlled easily and effectively using two P regulators. The issue is that the coupling links between the d and q axes, as shown in Fig.II. 3, cause disturbances and degrade the performance of the CCL. Here ($L\omega_x i_{L1q}$)and ($-V_{C.d}$)are the d-axis' disturbances, and ($-L\omega_x i_{L1d}$) and ($-V_{C.q}$)are the q-axis' disturbances. To eliminate them, they are added to the CCL with an opposite sign as shown in Fig. II. 4.

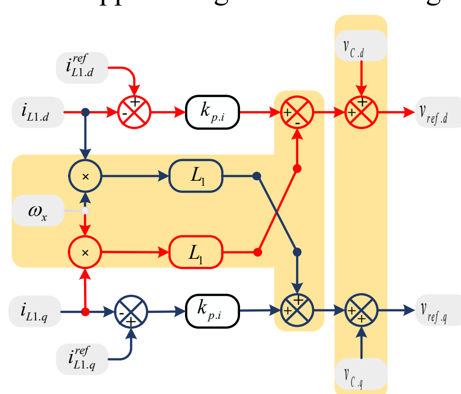

Fig.II. 4 Block diagram of the CCL.

Accordingly, the expression of the current controller can be obtained as follows:

$$\begin{cases} v_{ref.d} = k_{p.i}\left(i_{L1-ref.d} - i_{L1.d}\right) + v_{C.d} - L_1\ \omega_x i_{L1.q} \\ v_{ref.q} = k_{p.i}\left(i_{L1-ref.q} - i_{L1.q}\right) + v_{C.q} + L_1\ \omega_x i_{L1.d} \end{cases} \quad \text{(II.7)}$$

where $k_{p.i}$ is the proportional gain of the current controller, and $i_{L1-ref.dq}$ is the generated current reference.

II.3.3 External Voltage Control Loop

For the VCL, the ($C\omega_x V_{Cq}$) and ($-i_{L2d}$)are the d-axis' disturbances, while ($-C\omega_x V_{Cq}$) and ($-i_{L2q}$)are the q-axis' disturbances. As a result, the compensation and decoupling terms with opposite signs are added. Fig.II.5 depicts the designed VCL schematic diagram based on two PI regulators.

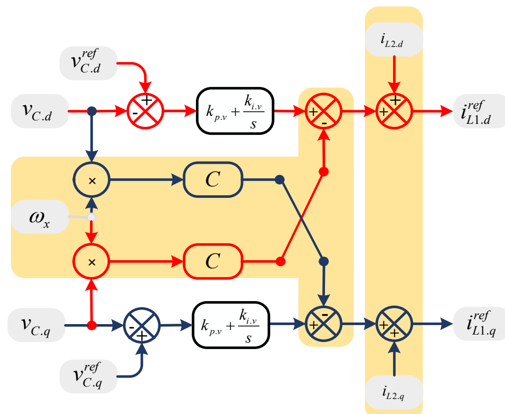

Fig.II. 5 Block diagram of the VCL.

According to this diagram, the voltage controller expression can be obtained as follows:

$$\begin{cases} i_{L1-ref.d} = \left(k_{p.v} + \dfrac{k_{i.v}}{s}\right)\left(v_{C-ref.d} - v_{C.d}\right) + i_{L2.d} - C\ \omega_x v_{C.q} \\ i_{L1-ref.q} = \left(k_{p.v} + \dfrac{k_{i.v}}{s}\right)\left(v_{C-ref.q} - v_{C.q}\right) + i_{L2.q} - C\ \omega_x v_{C.d} \end{cases} \quad \text{(II.8)}$$

where $k_{p.v}$ and $k_{i.v}$ are the voltage control's proportional and integral gains, and $v_{d.q}^{ref}$ is the voltage reference of the inverter side.

II.3.4 Closed-Loop Model

Fig .II. 6 depicts the schematic block diagram of the closed-loop model of the system, it consists of (i) the inner loops transfer functions, and (ii) the model of the LC-filtered VSI (plan) including the transfer function *T(s)* that describes the inverter's time delay dynamics. *T(s)* can approximatively be given by:

$$T(s) = \frac{v_{dq}(s)}{v_{ref.dq}(s)} = \frac{1}{1+1.5\ .\ T_s\ .\ S} \quad \text{(II.9)}$$

where T_s denotes the sampling time and v_{ref-dq} the VSI output voltage reference.

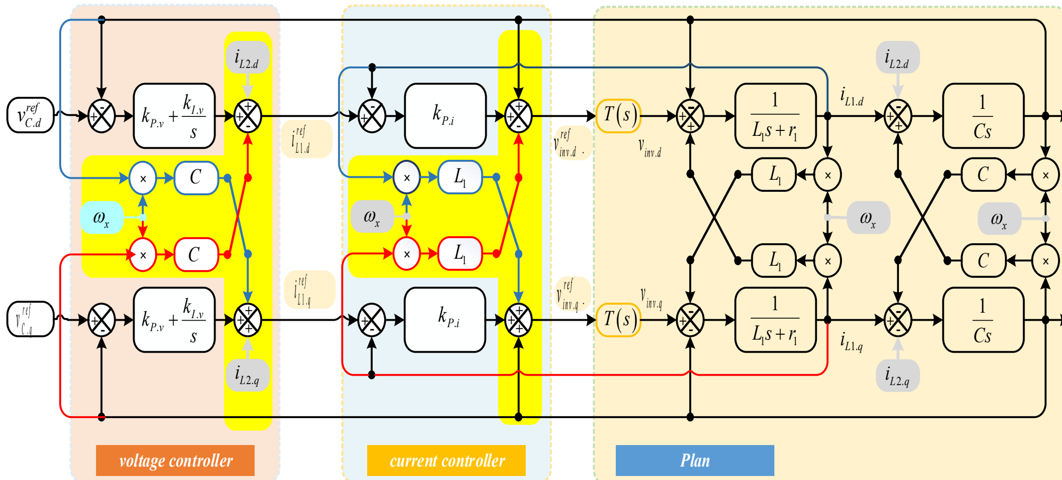

Fig.II. 6 Closed-loop model of voltage-controlled LC-filtered VSI.

Based on Figs. II.3- II.5, the mathematical closed-loop models of the CCL and VCL can be expressed by:

$$\begin{cases} i_{L1} = G_i^{BF}\, i_{L1}^{ref} + H_i\, v_c \\ v_c = G_v^{BF}\, v_c^{ref} + Z_{i.L1}\, i_{L1} + Z_{i.L2}\, i_{L2} \end{cases} \quad \text{(II.10)}$$

where, the transfer functions G_i^{BF}, G_v^{BF}, $H_i, Z_{i.L1}$ and $Z_{i.L2}$ can be defined, for each controller's loop, as given below:

$$\begin{cases} G_i^{BF} = \dfrac{k_{p.i} T_s G_i}{1 + k_{p.i} T_s G_i} \\ H_i = \dfrac{G_i (T_s - 1)}{1 + k_{p.i} T_s G_i} \end{cases} ; \begin{cases} G_v^{BF} = \dfrac{\left(k_{p.v} + \dfrac{k_{i.v}}{s}\right) G_i^{BF} G_v}{1 + \left(k_{p.v} + \dfrac{k_{i.v}}{s}\right) G_i^{BF} G_v} \\ Z_{i.L1} = \dfrac{G_v H_i}{1 + \left(k_{p.v} + \dfrac{k_{i.v}}{s}\right) G_i^{BF} G_v} \\ Z_{i.L2} = \dfrac{\left(k_{p.v} + \dfrac{k_{i.v}}{s}\right) G_i^{BF} G_v}{1 + \left(k_{p.v} + \dfrac{k_{i.v}}{s}\right) G_i^{BF} G_v} \end{cases} \quad \text{(II.11)}$$

By substituting the expressions of these functions in (II.10), the voltage and current closed-loop models can be easily derived. These transfer functions are employed for the analysis of the system stability and control parameters tuning given later.

II.4 Control Design and Parameters Tuning

Unlike the existing techniques, where stability analyses are performed with random variation of the controller parameters (i.e., k_p and k_i), in this subsection, a systematic guideline is suggested for the parameters tuning. The aim is to achieve high efficiency with low energy cost and increase the production rate while reducing process variability. Stability analyses considering the variation of the transient response settling time are then conducted.

The proposed guideline can be summarized in three steps:

- The simplified closed-loop models of both VCL and CCL are derived. Considering that the time delay is very small compared to the CCL response time, its transfer function (II.9) results in (II.12) below. Consequently, the closed-loop transfer function for the d and q-axis CCL can be written as given in (II.13):

$$T(s)\Big|_{Steady-state} = 1 \qquad \text{(II.12)}$$

$$G_{i.dq}^{FB}(s) = \frac{i_{L1.dq}}{i_{L1-ref.dq}} = \frac{\frac{k_{p.i}}{L_1}}{s + \frac{k_{p.i} + r_1}{L_1}} \qquad \text{(II.13)}$$

Assuming that the CCL is much faster than the VCL, its closed-loop transfer function becomes:

$$G_{i.dq}^{FB.ss}(s)\Big|_{Steady-state} = \frac{i_{L1.dq}}{i_{L1-ref.dq}} = 1 \qquad \text{(II.14)}$$

$$G_{v.dq}^{FB}(s) = \frac{v_{C.dq}}{v_{C-ref.dq}} = \frac{\frac{k_{P.v}}{C}s + \frac{k_{I.v}}{C}}{s^2 + \frac{k_{P.v}}{C}s + \frac{k_{I.v}}{C}} \qquad \text{(II.15)}$$

- The mathematical expressions of the controllers' parameters as a function of the controllers' gains are determined. It can be seen that the CCL exhibits a first-order transfer function. While VCL exhibits a second-order transfer function. By matching the characteristic equations of the derived closed-loop models, (II.13) and (II.15), with the desired transfer functions described by:

$$\begin{cases} G_{i_{desired}}^{BF}(s) = k_i \dfrac{1}{\tau s + 1} \\ G_{v_{desired}}^{BF}(s) = \dfrac{\omega_v^2}{s^2 + 2\zeta_v \omega_v s + \omega_v^2} \end{cases} \qquad \text{(II.16)}$$

The expressions of the parameters k_i, τ, ζ_v, and ω_v can be derived as follows:

$$\begin{cases} k_i = \dfrac{k_{p.i}}{k_{p.i}+r_1} \cong 1 \\ \tau = \dfrac{L_1}{k_{p.i}+r_1} \end{cases}, \qquad \begin{cases} \zeta_v = \dfrac{k_{p.v}}{2C\omega_v} \\ \omega_v = \sqrt{\dfrac{k_{i.v}}{C}} \end{cases} \qquad \text{(II.17)}$$

where k_i and τ denote the gain factor and the time constant of the internal CCL, while ζ_v, and ω_v are the damping and the natural frequency of the outer VCL.

Based on (II.17), the parameters of the CCL and VCL are then given by (II.18) below:

$$k_{p.i} = \frac{L_1}{\tau}, \qquad , \qquad \begin{cases} k_{p.v} = 2C\zeta_v\omega_v \\ k_{i.v} = C\omega_v^2 \end{cases} \qquad \text{(II.18)}$$

- The controller's gains (τ, ζ_v and ω_v) are described based on the optimal transient response's desired overshoot M_p and settling time T_s by using the following equations:

$$t_{s.i} = 4\tau \qquad , \qquad \begin{cases} M_{p.v} = e^{\frac{\zeta_v \pi}{\sqrt{1-\zeta_v^2}}} \\ t_{s.v} = \dfrac{4}{\zeta_v\omega_v} \end{cases} \qquad \text{(II.19)}$$

It is worth mentioning that these parameters are chosen according to the analysis based on root-locus plots while considering the following conditions:

$$\begin{cases} f_n \langle\langle \dfrac{1}{t_{s.v}} \langle\langle \dfrac{1}{4t_{s.i}} \langle\langle f_{rs} \langle\langle \dfrac{f_{switch}}{2} \\ 0.4 \le \zeta_v \le 1 \end{cases} \qquad \text{(II.20)}$$

where, f_n, f_{rs}, and f_{switch} are the fundamental frequency, the LC-filter resonant frequency, and the inverter switching frequency. While $t_{s.i,v}$ and ζ_v are the current and voltage settling times and the damping factor, respectively.

The impact of $t_{s.i,v}$ and ζ_v parameter on the system performance is analyzed by adjusting one of them each time. Therefore, the range of the parameters ensuring the system stability, can be obtained. The desired performance of the system can be achieved according to the pole distribution of those parameters. More details are given in the next subsection.

II.4.1 Sensitivity Assessment

The influence of the settling time ($t_{s.i}$, $t_{s.v}$) and the damping factor (ζ_v) on the roots' movement of the closed-loop models of the current control G_i^{BF} and the voltage control G_v^{BF} are investigated.

The characteristic equations of the CCL and VCL model can be expressed as follows:

$$\begin{cases} 1+k_{p.i}\, T_S G_i = 0 \\ 1+\left(k_{p.v}+\dfrac{k_{i.v}}{s}\right) G_i^{BF} G_v = 0 \end{cases} \qquad \text{(II.21)}$$

The root plots of the CCL characteristic equations are illustrated in Fig.II.7. They are obtained by changing the settling time $t_{s.i}$. As shown in the figure, there are two couple of roots represented in blue and red colors.

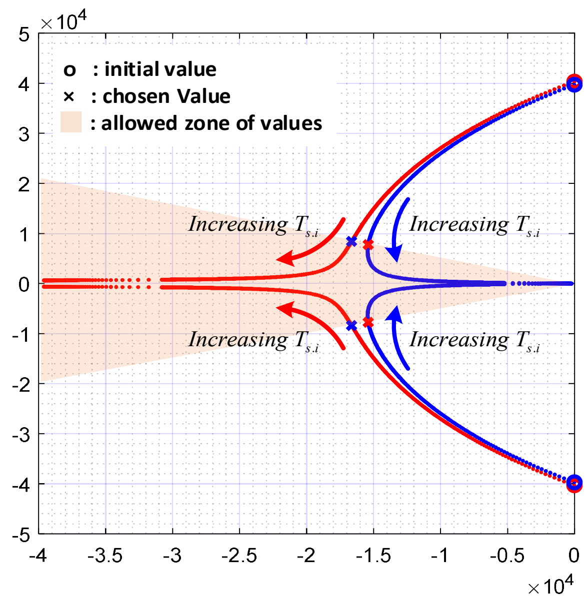

Fig.II. 7 Root-locus corresponding to the change of parameter $\boldsymbol{Ts\!-\!i}$

The first ones (red ones) are moving from the positive part of the real axis (unstable region) to the negative part (stable region) with a decrease of the imaginary part, when $t_{s.i}$ increases.

While the second ones are also moving from the positive part of the real axis (unstable region) to the negative part (stable region) with a decrease of the imaginary part, but at a certain value of $t_{s.i}$, they return to the unstable region.

From that, and knowing that the optimal controller parameters are chosen when the roots are near from real-axis of the negative part, the value of the settling time $t_{s.i}$ is chosen as:

$$t_{s.i} \geq 1ms \qquad \text{(II.22)}$$

It can be seen that the system stability range of the CCL has a wide range of changes in the value of the response time, which allows for reaching the optimal response time while maintaining the system stability.

The plots describing the influence of the settling time $t_{s.v}$ and the damping factor ζ_v on VCL are illustrated in Fig. II.8, where the root-locus curves are obtained by fixing $t_{s.i}$ at the chosen value that achieves the CCL stability, and ζ_v once at 0.8 (blue curve), once at 1.2 (red curve) and once at 1.2 (zoom), and changing $t_{s.v}$. As shown in the figure, as ζ_v increases, the poles move to the stable region, so it can be selected in the way that all roots are on the negative side of the real axis, then it can be determined as:

$$0.8 \leq \zeta_v \qquad \text{(II.23)}$$

while the settling time $t_{s.v}$, is determined to guarantee the VCL stability, so it is chosen as:

$$T_{s.v} \geq 3ms \qquad \text{(II.24)}$$

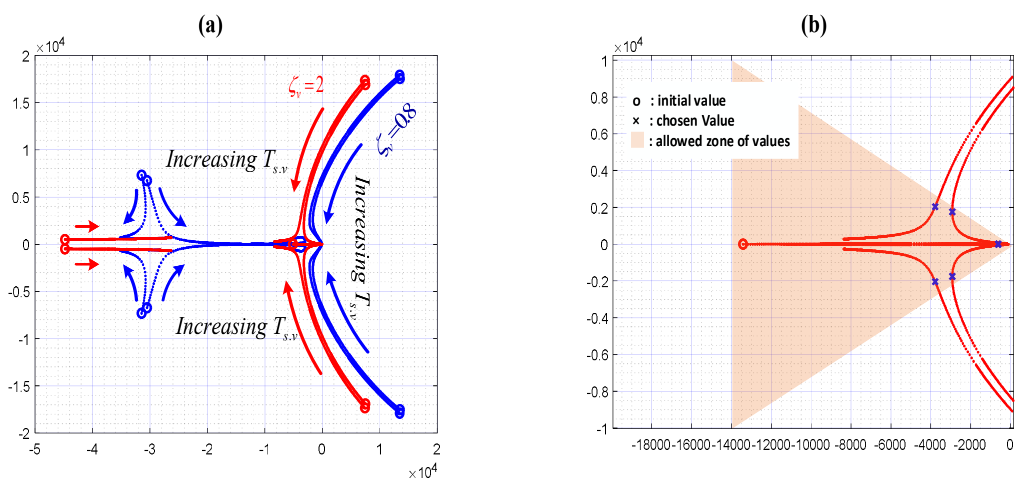

*Fig.II. 8 (a)Root-locus corresponding to the change of parameter **Ts**–v and (b) zoom for =1.2*

II.4.2 Robustness Assessment

In this subsection, the performance of the control is evaluated in terms of stability, where the influence of the filter parameters L_1, r_1 and C variation in the poles of the closed-loop models of both CCL and VCL is investigated. The resulting root locus plots are shown in Figs. II.9 and II.10 respectively.

From the two figures, it can be seen that the increase in L_1, r_1, and C values, guarantees a stable operation of both CCL and VCL, so it has a large range of variation.

It is concluded that the proposed design values of current and voltage controllers give high dynamic performance and robust stability under parameters variation.

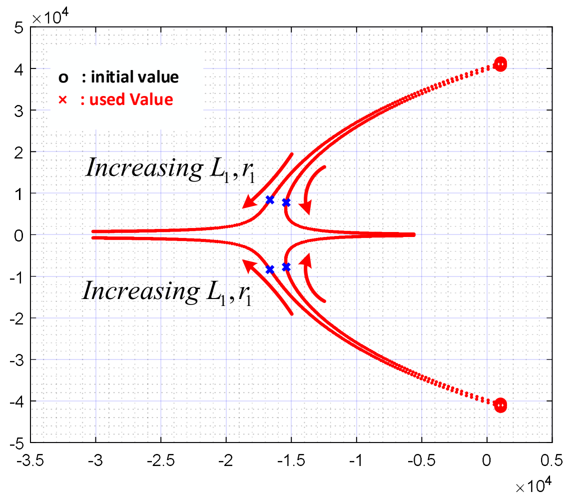

Fig.II. 9 Root-Locus corresponding to the change of the values of the parameters L_1 and r_1 on CCL.

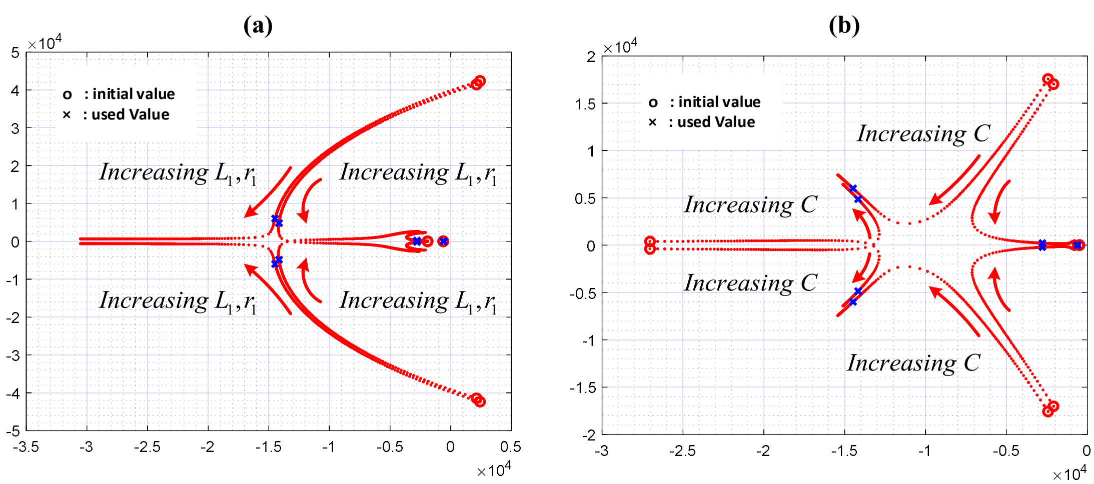

Fig.II. 10 Root-Locus corresponding to the change of the values of the parameters (a) L_1, r_1, and (b) C on VCL.

The proposed virtual control scheme based on the MSOGI method is highlighted in this section. However, before that, the droop control concept and modeling are first presented.

II.5 Proposed power-sharing Control Scheme

The power balance between different DG units is maintained by the *P-Q* power-sharing control. It includes, as shown in Fig. II.1, a VICL and a droop-based power control.

The droop control technique is an effective solution that has been adopted to coordinate the DG units within an MG. One of the major advantages of this control strategy is the ability to enable communication-less power-sharing among parallel-connected DG units. It adopts the calculated active and reactive powers as inputs and produces the output voltage reference of the inverter.

The operation principle of the droop method is based on adjusting the frequency (*f*), and voltage (*E)*, of an inverter in order to control the power balance. This concept is inspired by synchronous generators, which drop their frequency to inject more active power.

By using the droop method, the inverters' outputs and line impedances can affect the power-sharing accuracy. Also, feeding nonlinear loads creates current harmonics, therefore, a virtual impedance controller is proposed for enhancing the power-sharing performance. This VICL is introduced to improve the accuracy of the power-sharing and allow the share of current harmonics by normalizing the output impedance of the VSIs. As shown in Fig. II.11, this control block considers the output current of the inverter as an input and provides an output voltage to be subtracted from the droop voltage reference.

II.5.1 Droop Control

As discussed in Chapter I, the droop control unit includes a power calculation block with a Low Pass Filter (LPF), *f/P* and *V/Q* droop controllers, and a sinusoidal generator. In this control scheme, the droop controller respectively uses, to produce the frequency and voltage references (ω_i , E_i), the calculated average *P* and *Q* powers in the *αβ*-frame based on (II.25), below:

$$\begin{cases} P_i = \left(v_{c.\alpha} \times i_{L2.\alpha} + v_{c.\beta} \times i_{L2.\beta}\right) \\ Q_i = \left(v_{c.\beta} \times i_{L2.\alpha} - v_{c.\alpha} \times i_{L2.\beta}\right) \end{cases} \tag{II.25}$$

Next, a sinusoidal generator is used for generating the three-phase *abc* references of the inverter output voltage according to the following expression:

$$v^*_{droop}(t) = E_i \sin\left(\omega_i t + \begin{bmatrix} 0 & \frac{2\pi}{3} & -\frac{2\pi}{3} \end{bmatrix}^T\right) \tag{II.26}$$

To derive the droop functions, we should analyze the equivalent circuit of two VSIs connected in parallel to an AC bus via line impedances as given in Fig. II.11. In this figure, each inverter stage is modeled as a sinusoidal voltage source with an output impedance in series. According to this figure, the expression of the active P and reactive Q power of each DG, after some mathematical manipulation, can be obtained as follows:

$$\begin{cases} P_i = \dfrac{3V_{PCC}}{Z_i}\left(\left(E_i\cos(\varphi_i) - V_{PCC}\right)\cos(\phi_i) + E_i\sin(\varphi_i)\sin(\phi_i)\right) \\ Q_i = \dfrac{3V_{PCC}}{Z_i}\left(\left(E_i\cos(\varphi_i) - V_{PCC}\right)\sin(\phi_i) - E_i\sin(\varphi_i)\cos(\phi_i)\right) \end{cases} \tag{II.27}$$

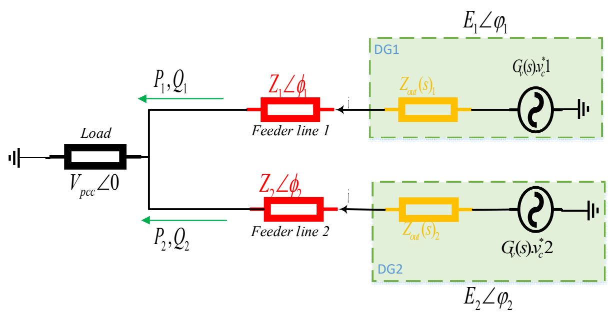

Fig.II. 11 Equivalent electric circuit of two paralleled VSIs

where $E_i\angle\varphi_i$ is the inverter output voltage, $E_{pcc}\angle 0$ is the voltage at the PCC, and $Z_i\angle\phi_i = R_i + jX_i$ is the inverter to the PCC bus impedance, which considers the inverter output impedance and the line impedance of the connection wires.

By assuming that the phase difference between the inverters' output voltages and the PCC, is very small, (φ_i <<1 $\rightarrow$sin $\varphi_i = \varphi_i$ and cos $\varphi_i = 0$), (II.26) yields:

$$\begin{cases} P_i = \dfrac{V_{PCC}}{Z_i}\left(\left(E_i - V_{PCC}\right)\cos(\phi_i) + E_i\varphi_i\sin(\phi_i)\right) \\ Q_i = \dfrac{V_{PCC}}{Z_i}\left(\left(E_i - V_{PCC}\right)\sin(\phi_i) - E_i\varphi_i\cos(\phi_i)\right) \end{cases} \tag{II.28}$$

Based on the line impedance nature: the expression of the active and reactive powers can be defined as follows:

- For pure inductive line impedance i.e., $X_i >> R_i$ $(\rightarrow Z_i\angle\phi_i \cong X_i\angle \pi/2)$:

$$\begin{cases} P_i = \dfrac{E_i V_{PCC}}{X_i}\varphi_i \\ Q_i = \dfrac{(E_i - V_{PCC})V_{PCC}}{X_i} \end{cases} \tag{II.29}$$

- For pure resistive line impedance i.e., $X_i << R_i$ $(\rightarrow Z_i\angle\phi_i \cong R_i\angle 0)$:

$$\begin{cases} P_i = \dfrac{(E_i - V_{PCC})V_{PCC}}{R_i} \\ Q_i = \dfrac{-E_i V_{PCC}}{R_i}\varphi_i \end{cases} \quad \text{(II.30)}$$

where X_i and R_i are the reactance and resistance of the inverter output impedance.

It can be noticed that in the case of pure inductive impedance, the active power depends on the phase angle (II.29), and the reactive power depends on the voltage (II.30). While, in the case of pure resistive impedance, the *f/Q* and *V/P* characteristics seen in the previous chapter are found.

Based on the aforementioned characteristics, the expressions of the droop controller can be formulated as follows:

- Pure inductive impedance:

$$\begin{cases} \omega_i = \omega^* - \left(\dfrac{\omega_f}{s+\omega_f}\right) nP_i \\ E_i = E^* - \left(\dfrac{\omega_f}{s+\omega_f}\right) mQ_i \end{cases} \quad \text{(II.31)}$$

- Pure resistive impedance:

$$\begin{cases} E_i = E^* - \left(\dfrac{\omega_f}{s+\omega_f}\right) nP_i \\ \omega_i = \omega^* - \left(\dfrac{\omega_f}{s+\omega_f}\right) mQ_i \end{cases} \quad \text{(II.32)}$$

where ω^* and E^* correspond to the nominal frequency and amplitude output voltage at no load. *n* and *m* are the frequency and amplitude droop gains which can be determined by the maximum frequency. and voltage deviations (Δf_{max} and ΔV_{max}) divided by the inverter active and reactive rated power, and the first-order transfer function is of the transfer function of the LPF with a cut-off frequency ω_f.

It is worth mentioning that in this work we considered the case of pure inductive impedance.

II.5.2 Proposed Virtual Impedance Control Loop

By using the droop method, the inverters' outputs, and line impedances as well as feeding nonlinear loads can affect the power-sharing accuracy. Therefore, an ESOGI-based virtual impedance control scheme is proposed for enhancing the power-sharing performance. The schematic of the designed VI intended for a three-phase VSI is depicted in Fig.II.12 . As shown, the ESOGI uses the output current of the *a*-phase ($i_{L2.a\text{-}in}$); obtained via the *abc*-*αβ* transform;

to extract the filtered direct and orthogonal fundamental components ($i_{L2.\alpha\beta}$). Note that the ESOGI uses the frequency provided by the droop control. The $\alpha\beta$-components are multiplied by the virtual inductance, L_v, and the fundamental frequency, ω. The resulting $\alpha\beta$ voltage components are transformed to *abc* voltages. These *abc* voltages are, then, added to the terms obtained from the multiplication of *abc*-components ($i_{L2.abc}$) with the virtual resistance, r_v, to obtain the output *abc*-voltages of the VI.

Accordingly, the output of the VI, in the *s*-domain, can be derived as follows:

$$v_{z-abc}(s) = r_v\, i_{L2.abc} - \left(T_{\alpha\beta-abc} \times \left(L_v \omega \times \begin{bmatrix} -i_{L2.\beta} & i_{L2.\alpha} \end{bmatrix}^T\right)\right) \quad \text{(II.34)}$$

where $T_{\alpha\beta\text{-}abc}$ defines the inverse Clarke transform.

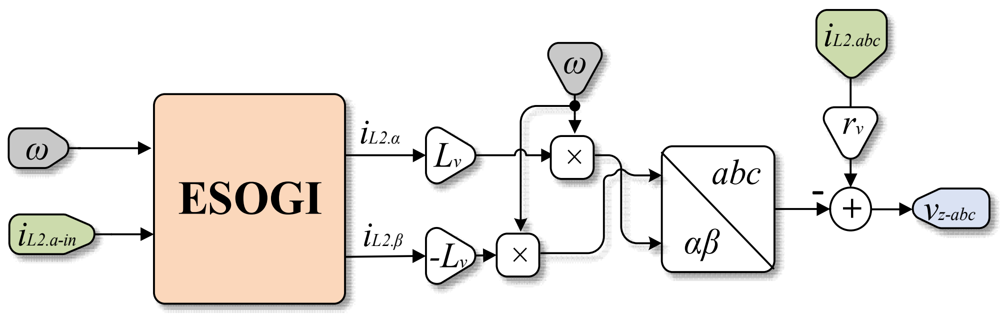

Fig.II. 12 Structure of the VI control scheme based on ESOGI.

The $\alpha\beta$ voltage components are transferred to *abc* frame and then, subtracted from the ones generated by the droop controllers, resulting in the new voltage reference defined as follows:

$$v_{C.ref}(s) = v_{droop.ref}(s) - v_z(s) \quad \text{(II.35)}$$

The structure of the ESOGI used to estimate the current components is presented in Fig. II.13. It consists of two second-order adaptive filters; tuned by the droop control frequency and an LPF. The adaptive filters are responsible for generating the $\alpha\beta$ current components from a single sinusoidal current. While the LPF is in charge of estimating the inherent dc offset in the input current. The outputs of the ESOGI are the direct component and the quadrature component free from the dc offset, which is achieved by subtracting the estimated dc offset from the shifted quadrature generated by the SOGI [11].

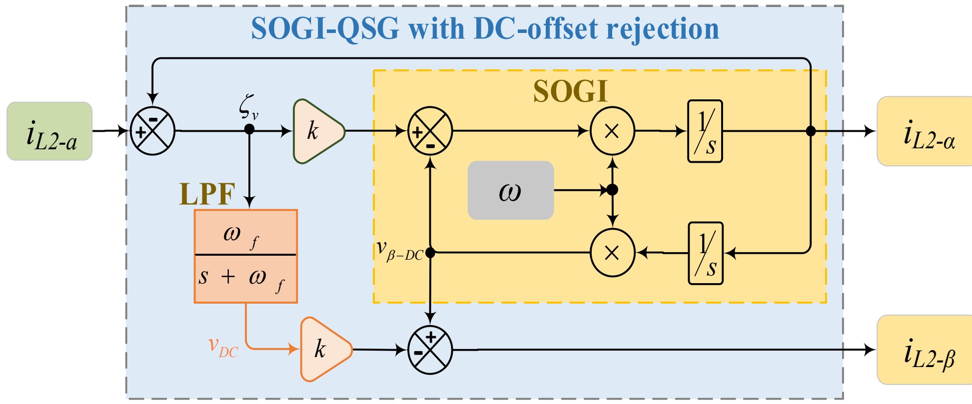

Fig.II. 13 Enhanced-SOGI structure.

The ESOGI can ensure the proper estimation of the current components with high accuracy even under a distorted current and fast dynamic response, in addition to its simplicity of implementation. This may lead to improving the droop control performance; therefore, an enhancement of the power-sharing accuracy is expected.

II.6 Simulation Results

To evaluate the proposed controller performance, the system illustrated in Fig. II.1 is simulated in the MATLAB/Simulink environment under different operating conditions and load variations.

The simulation tests were conducted under two steps, firstly, in subsection (II.6.1), the proposed cascaded inner controller is tested under different abnormal conditions. After proving its effectiveness, the whole control is tested in section (II.6.2) under different case studies, taking into consideration three DG units.

Table II.1 lists the parameters used in these simulation tests.

Table II. 1 Simulation parameters

Parameters	Symbol	Unit	Value
Nominal Voltage	E_n	V	220
Nominal frequency	f_n	Hz	50
Switching frequency	f_s	kHz	20
Simulation frequency	f_s	MHz	1
DC source voltage	U_{DC}	V	650 / 450z
Filter capacitor, inductor, resistor	C, L_1, r_1	μF, mH, Ω	23, 2, 1
Line impedance of DG#01	$Li1, ri1$	mH, Ω	1.5,0.8
Line impedance of DG#02	Li_2, ri_2	mH, Ω	0.5,0.8
Virtual inductance	L_v	mH	2.7

Virtual Resistance	R_v	Ω	1
P-ω droop	m	rad/(W. s)	0.0005
Q-V droop	n	V/Var	0.001
VCL PI gains	k_{pv} , k_{iv}	-	0.1839 , 183.87
CCL P gain	k_{pi}	-	6.2831
Linear load inductor	L_L ,r_L	mH, Ω	1, 150
Nonlinear load inductor	L_{nL} ,r_{nL}	mH, Ω	1, 1000
Nonlinear load capacitor	C_{nL}	μF	1000

II.6.1 Inner control performance investigation

In this subsection, the designed controller is tested under various operating variations, where the considered case studies are as follows:

<u>Case 01</u>: reference variation

Fig.II.15 illustrates the different perturbations applied on the inner control references when feeding linear load, such that:

- <u>Scenario 01</u>: voltage reference sag (E) of 0.2 p.u (ΔE) of its fundamental amplitude ($E*$) is performed at 0.1s.
- <u>Scenario 02</u>: a phase jump is introduced into the output voltage reference ($\Delta\varphi$) at 0.4s.
- <u>Scenario 03</u>: a step change of the inverter frequency ($\Delta\omega$) is set at 0.75s.

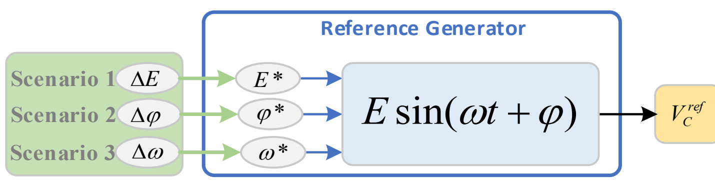

Fig.II. 14 Performed scenarios considering the reference key parameters variations

<u>Case 02:</u> load change

As shown in Table II.2, a linear load of 500W is first supplied at 0.1s, then the power is increased by 50% at 0.2s.

Table II. 2 Performed scenarios of load change.

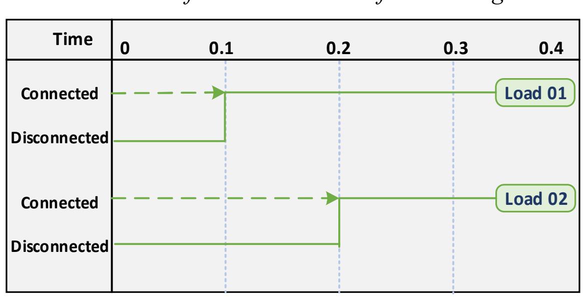

Note that the considered performance criteria for the designed control scheme are the transient and steady-state responses. The simulation results of the controller's performance tracking in terms of instantaneous output voltage and current in both *abc* and *dq* frames in response to case studies 1 and 2 are shown in Figs.II. 16-19.

Figs.II.16-17 demonstrate the effective and stable operation of the controller, in which, the inductor current tracks the reference current established by the VCL either if the amplitude/frequency value of the voltage reference has been changed or a phase jump happened. The same performance for the output voltage and its reference is achieved. Figs.II.18-19 show that an increase/decrease in power demand leads to an increase/decrease in the current, while the voltage is maintained stable. All the investigated cases demonstrate that the transient response of both voltage and current waveforms are well-damped, very fast, and without overshoot. Furthermore, the signals are relatively free of both switching frequency and low-order harmonic distortion. In conclusion, the control system can maintain stable voltage and frequency levels, even in the presence of external perturbations or load variations.

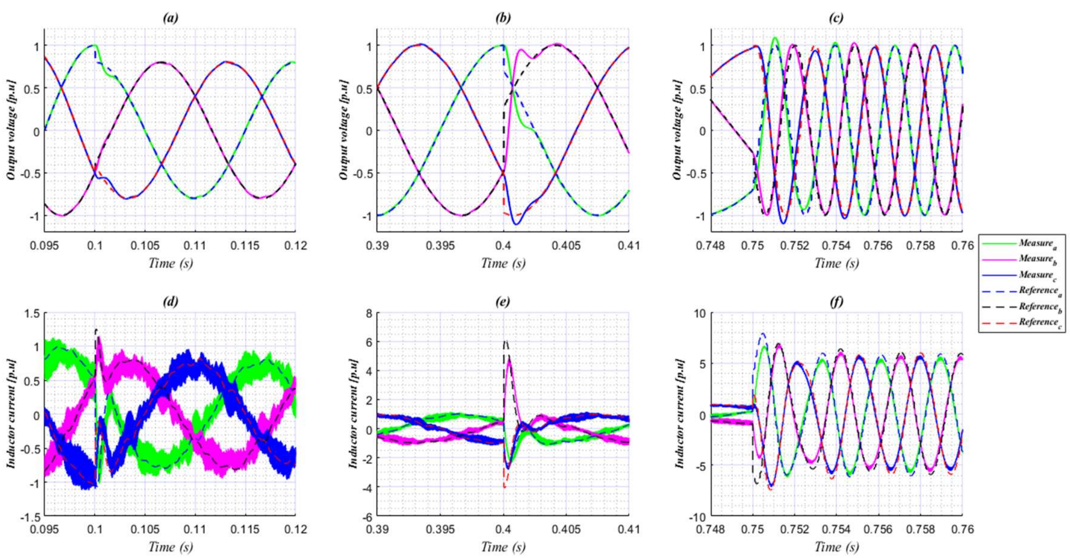

Fig.II. 15 Simulation results in response to case 01 in abc frame (a) output voltage for scenario 01 (b) output voltage for scenario 02 (c) output voltage for scenario 03 (d) Inductor current for scenario 01 (e) Inductor current for scenario 02 (f) Inductor current for scenario 03

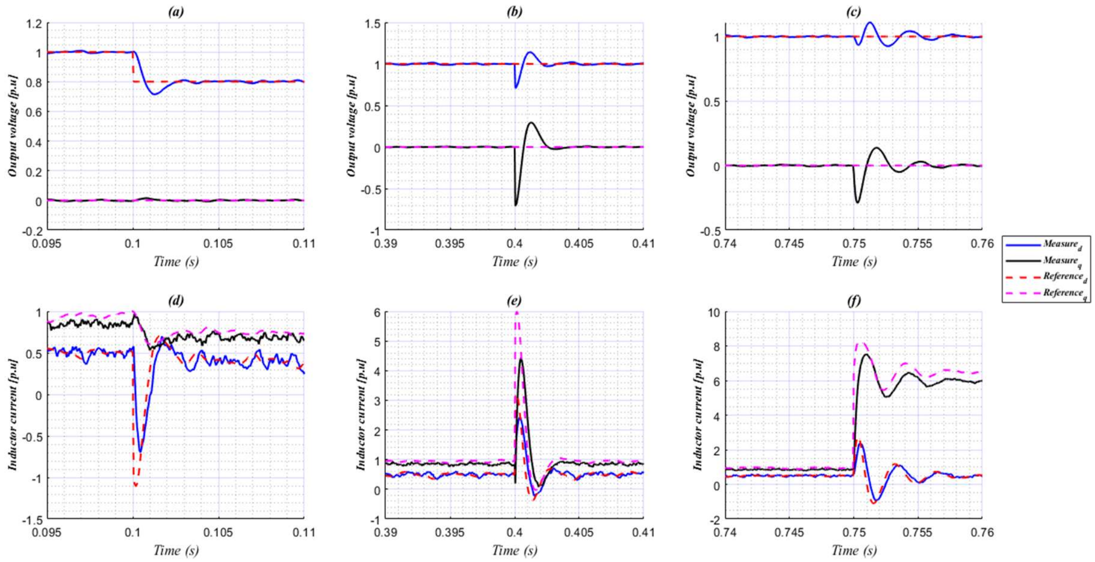

Fig.II. 16 Simulation results in response to case 01 in dq frame (a) output voltage for scenario 01 (b) output voltage for scenario 02 (c) output voltage for scenario 03 (d) Inductor current for scenario 01 (e) Inductor current for scenario 02 (f) Inductor current for scenario 03

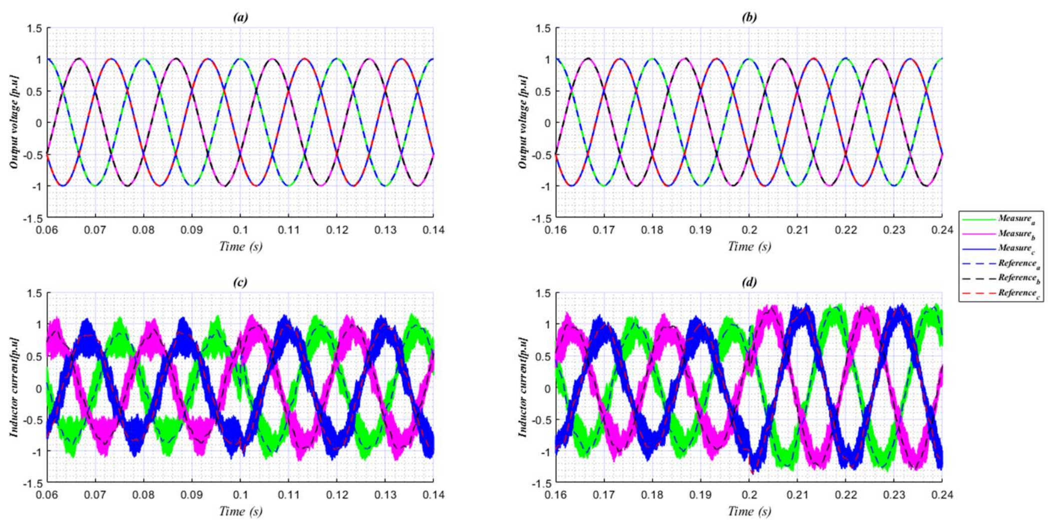

Fig.II. 17 Simulation results in response to case 02 in abc frame (a) output voltage for scenario 01 (b) output voltage for scenario 02 (c) Inductor current for scenario 01 (d) Inductor current for scenario 02

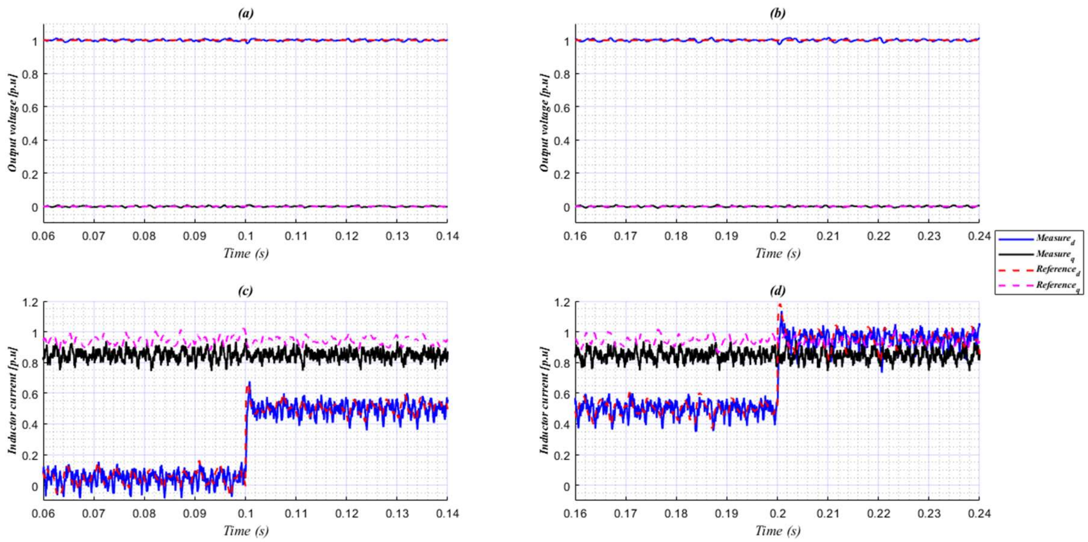

Fig.II. 18 Simulation results in response to case 02 in dq frame (a) output voltage for scenario 01 (b) output voltage for scenario 02 (c) Inductor current for scenario 01 (d) Inductor current for scenario 02

II.6.2 Power-sharing control performance investigation

To assess the effectiveness of the proposed power-sharing control scheme, an MG model; consisting of three inverters connected in parallel feeding a common load; as shown in Fig. II.20 is built in MATLAB/Simulink. The controller under study is configured according to the parameters presented in Table II.1. In this simulation, the performance of the designed controller is tested under various scenarios.

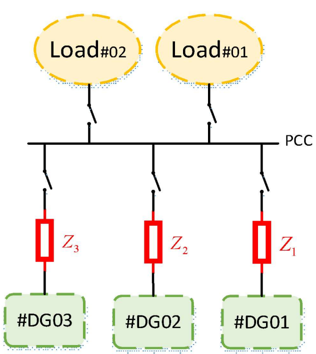

Fig.II. 19 Simulation network.

<u>Case 01:</u> Linear load changes

In this test, the DG units start with no load operation, and then a linear load is added at t = 0.05 s. Next, a second load is connected and disconnected at t = 0.2 s and 0.5 s respectively. The obtained results demonstrating the transient performance of the active power and frequency of

DG #1, #2, and #3 are shown in Figs. II.21-22. Fig. II.23 displays the plots of the output voltage and current at the PCC.

According to these results, the following remarks can be observed:

- At no-load operation, the active power, reactive power, and currents of DG #1, #2, and #3 are equal to zero, while the frequency and voltage are set to their nominal values. (i.e. 50 Hz and 220 V (RMS))
- When a load is connected, the active and reactive powers of the DGs are equal, which means that the load power is shared between the DG units. From Fig. II.21, it can be seen that the frequency drooped with a significant amount to inject the required active power, while the voltage almost remains unchanged since the reactive power is set to zero as shown in Fig. II.22. Regarding the voltage and current in the *abc* frame, given in Fig. II.23, it can be noticed that proper sinusoidal forms are achieved.
- The same observations are considered when the second load is connected and disconnected.
- High transient responses are achieved during load changes.

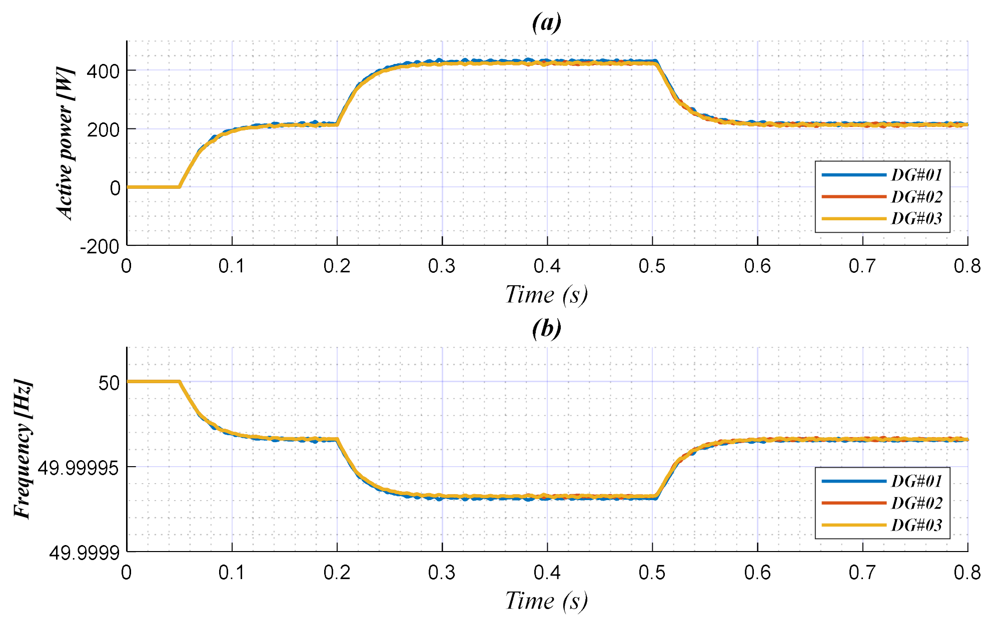

Fig.II. 20 Obtained results to load change: (a) active power and (b) frequency of VSI #1, #2, and #3.

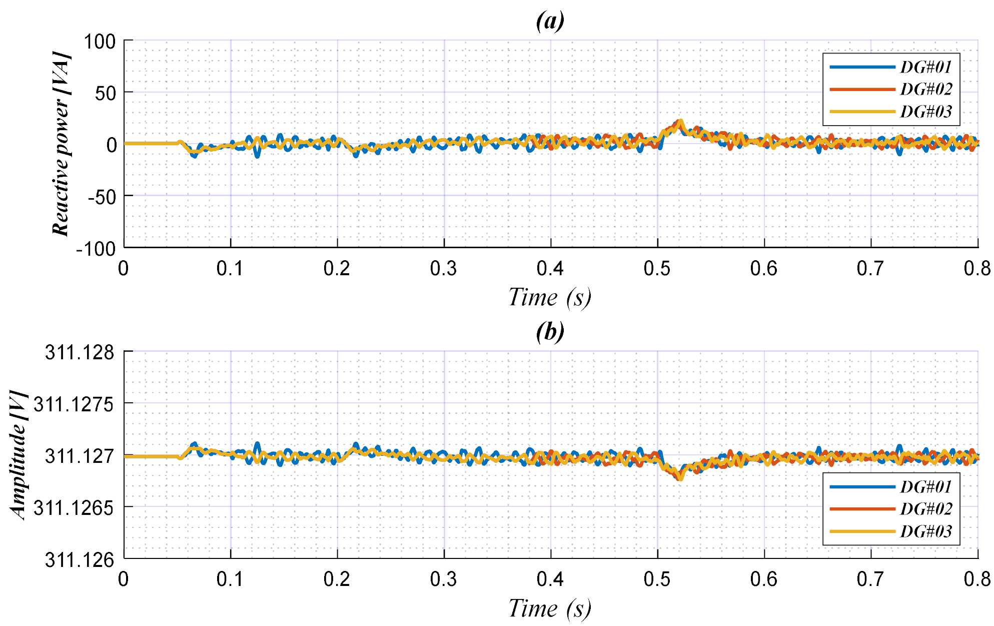

Fig.II. 21 Obtained results to load change: (a) reactive power and (b) amplitude of VSI #1, #2, and #3.

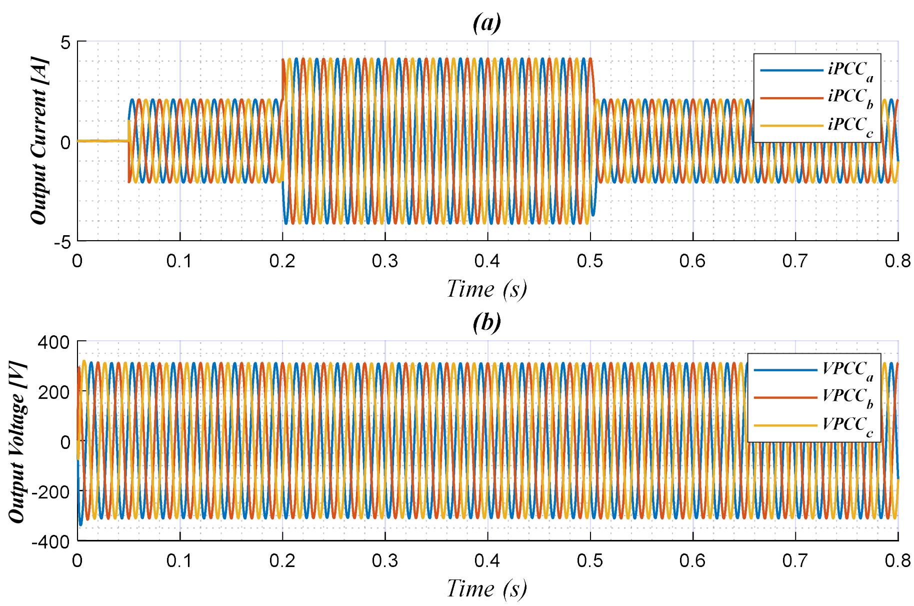

Fig.II. 22 Obtained results to load change: (a) current and (b) voltage at the PCC.

Case 02: Nonlinear load changes

In the following test, the proposed controller is subject to similar working conditions as in the first one, except using nonlinear loads. Figs. II.24-26 shows the obtained results, which show the same variables as the first scenario. They reveal that, as for linear load feeding in the first test, the proposed controller is able to distribute equally the active as well as reactive power, ensuring the MG output voltage and current stability.

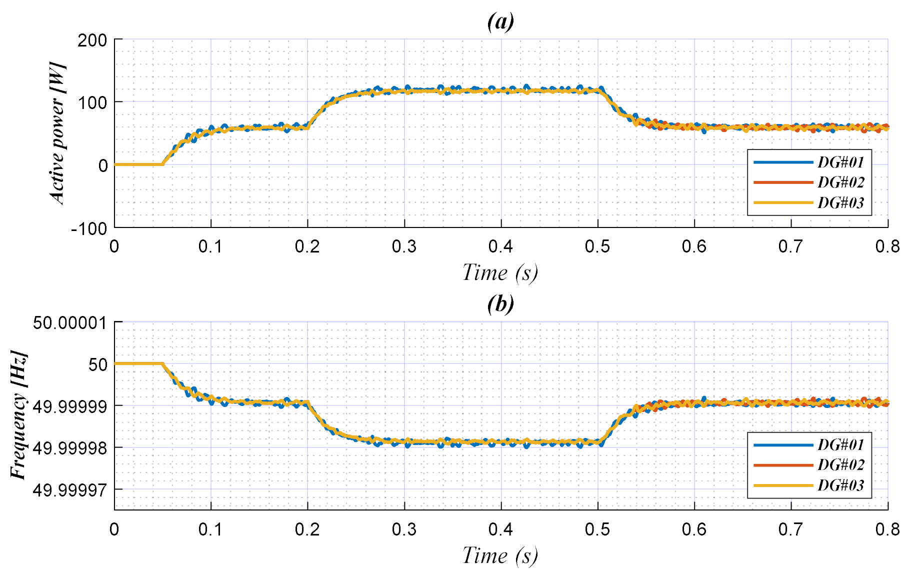

Fig.II. 23 Obtained results to nonlinear load change: (a) active power and (b) frequency of VSI #1, #2, and #3.

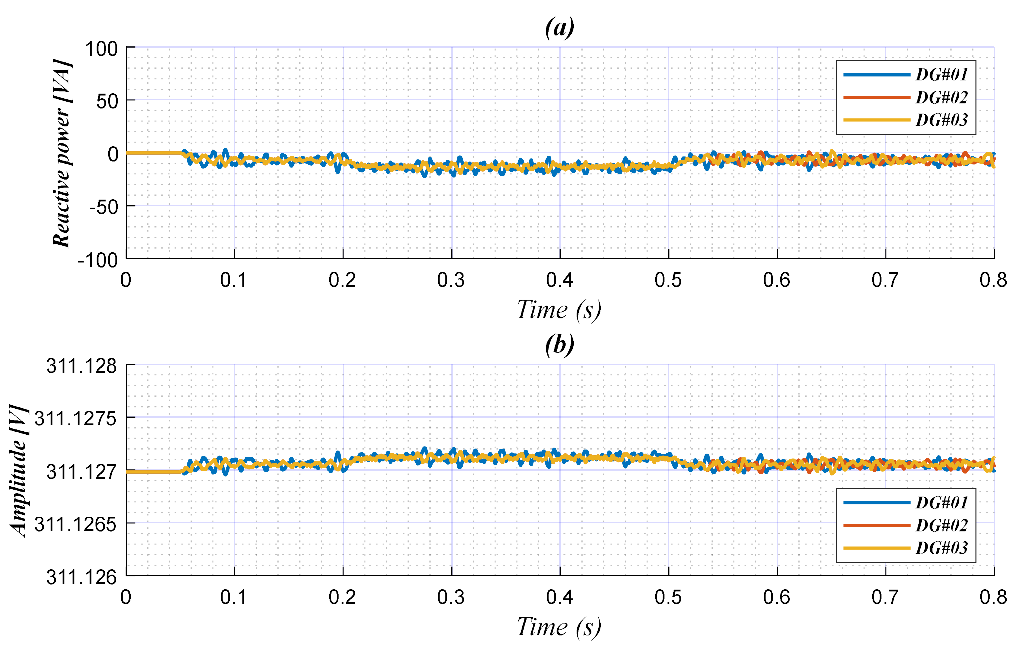

Fig.II. 24 Obtained results to nonlinear load change: (a) reactive power and (b) amplitude of VSI #1, #2, and #3.

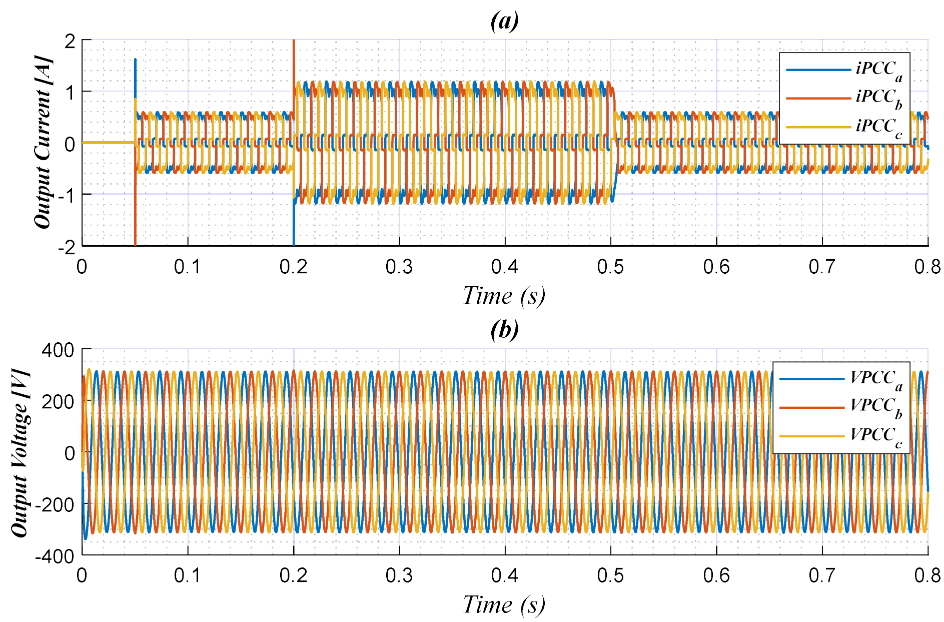

Fig.II. 25 Obtained results to nonlinear load change: (a) current and (b) voltage at the PCC.

Case 03: DG units plug in/out

Finally, the ability of the proposed control to handle the connection/disconnection of the DGs is tested. So, the first DG is the only one to supply the load from 0.1s. Then, DG #02 and DG#03 are connected at 0.3s and 0.6s respectively. Thereafter, DG#03 is disconnected again at 0.9 s. Figs.II.27-29 show the obtained results for this test and portray the same variables as the previous scenarios. From these plots, it can be observed that the proposed controller is able to handle the DGs connection and disconnection. In addition, it can be seen that the active and reactive are shared equally after the DGs are connected.

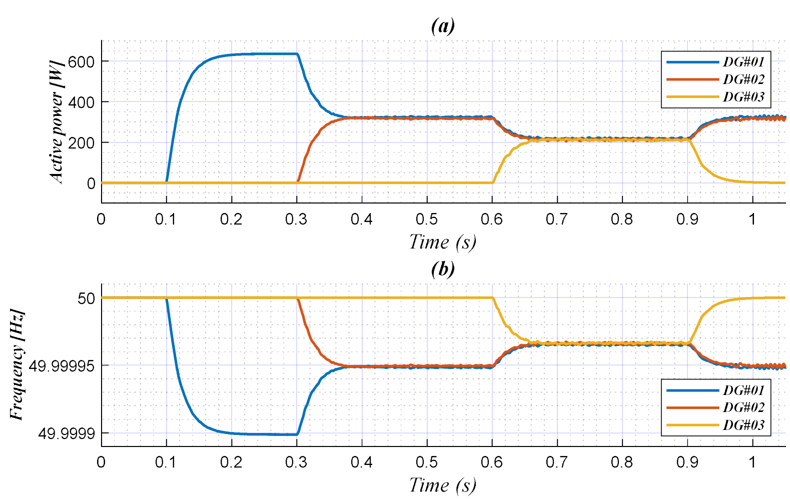

Fig.II. 26 Obtained results to DG plug in/out (a) active power and (b) frequency of VSI #1, #2, and #3

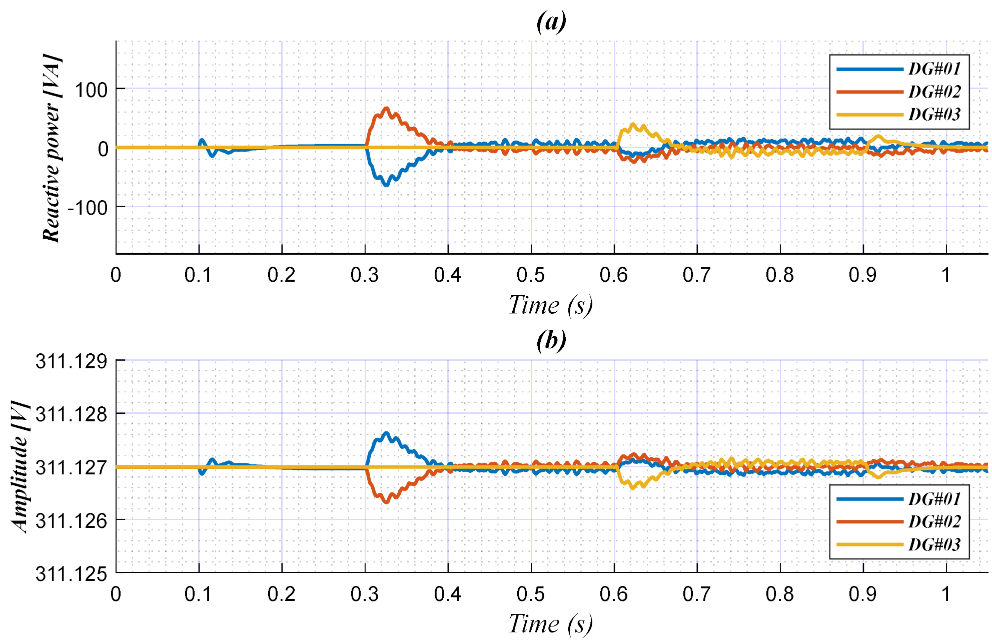

Fig.II. 27 Obtained results to DG plug in/out (a) reactive power and (b) amplitude of VSI #1, #2, and #3.

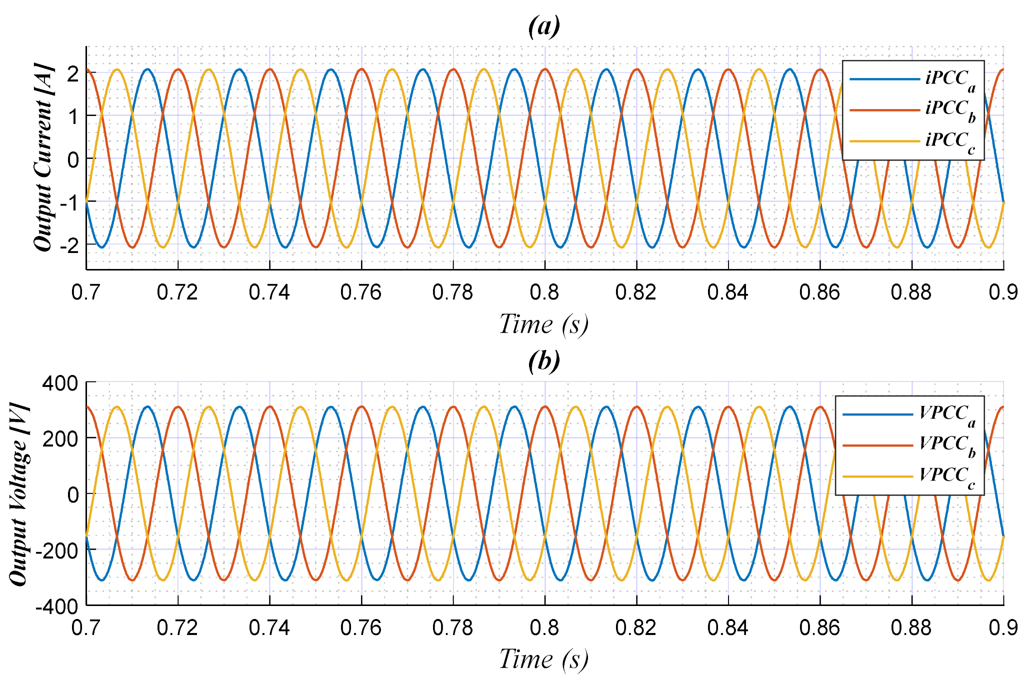

Fig.II. 28 Obtained results to DG plug-in/out (a) current and (b) voltage at the PCC

II.7 Conclusion

In this chapter, a detailed examination of primary control for a three-phase VSI based on MG was conducted. In addition, an extensive analysis of the inner control system, including modeling and design was performed. Furthermore, stability analyses and robustness assessment of the designed inner controller under various parameters variation was established. On the other hand, a power-sharing control approach employing a virtual impedance control scheme based on the MSOGI method, along with corresponding structures and formulations was also introduced. To assess the proposed controller's effectiveness, simulations were conducted using the MATLAB/SimPowerSystem environment.

The next chapter will cover the third major contribution of this thesis, which focuses on the design and analysis of the secondary and tertiary control levels based on ESOGI-FLL. The main goal is to effectively manage voltage amplitude and frequency variations caused by the inherent characteristics of the droop control strategy within three-phase MGs seen in this chapter, along with the power flow management.

Chapter 03 : Secondary and Tertiary Controls : Enhanced Implementation Intended for Three-Phase Inverters

III.1 Introduction

As has been shown in previous chapters, power converter-based MGs must be efficiently controlled in order to achieve key goals objectives including power-sharing, power quality enhancement, synchronization, and power flow management [141]. In the literature, the most popular method to accomplish these aims is hierarchical control, which combines primary, secondary, and tertiary control levels [43, 91] [142]. To maintain the steady operation of the DG units and to guarantee power sharing among them, primary control is conducted locally. On the other hand, secondary control becomes necessary to rectify frequency and amplitude changes caused by the inherent properties of the droop control and power quality improvement as well. In addition, while switching to grid connection mode, MG synchronization with the main utility grid is integrated smoothly inside the Secondary Control (SC) loop [94]. Furthermore, to address power flow dynamics and ensure a smooth and efficient functioning of the MG system, the tertiary controller assumes the responsibility of providing set-points to the lower control tiers.

The SC; which aims to restore the frequency and voltage at the PCC to their rated values when they deviate from their nominal ones because of the intrinsic properties of the droop control. It has drawn interest in both single and three-phase AC MGs [111, 115, 143-145]. For three-phase MGs, modeling and control design of the SC layer regarding frequency and amplitude restoration has been thoroughly covered in the literature, but they all agree that accurate modeling of MG frequency and voltage restoration control is still difficult to achieve, mostly because the related estimations contain unknown dynamics. In addition to the lack of a thorough parameter selection tuning technique for the PI controllers, which are essential to the restoration control process. Addressing these challenges, this chapter explores a thorough explanation of a secondary control scheme designed for effective DC offset rejection, based on the DESOGI-FLL. This is achieved by a comprehensive analysis of the dynamics inherent in the DESOGI-FLL. Furthermore, this chapter focuses on the design, modeling, analysis, and tuning of tertiary control using the DESOGI-FLL scheme for a three-phase VSI-based droop-controlled MG running in grid-connected mode. It seeks to improve the performance of power flow regulation while reducing the computational load related to the accuracy and computation time of the provided quantities.

The suggested scheme is introduced within the context of an islanded AC MG's hierarchical control structure, as shown in Fig. III.1. It is composed of two parallel DG units using three-phase VSIs, considering primary control, secondary and tertiary controls based on DESOGI-FLL. According to this scheme, each DG is equipped with its own local controller that is linked to a local load and the utility grid via a common AC bus. Wherein the DESOGI-FLL scheme is introduced to precisely estimate the key parameters of the MG.

To validate our proposals, we implement a model, including a hierarchical control scheme inclusive of traditional droop control and the proposed secondary and tertiary control loops. These tests involve 3 three-phase parallelled inverters and intend to confirm our method's efficacy and resilience in a range of operating scenarios. The obtained findings from this research effort substantiate our modeling approach, showing the expected transient response and excellent disturbance rejection in the MG.

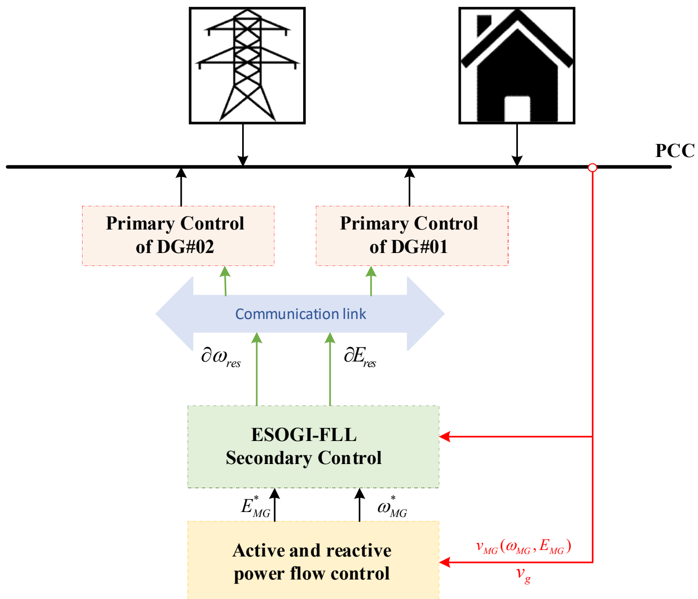

Fig.III. 1 Hierarchical control of two three-phase VSIs-based islanded AC MG, considering primary, secondary, and tertiary control levels.

III.2 The Proposed Secondary Control Scheme for Three-Phase Droop Controlled Islanded MG

The block diagram of the suggested hierarchical control strategy for two three-phase inverters coupled in parallel to generate an islanded AC MG is depicted in Fig. III.2 The power inverter-based DGs are connected to the same AC bus via a line inductive impedance. This AC bus is also connected to the utility grid and the local load. Each DG unit is made up of a VSI fed by a DC source and an LC filter that enables high-frequency content cancellation [146]. As shown in Fig. III.2, primary and secondary control levels make up the hierarchical control of the islanded MG in this system.

The primary level presented in this work is based on droop control, and operates strictly on a local scale, managing the challenging task of active and reactive power sharing among DG units without requiring communication. In addition to the voltage and current control loops, it also contains the power calculations block and the virtual impedance loop. All of these power blocks were covered in great detail in the last chapter.

Then, the secondary controller is introduced to restore the frequency and voltage at the PCC to their nominal values since they vary from them due to the nature of droop control. At this control level, the MG's frequency and amplitude, as well as the orthogonal components of both, the MG and the utility grid, are estimated by the DESOGI-FLL. Two distinct control loops are then developed: synchronization and restoration.

Fig.III. 2 Hierarchical control diagram for two paralleled DG units

In the synchronization phase, the phase angle difference between the utility grid and the MG is calculated using the orthogonal components of the PCC and grid voltages that are extracted, using DESOGI-FLL with Positive Sequence Detector (PSD), then passed through a P controller to achieve alignment. The resulting control signal is employed to update the frequency reference in the restoration control loop.

As we proceed to the restoration stage, the estimated frequency and amplitude $\hat{\omega}_{MG}$, $\hat{E}_{MG}$ are compared to their desired nominal values ω^*_{MG} , E^*_{MG} , and then, PI controllers process these values and provide the required modifications for the actual frequency and amplitude. A low bandwidth communication channel is then used to send the resulting control signals, which are designated as $\partial\omega_{res}$ and ∂E_{res} , to the primary control level. This makes it easier for the intended nominal values to be recovered inside this later.

The formulations for the frequency and amplitude restoration compensators based on the PI controller, unfold as follows:

$$\begin{cases} \partial\omega_{res} = \int k_{i1}((\omega_{MG}^{*} + \partial\omega_{syn}) - \omega_{MG})dt - k_{p.f}\omega_{MG} \\ \partial E_{res} = \int k_{i.E}(E_{MG}^{*} + E_{MG})dt - k_{p.E}E_{MG} \end{cases} \quad \text{(III.1)}$$

In this equation, $k_{p.f}, k_{i.f}, k_{p.E}$ and $k_{i.E}$ represent the gains of the frequency and voltage controllers, respectively. Meanwhile, $\partial\omega_{syn}$ stands for the synchronization control signal, which, in the absence of the grid, is set to zero.

To assess the stability of the MG and appropriately set the parameters for frequency and voltage secondary control, precise dynamic models are formulated. The upcoming section outlines the proposed method for creating these models and the process for adjusting the control parameters.

III.3 Modeling of the Secondary Control

The main goal of the suggested modeling approach is obtaining accurate dynamic models for the SC for restoring frequency and amplitude in a three-phase AC MG. The idea behind is to apply the generated frequency and amplitude estimated dynamics of DESOGI-FLL to the secondary control modeling.

The whole restoration control model in the SC stage is shown in Fig. III.3. It includes models for communication delays, frequency and amplitude restoration controllers, and DESOGI-FLL frequency and amplitude estimation. It also demonstrates how the restoration model introduces the models for droop control, power calculations, and the inner control loops of the primary control stage. The line impedance model, a crucial element that shows the frequency and amplitude shift from the VSIs to the PCC, is also included.

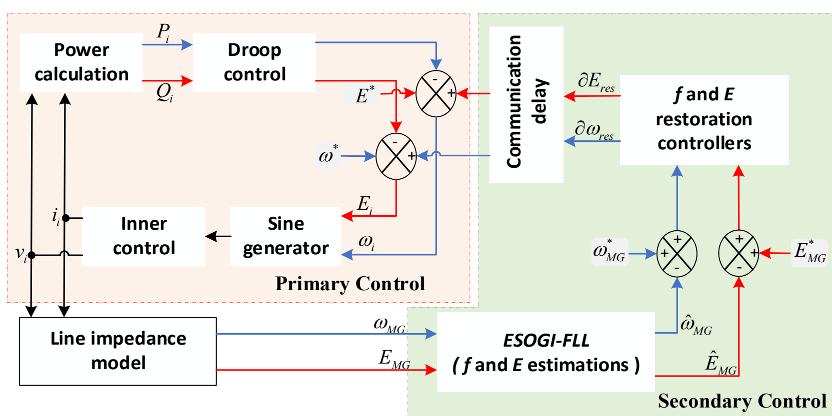

Fig.III. 3 DESOGI-FLL based restoration control loop model.

The modeling of the DESOGI-FLL scheme is presented in the next paragraph with an emphasis on the frequency dynamic. Simultaneously, a phasor domain theoretical analysis is carried out to uncover the dynamics of voltage estimation. The DESOGI-FLL-based frequency and amplitude restoration control modeling is developed in the next subsection, assuming that because of its quick response, the dynamics of the inner controller are negligible. The line impedance model is likewise neglected throughout this procedure. The following subsections further examine the tuning process based on the developed mathematical models, as well as the synchronization modeling and design analysis.

III.3.1 Modeling Analysis of the DESOGI-FLL

The DESOGI-FLL technique, which introduces an additional loop for the estimation/rejection of the DC component, is an adaptive second-order filter used to estimate the essential characteristics of a three-phase input voltage [110]. Fig. III.4 shows the block diagram of the DESOGI-FLL structure. It is made up of : an FLL and two ESOGI-based Quadrature Signal Generator (ESOGI-QSG). The primary function of the ESOGI-QSG block is to extract the direct and orthogonal voltage components, which can be utilized to determine the voltage amplitude. The operational frequency that will be supplied to the ESOGI-QSG blocks is estimated by the FLL. Further details regarding this plan can be found in [110].

The relationship between the input MG voltage and the extracted orthogonal components ($\hat{v}_{MG_\alpha}$, $\hat{v}_{MG_\beta}$) can be described by the following closed-loop transfer functions [147], as shown in Fig.III.4:

$$\begin{cases} G_\alpha(s) = \dfrac{\hat{v}_{MG_\alpha}(s)}{v_{MG}(s)} = k\hat{\omega}_{MG}\dfrac{s}{s^2 + k\hat{\omega}_{MG}s + \hat{\omega}_{MG}^2} \\ G_\beta(s) = \dfrac{\hat{v}_{MG_\beta}(s)}{v_{MG}(s)} = \dfrac{k(\hat{\omega}_{MG}^2 - \omega_f s)}{s + \omega_f}\dfrac{s}{s^2 + k\hat{\omega}_{MG}s + \hat{\omega}_{MG}^2} \\ G_{\beta-DC}(s) = \dfrac{\hat{v}_{MG_{\beta-DC}}(s)}{v_{MG}(s)} = \dfrac{k\hat{\omega}_{MG}^2}{s^2 + k\hat{\omega}_{MG}s + \hat{\omega}_{MG}^2} \end{cases} \qquad \text{(III.2)}$$

In this equation *s* represents the Laplace variable, $\hat{\omega}_{MG}$ and ω_f stands for the estimated and the additional block frequencies, while *k* denotes the gain of the SOGI-QSG, a parameter conventionally set to ($1/\sqrt{2}$) [148].

It is important to note that the dynamic of FLL based on SOGI is used instead of the ESOGI since it is assumed that there is no DC component present in the inputs of the ESOGI-FLL. Consequently, the FLL frequency adaptation loop's simplified transfer function can be written as follows [149]:

$$\hat{\omega}_{MG} = \frac{\Gamma}{s + \Gamma}\omega_{MG} \qquad \text{(III.3)}$$

where, ω_{MG} denotes the input frequency, while Γ represents the gain of the FLL. This gain is related to the FLL controller gain γ, as depicted in Fig.III.4, expressed through the following relationship [149]:

$$\gamma = \frac{k\hat{\omega}_{MG}}{\hat{E}_{MG}^2}\Gamma \qquad \text{(III.4)}$$

Indeed, Eq. (III.3) can be viewed as a model for the dynamics of frequency estimation as it expresses the relationship between the input and the estimated frequencies.

Authors in [150] provided more information with theoretical analysis and simulation study using MATLAB/Simulink in order to confirm the accuracy of the produced frequency and amplitude models.

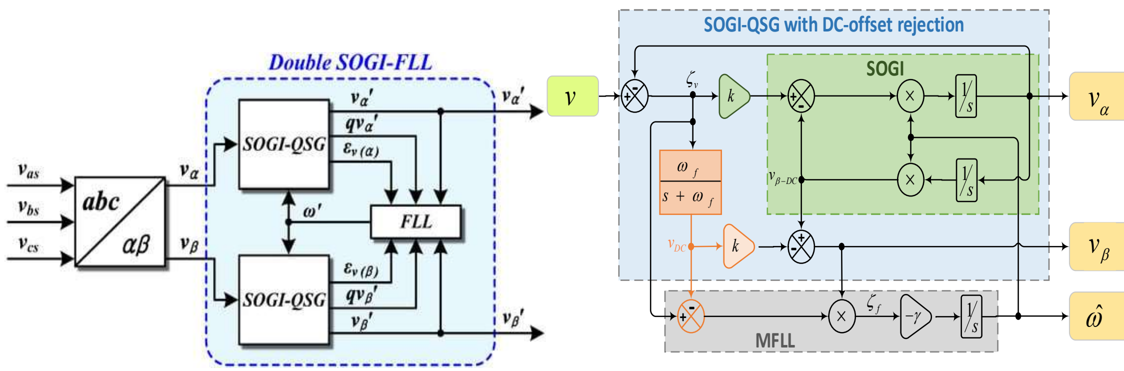

Fig.III. 4 The structure of (a) DESOGI -FLL and (b) ESOGI-FLL

III.3.2 Modeling of the frequency and amplitude restoration loops

Figs. III.5 (a) and (b) display the block diagram of the voltage amplitude and frequency control model, respectively.

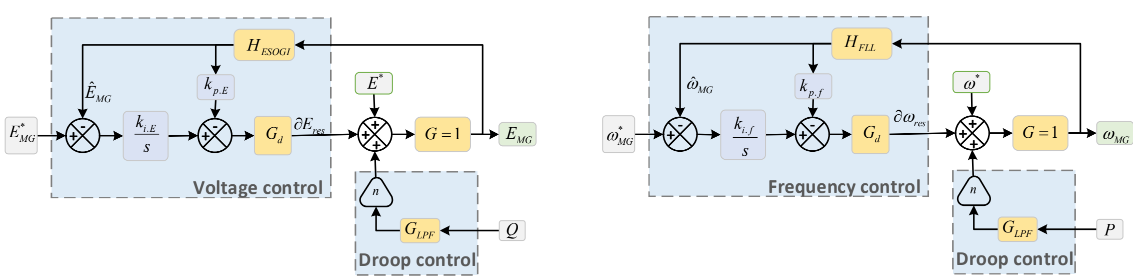

(a) **(b)**

Fig.III. 5 Secondary's (a) voltage control block diagram (b) frequency control block diagram

Based on this figure, the voltage and frequency restoration closed-loop transfer function can be obtained as follows:

$$\begin{cases} E_{MG} = \dfrac{\left[\dfrac{k_{i.E}}{s}\right] G_d(s)}{1 + G_{PI.E}(s) H_{SOGI}(s) G_d(s)} E_{MG}^{*} - \dfrac{n G_{LPF}(s)}{1 + G_{PI.E}(s) H_{SOGI}(s) G_d(s)} Q \\ \omega_{MG} = \dfrac{\left[\dfrac{k_{i.f}}{s}\right] G_d(s)}{1 + G_{PI.f}(s) H_{FLL}(s) G_d(s)} \omega_{MG}^{*} - \dfrac{m G_{LPF}(s)}{1 + G_{PI.f}(s) H_{FLL}(s) G_d(s)} P \end{cases} \quad \text{(III.5)}$$

where:

$$\begin{cases} G_{PI.E}(s) = \dfrac{k_{P.E} s + k_{i.E}}{s} \\ G_d(s) = \dfrac{1}{\tau s + 1} \\ G_{LPF}(s) = \dfrac{\omega_f}{s + \omega_f} \\ H_{SOGI}(s) = \dfrac{k \dfrac{\omega_{MG}}{2}}{(s + k \dfrac{\omega_{MG}}{2})} \end{cases} \qquad \begin{cases} G_{PI.f}(s) = \dfrac{k_{p.f} s + k_{i.f}}{s} \\ H_{FLL}(s) = \dfrac{\Gamma}{s + \Gamma} \end{cases} \quad \text{(III.6)}$$

τ represents the time delay of the communication link, and G_{LPF} a low-pass filter is utilized for reactive power calculation, with a cut-off frequency set at $\omega_f = 2\pi \times 20$.

Incorporating Equations (III.6) into (III.5), provides the complete mathematical description of the restoration control model given as follows:

$$\begin{cases} E_{MG} = \left[\dfrac{k_{i.E} s^2 + a\ k_{i.E} s + c}{s^3 + a\ s^2 + b\ s + c}\right] \left[\dfrac{1}{s(\tau s + 1)}\right] E_{MG}^{*} - \dfrac{n(s^2 + a\ s + \dfrac{c}{k_{i.E}})}{s^3 + a\ s^2 + b\ s + c} \left[\dfrac{\omega_f}{s + \omega_f}\right] Q \\ \omega_{MG} = \left[\dfrac{k_{i.f} s^2 + a\ k_{i.f} s + c}{s^3 + a\ s^2 + b\ s + c}\right] \left[\dfrac{1}{s(\tau s + 1)}\right] \omega_{MG}^{*} - \dfrac{m(s^2 + a\ s + \dfrac{c}{k_{i.f}})}{s^3 + a\ s^2 + b\ s + c} \left[\dfrac{\omega_f}{s + \omega_f}\right] P \end{cases} \quad \text{(III.7)}$$

with:

$$\begin{cases} a = k \dfrac{\omega_{MG}}{2} + \dfrac{1}{\tau} \\ b = k \dfrac{\omega_{MG}}{2\tau} (1 + k_{p.E}) \\ c = k_{i.E} k \dfrac{\omega_{MG}}{2\tau} \end{cases} \qquad \begin{cases} a = \Gamma + \dfrac{1}{\tau} \\ b = \dfrac{\Gamma}{\tau} (1 + k_{p.f}) \\ c = k_{i.f} \dfrac{\Gamma}{\tau} \end{cases} \quad \text{(III.8)}$$

III.3.3 Tuning Control Parameters

Based on the acquired models, the subsequent analysis is created in order to appropriately choose the parameters of the frequency and amplitude restoration control. The transfer functions that connect the desired frequency and amplitude to the actual ones can be obtained using Equations (III.7) as follows:

$$\begin{cases} E_{MG} = \left[\dfrac{k_{i.E}s^2 + a\,k_{i.E}s + c}{s^3 + a\,s^2 + b\,s + c}\right]\left[\dfrac{1}{s(\tau s+1)}\right]E_{MG}^* \\ \omega_{MG} = \left[\dfrac{k_{i.f}s^2 + a\,k_{i.f}s + c}{s^3 + a\,s^2 + b\,s + c}\right]\left[\dfrac{1}{s(\tau s+1)}\right]\omega_{MG}^* \end{cases} \quad \text{(III.9)}$$

By assuming that the perturbation amount of the droop model is likewise small and that the time delay is negligible with respect to the SOGI-FLL estimate time, equations (III.9) become as follows:

$$\begin{cases} E_{MG} = \dfrac{k_{i.E}k\dfrac{\omega_{MG}}{2}}{s^2 + k\dfrac{\omega_{MG}}{2}(1+k_{p.E})s + k_{i.E}k\dfrac{\omega_{MG}}{2}}E_{MG}^* \\ \omega_{MG} = \dfrac{\Gamma k_{i.f}}{s^2 + \Gamma(1+k_{p.f})s + \Gamma k_{i.f}}\omega_{MG}^* \end{cases} \quad \text{(III.10)}$$

Where these transfer functions' characteristics polynomials are:

$$\begin{cases} s^2 + \underbrace{k\dfrac{\omega_{MG}}{2}(1+k_{p.E})}_{2\zeta_E\omega_{n.E}}s + \underbrace{k_{i.E}k\dfrac{\omega_{MG}}{2}}_{\omega_{n.E}^2} = 0 \\ s^2 + \underbrace{\Gamma(1+k_{p.f})}_{2\zeta_f\omega_{n.f}}s + \underbrace{\Gamma k_{i.f}}_{\omega_{n.f}^2} = 0 \end{cases} \quad \text{(III.11)}$$

Being ζ and ω_n represent the damping factor and the natural frequency, respectively.

Hence, the proportional and integral gains for both amplitude and frequency controllers can be expressed as follows:

$$\begin{cases} k_{p.E} = \dfrac{4\zeta_E\omega_{n.E}}{k\omega_{MG}} - 1 \\ k_{i.E} = \dfrac{2\omega_{n.E}^2}{k\omega_{MG}} \end{cases} \quad \begin{cases} k_{p.f} = \dfrac{4\zeta_f\omega_{n.f}}{\Gamma} - 1 \\ k_{i.f} = \dfrac{2\omega_{n.f}^2}{\Gamma} \end{cases} \quad \text{(III.12)}$$

The corresponding natural frequency can be determined in relation to the desired settling time of the control response by choosing a suitable value for the damping factor ζ that can optimally ensure a trade-off between overshoot and settling time. Equations (III.12) can be used to calculate the controller parameters once ζ and ω_n have been selected.

III.4 Synchronization control loop

In this section, the synchronization control loop modeling and design are conducted. The synchronization control scheme is seamlessly integrated into the secondary control layer as depicted in Fig.III.2. Accordingly, its expression can be outlined as follows:

$$\partial\omega_{syn} = k_{p.\phi}(\phi^* - \phi) \qquad \text{(III.13)}$$

Where $k_{p.\phi}$ is the proportional gain term of the synchronization controller, ϕ is the phase difference between the MG and the main grid, and ϕ^* is the phase angle reference, set to zero.

To derive the phase angle difference ϕ, the cross-product mathematical formulas are used. The first formula defines the cross product of the MG, and the main grid voltages can be given by [26]:

$$\left\|\vec{v}_g \times \vec{v}_{MG}\right\| = \hat{V}_g \hat{E}_{MG} \sin(\phi) \qquad \text{(III.14)}$$

where $\hat{V}_g$ is the estimated voltage amplitude of the main grid.

The second formula of the cross-product within the stationary reference frame is given as follows:

$$\left\|\vec{v}_g \wedge \vec{v}_{MG}\right\| = \hat{v}_{g\,\alpha}\hat{v}_{MG\,\beta} - \hat{v}_{MG\,\alpha}\hat{v}_{g\,\beta} \qquad \text{(III.15)}$$

Here, the terms $v_{MG\,\alpha\beta}$ and $v_{g\,\alpha\beta}$ represent the extracted orthogonal components of the MG and the main grid voltages.

The phase angle difference expression can be derived by subtracting Equation (III.14) from Equation (III.15) and considering a small phase angle variation, i.e., $\sin(\phi) \approx \phi$, and given by:

$$\phi = \frac{\hat{v}_{g\,\alpha}\hat{v}_{MG\,\beta} - \hat{v}_{MG\,\alpha}\hat{v}_{g\,\beta}}{\hat{V}_g \hat{E}_{MG}} = \frac{\hat{v}_{g\,\alpha}\hat{v}_{MG\,\beta} - \hat{v}_{MG\,\alpha}\hat{v}_{g\,\beta}}{\hat{E}_{MG}^2} \qquad \text{(III.16)}$$

Thus, Equation (III.13) becomes:

$$\partial\omega_{syn} = -k_{p.\phi}\frac{\hat{v}_{g\,\alpha}\hat{v}_{MG\,\beta} - \hat{v}_{MG\,\alpha}\hat{v}_{g\,\beta}}{\hat{E}_{MG}^2} \qquad \text{(III.17)}$$

A constructed control model with the goal of adjusting the synchronization controller's parameter ($k_{p.\phi}$) is shown in Fig. III.6. This phase angle control diagram includes both the synchronization control model and the plant model ($G_\phi(s)$), as may be shown.

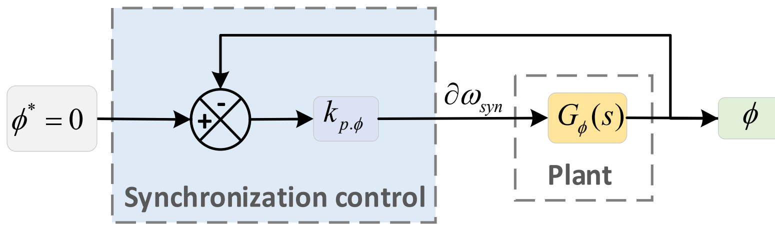

Fig.III. 6 Synchronization feedback control scheme

This representation allows the following equation to be obtained as the closed-loop transfer function of the phase angle control:

$$\phi = \frac{k_{p.\phi} G_\phi(s)}{1 + k_{p.\phi} G_\phi(s)} \phi^* \qquad \text{(III.18)}$$

The plant model $G_\phi(s)$ is defined by the expression:

$$G_\phi(s) = \frac{1}{s} \qquad \text{(III.19)}$$

By substituting Equation (III.19) into (III.18), we can derive the closed-loop model of the phase angle control as follows:

$$\phi = \frac{k_{p.\phi}}{s + k_{p.\phi}} \phi^* \qquad \text{(III.20)}$$

Applying the first-order control design concept to the transfer function given by Equation (III.20), we can calculate the proportional gain $k_{p.\phi}$ using the following expression:

$$k_{p.\phi} = -\frac{1}{T_s} \ln(0.02) \qquad \text{(III.21)}$$

where T_s is the desired settling time.

III.5 The proposed tertiary control scheme for three-phase MG

The MG can operate both independently and in conjunction with the main grid, as was previously noted. In grid-tied mode, the MG's power generation can exceed local consumption, particularly when renewable energy sources, such as: energy storage devices, are producing at their peak. As a result, excess active and reactive power is sent via an inverter and line impedance to the main AC grid. On the other hand, the main grid supplies additional power to meet demand in the event that the MG's supply is insufficient.

As a centralized controller, the tertiary control level is responsible for managing the bidirectional power transfer between the distributed generation units in the MG and the main grid at the PCC by controlling the flow of both active and reactive power [40]. The distributed generation units' voltage amplitudes and frequency can be changed to regulate this power exchange. It's crucial to remember that, in comparison to the secondary and primary controls at lower levels, this control level often displays a slower dynamic reaction.

The suggested tertiary controller, which is based on the DESOGI-FLL scheme, and the power stage of a three-phase MG running in grid-tied mode are shown in Fig. III.7. The load in this configuration is linked to the AC common bus, where the DG units share the load power demand equally. The suggested tertiary control scheme comprises of a PI controller and a DESOGI-FLL-based power calculation block, as shown in Fig. III.7. The direct and quadrature components of the grid voltage and current are estimated using the DESOGI-FLL. Equation (I.1) presented in Chapter I is used to calculate the active and reactive power of the grid using the predicted components. Based on the computed powers P_g and Q_g, the PI controller modifies the MG's active and reactive power references. The corrected references for the MG, represented as f_{MG} and E_{MG}, respectively, are then transmitted to the secondary control level by the tertiary control along with the updated frequency and voltage amplitude values.

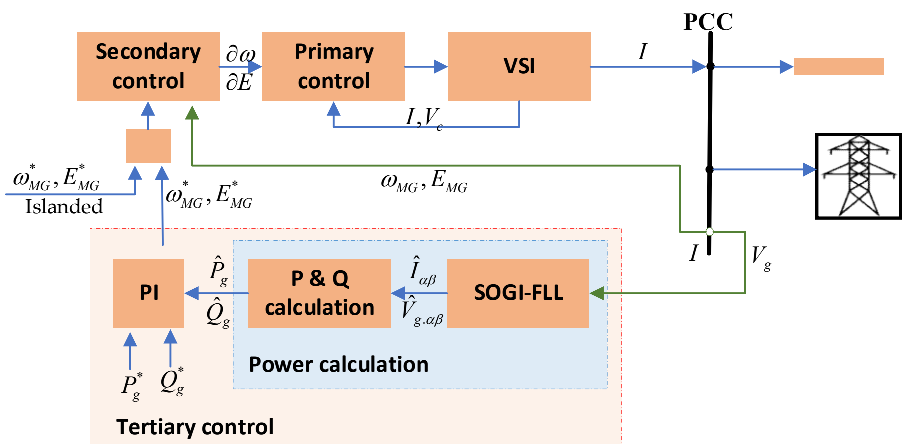

Fig.III. 7 Tertiary control diagram for a grid-tied MG

Fig.III.8 depicts a simplified block diagram of the power flow control between the grid and the DGs-based MG.

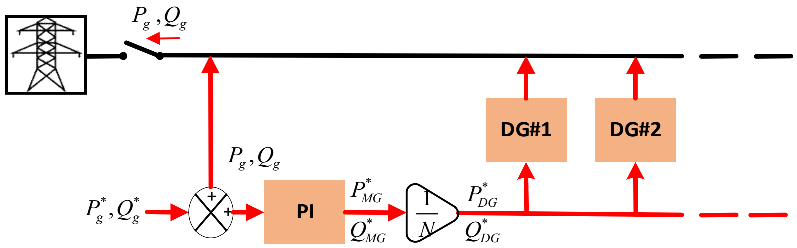

Fig.III. 8 Power flow control between the DG units and the utility grid diagram

The following expression can be used to acquire control over the flow of both active and reactive power [97]:

$$\begin{cases} \omega_{MG}^* = k_{p.P}(P_g^* - P_g) + k_{i.P}\int(P_g^* - P_g)dt \\ E_{MG}^* = k_{p.Q}(Q_g^* - Q_g) + k_{i.Q}\int(Q_g^* - Q_g)dt \end{cases} \quad \text{(III.22)}$$

Where the tertiary control compensator's control parameters are $k_{p.P}$, $k_{i.P}$, $k_{p.Q}$ and $k_{i.Q}$. The MG's references for active and reactive power are represented by the variables P_g and Q_g, respectively (*indicates the variable's reference value). The MG's nominal frequency and amplitude references are used when operating in island mode, and both active and reactive power are zero ($P_g^* = 0$, $Q_g^* = 0$). It's also critical to emphasize that, in accordance with the load power demand, the central manager is in charge of designating the appropriate grid power references to the DG units [151].

The characteristics of the tertiary control level are depicted in Fig.III.9, where the autonomous direction of outbound and inbound flows of active and reactive power depends on the sign of P_g^* and Q_g^*. Horizontal lines on the graph represent the frequency and amplitude (f_{MG} and E_{MG}) of the grid, which are held constant. As a result, the points at which the horizontal lines depicting the primary grid and the MG's droop characteristics intersect control the flow of active and reactive electricity between the two. As a result, the MG's frequency and amplitude references—referred to as f_{MG}^* and E_{MG}^*, respectively—can be adjusted to control power flows as follows:

- When $f_{MG} \langle f_g$, the MG generates P for the main grid, and the active power quantity $P_g \langle 0$.
- On the other hand, the MG absorbs P from the grid if $f_{MG} \rangle f_g$, which implies $P_g \rangle 0$.

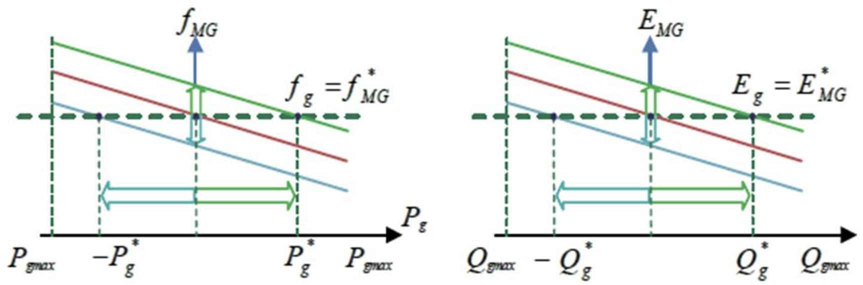

Fig.III. 9 Tertiary Control characteristics.

The grid affects the MG's frequency, which causes changes to the power angle. The reactive power Q_g can also be controlled using a similar method based on the amplitude reference of the MG, f^*_{MG}. Moreover, the tertiary control acts as the MG's primary control by setting $k_{i.P}$ and $k_{i.Q}$ to zero in the equation (III.22).

It is important to note that the MG is cut off from the grid and the tertiary control is turned off for safety reasons when the islanded mode happens.

In order to analyze the stability of the developed grid-connected MG system integrating tertiary control, and to appropriately determine the parameters of the tertiary controller, it is essential to establish a mathematical model. Therefore, the subsequent section introduces a precise modeling method utilizing dynamic phasors to derive the desired model.

III.6 Proposed Modeling approach for the power flow control

The objective of this section is to construct a precise small-signal model of a power flow control-oriented three-phase MG, employing the dynamic phasor principle. The formulated models enable the analysis and assessment of the dynamic characteristics of active and reactive power within the grid-connected distributed generation units, integrating the tertiary control system.

This section aims to build an accurate small-signal model using the dynamic phasor principle for a three-phase MG with power flow control. With the integration of the tertiary control system, the developed models provide the examination and evaluation of the dynamic properties of both active and reactive power in the grid-connected dispersed generation units.

It's crucial to mention that we have assumed there is no DC component in the input voltage in order to simplify the analysis. As a result, instead of using the dynamics of the DESOGI-FLL, the mathematical development uses those of the SOGI-FLL scheme.

III.6.1 Dynamic phasor modeling of the MG power flow

Dynamic phasors are being used more and more to simulate MGs that depend on power converters. For example, a technique based on dynamic phasors has been developed by researchers in [152-154] to generate realistic models of interfaced MGs with droop-controlled inverters. Nevertheless, these techniques usually presume that the low-pass filter's transfer function can adequately capture the dynamics of power computation. It is important to note that this is the underlying assumption of all existing modeling efforts for VSI-based MG systems. However, this first-order transfer function is not sufficient to reflect the nuances of power computation dynamics, especially for three-phase MGs. As a result, the generated models' small-signal analysis frequently falls short of correctly forecasting system instabilities.

By utilizing the dynamics of the SOGI-FLL, this study presents a dynamic phasor modeling approach for the grid-connected functioning of inverter-based MGs in order to address this problem. Fig.III.10 shows the suggested model for a three-phase grid-connected MG with tertiary control based on SOGI-FLL dynamics. The power flow model includes the tertiary control, the dynamics of the SOGI-FLL-based power computation, and line impedance that represents frequency and amplitude fluctuations of the MG, as illustrated in this diagram. It also includes models of the VSI circuit, primary control, and secondary control, all of which are considered to be unimportant. The ensuing subsections provide further detail on the mathematical examination of each part as well as the dynamic phasor modeling technique used to obtain the intended small-signal model of the entire system.

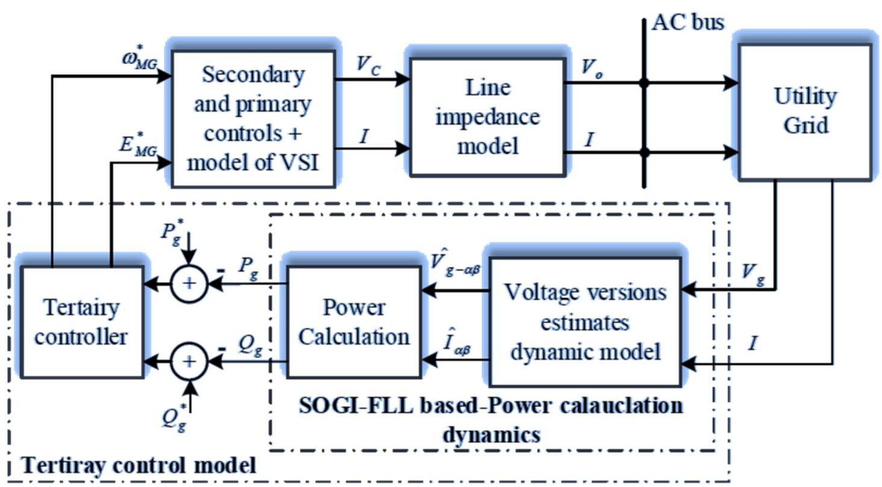

Fig.III. 10 Block diagram of a grid-tied VSI.

When operating in grid-tied mode, as shown in Fig.III.11, the AC MG is connected to the main utility grid by a tie line impedance at the PCC. A single DG unit is used to represent the MG in this arrangement. Assuming that switching ripples and high-frequency harmonics are ignored, the VSI is represented as an AC source with voltage $E(t)$. Furthermore, a voltage $V_g\angle 0$ is assumed for the utility AC grid.

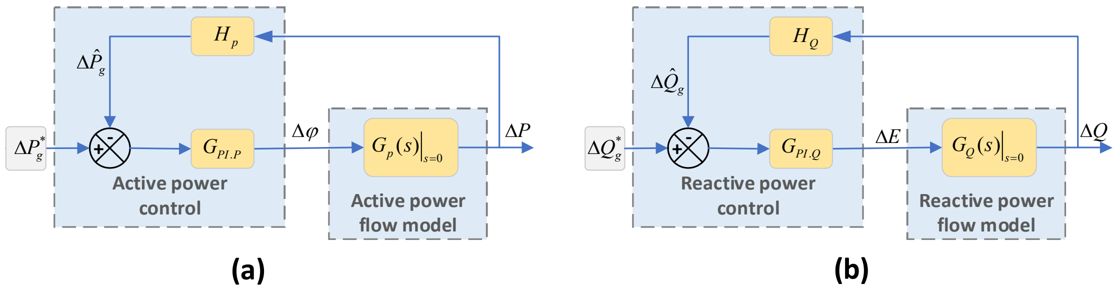

Fig.III. 11 Closed-loop small-signal model.

Power is moved between the main grid and the DG unit during this operating mode. The complex power, represented by S, that is transferred from the DG unit to the shared AC bus in the circuit shown in Fig. III.11 can be described as follows [143] :

$$S = V_g \times I^* = V_g\angle 0\left(\frac{V_g\angle 0 - E\angle\varphi}{Z\angle\delta}\right) = P + jQ \qquad \text{(III.23)}$$

where (*) is the complex conjugate operator.

The expression of the line impedance current must be ascertained before the mathematical formulation of the active and reactive powers can be derived.

III.6.2 Tertiary control parameter tuning

In this section, an effective tuning guideline for the proposed tertiary controller by using the obtained closed-loop model is investigated.

The approximate small-signal model shown in Fig. III.11 is used to determine the controller parameters ($k_{p.P}$, $k_{i.P}$, $k_{p.Q}$, and $k_{i.Q}$) associated with the desired response time (T_S), while constraining their fluctuations. This approach is required because of the complexity of conducting stability analyses using the resulting closed-loop model, wherein active and reactive powers are coupled. More specifically, there are significant difficulties when considering situations with broad fluctuations in all the above-mentioned parameters for both active and reactive controllers.

The power flow control's closed-loop small-signal model can be represented based on Fig. III.11, where the active and reactive powers are shown to be decoupled and the power stage dynamics are assumed to be unity:

$$\begin{cases} \Delta\hat{P}_g = \dfrac{G_P(s)\big|_{s=0} C_P(s) H_p(s)}{1+G_P(s)\big|_{s=0} C_P(s) H_p(s)} . \Delta P_g^* \\ \Delta\hat{Q}_g = \dfrac{G_Q(s)\big|_{s=0} C_Q(s) H_Q(s)}{1+G_Q(s)\big|_{s=0} C_Q(s) H_Q(s)} . \Delta Q_g^* \end{cases} \tag{III.24}$$

Accordingly, the characteristic equations of these transfer functions can be given by:

$$\begin{cases} s^2 + \underbrace{k\,{}^{\omega}\!/_{2}(1+G_P(s)\big|_{s=0} k_{p.P})}_{2\zeta_P\omega_{n.P}} s + \underbrace{G_P(s)\big|_{s=0} k_{i.P} k\,{}^{\omega}\!/_{2}}_{\omega_{n.P}^2} = 0 \\ s^2 + \underbrace{k\,{}^{\omega}\!/_{2}(1+G_Q(s)\big|_{s=0} k_{p.Q})}_{2\zeta_Q\omega_{n.Q}} s + \underbrace{G_Q(s)\big|_{s=0} k_{i.Q} k\,{}^{\omega}\!/_{2}}_{\omega_{n.Q}^2} = 0 \end{cases} \tag{III.25}$$

The parameters of the tertiary controller can be expressed as a function of the desired response time by matching these equations with the desired responses of a second-order characteristic equation and using the same tuning procedure previously suggested to determine the secondary controller parameters:

$$\begin{cases} k_{p.P} = \dfrac{4.82\dfrac{4\zeta_P}{k\omega T_{s.P}} - 1}{G_P(s)\big|_{s=0}} \\ k_{i.P} = \dfrac{2(4.82)^2}{G_P(s)\big|_{s=0} k\omega T_{s.P}^2} \end{cases} \qquad \begin{cases} k_{p.Q} = \dfrac{4.82\dfrac{4\zeta_Q}{k\omega T_{s.Q}} - 1}{G_Q(s)\big|_{s=0}} \\ k_{i.Q} = \dfrac{2(4.82)^2}{G_Q(s)\big|_{s=0} k\omega T_{s.Q}^2} \end{cases} \tag{III.26}$$

III.7 Simulation Results

This section presents the results of a simulation study conducted in the MATLAB/Sim Power System environment to evaluate the resilience and efficacy of the suggested secondary and tertiary control strategies.

Table III.1 reports the parameters used in the simulation study.

Table III. 1 Simulation parameters

Parameter	Symbol	Unit	Value
Inverter power stage			
Nominal voltage (RMS)	$E^*(RMS)$	V	220
Nominal frequency	$\omega^* / 2\pi$	Hz	50
DC bus voltage	V_{DC}	V	450
Loads	R_L, L_L	Ω, mH	40 , 1
Filter capacitor	C_1, C_2	μF	26

Filter inductor	r_1,L_1	Ω, mH	0.5 , 2.5
DG1 line impedance	L_i	mH	0.9
Grid impedance	L_g,r_g	mH , Ω	0.1 , 0.001
SOGI-FLL scheme			
SOGI gain	k	-	0.7
FLL gain	Γ	s^{-1}	40
Primary control			
Frequency-droop gain	m	$W / rad.s$	0.0003
Amplitude-droop gain	n	VAR / V	0.003
Virtual impedance	L_v	mH	4
Secondary control			
Voltage proportional gain	$k_{p.E}$	-	-0.45
Voltage integral gain	$k_{i.E}$	s^{-1}	1.57
Frequency proportional gain	$k_{p.f}$	-	-0.22
Frequency integral gain	$k_{i.f}$	s^{-1}	2.67
Synchronization gain	$k_{p.\varphi}$	s^{-1}	0.76
Communication time delay	τ	ms	0.5
Power flow control			
P proportional gain	$k_{p.P}$	-	0.0003
P integral gain	$k_{i.P}$	s^{-1}	0.003
Q proportional gain	$k_{p.Q}$	-	4
Q integral gain	$k_{i.Q}$	s^{-1}	0.76

III.7.1 Secondary

In the first step, the framework of an islanded MG system test is constructed, as shown in Fig.III.2. A local load is fed by two DG units with the same power rate. The control in this subsection consists of the primary and secondary levels.

The following case studies are taken into account, with two cases testing the restoration control, and the final case examining synchronization. Note that the first operation scenario is considered for all the tests, where the MG starts at t=0 s with the no-load operating condition, and at t = 0.1 s, DG units begin feeding a common load while only the primary control is working. The frequency and amplitude restoration control are turned on at t = 0.5 s. After this scenario, the next scenarios for the VSI-based MG are carried out according to the considered tests presented as follows:

Case 01: Load variations

A load is disconnected and reconnected from and to the MG at t = 1 s and t = 1.5 s, respectively, to make a load variation.

Case 02: DG disconnection
In order to achieve this, DG#2 is disconnected from the MG at t = 1 s. This leaves DG #1 to supply the common load, and reconnect at t=1.5 s.

Case 03: The synchronization examination
Thus, this controller is turned on at t = 1 s to synchronize the MG with the main utility grid (50 Hz and 220V),

The transient responses of DG units, and the MG at the PCC for the first case study are displayed in Fig.III.12. These responses include active and reactive powers, frequency, and amplitude. It is evident that the PCC and each DG unit are running at their nominal values when there is no load. Then when the primary control is operating, they drop with the same amounts to split the load's active and reactive powers when a load is attached.

The droop control's frequency and amplitude static deviations are eliminated when the restoration procedure is activated at t = 0.5 s, meaning that the MG's frequency and voltage smoothly return to their nominal values of 50 Hz and 311V. Furthermore, as demonstrated, the suggested secondary controller maintains the specified active and reactive powers-sharing while guaranteeing a smooth frequency and voltage recovery in the event of an abrupt load change (at t = 1 s and 1.5 s). We see that, with a settling time of around 1/4 s and without overshoots, the suggested controller offers good transient responses with regard to the intended specified performance.

Fig.III.13 provides the acquired findings for case 02, showing how the intended controllers successfully restore the frequency and amplitude of the MG, which is only created by DG#01, to their nominal values when the DG#02 is separated from the MG at t = 1 s. It should be noted that the frequency and voltage transient responses have a settling time of roughly 1/4 s and have no overshoots.

Results for case 03 are obtained and are shown in Fig. III.14. The MG frequency matches the main utility grid’s frequency zero when the synchronization procedure is enabled at t = 1 s. Additionally, the grid set points determine the frequency and amplitude of the PCC and DG units. while the synchronization procedure is activated, the active power stays constant. It is observed that the synchronization process is made in a short settling time.

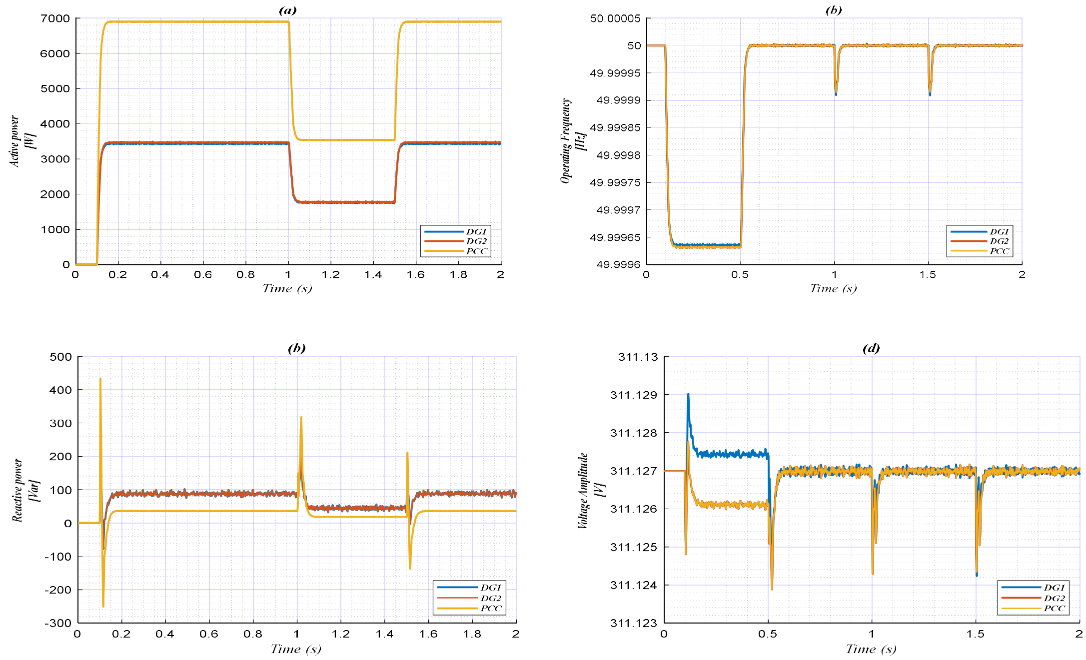

Fig.III. 12 obtained results for case 01

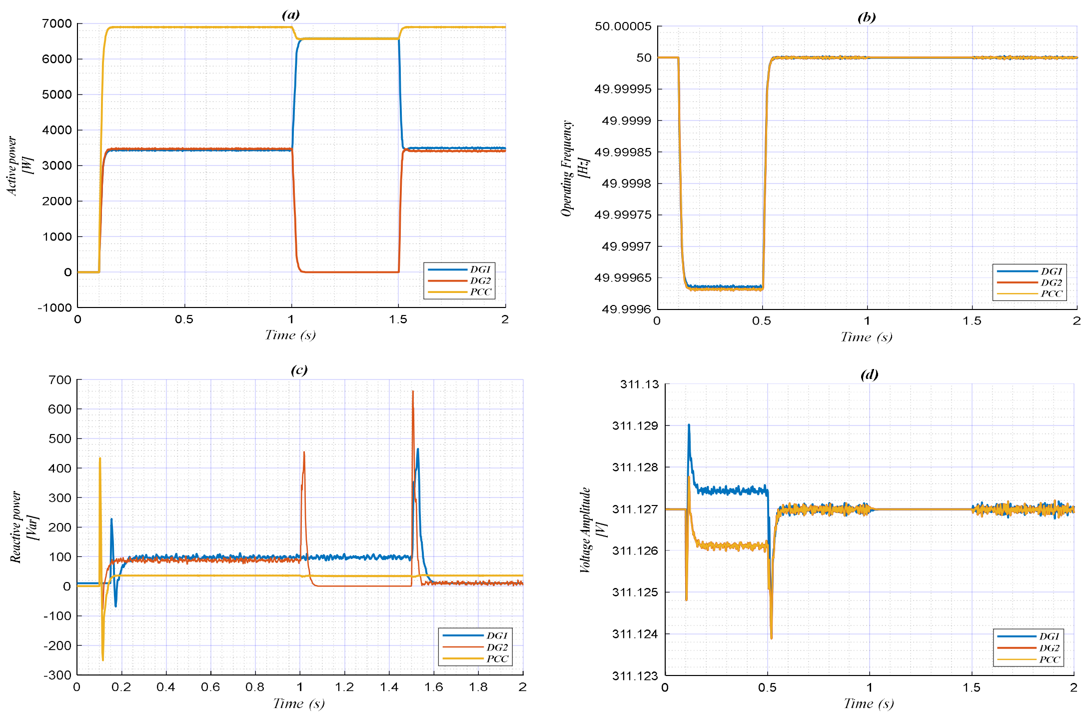

Fig.III. 13 obtained results for case 02

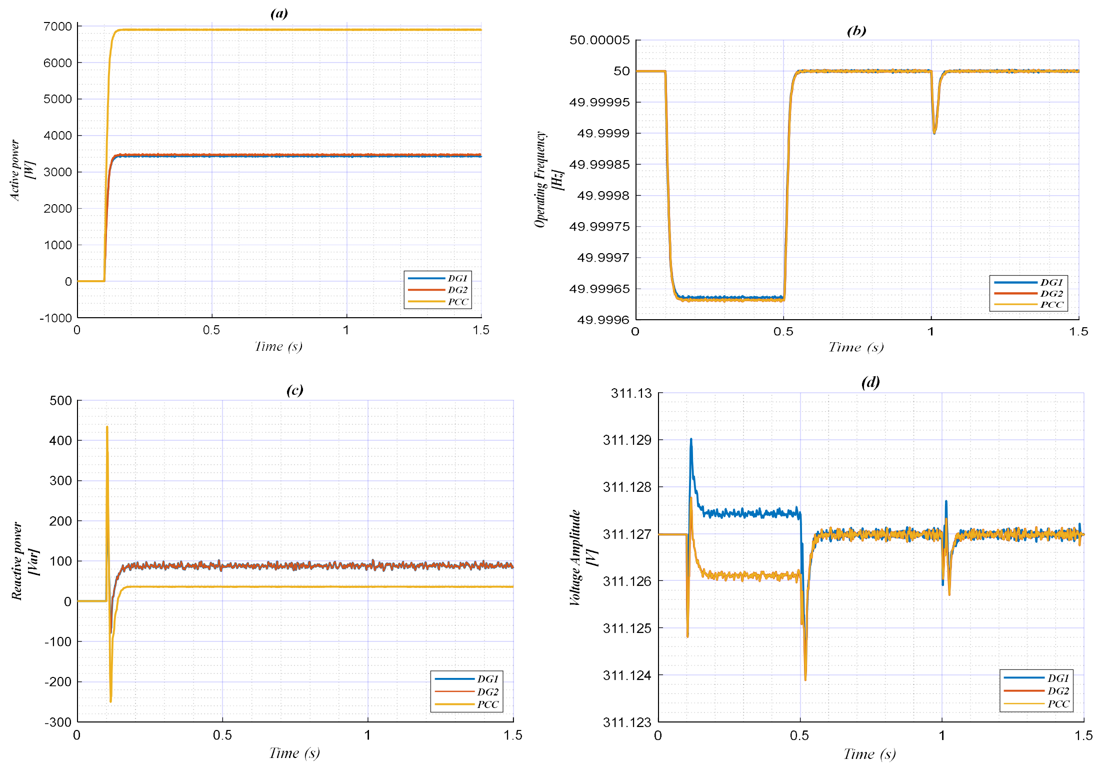

Fig.III. 14 obtained results for case 03

III.8 Conclusion

This chapter discussed two main contributions of the present thesis. Firstly, an innovative approach is proposed for developing a scheme and getting precise models for the secondary control of a three-phase MG using the DESOGI-FLL system. Design analysis and modeling of both restoration and synchronization control loops within the secondary control layer were performed. Then, the tertiary control for the power flow of three-phase grid-connected VSIs that are used as grid-forming units toward the main grid is described. Where, a modeling approach based on the dynamic phasor idea is utilized to accurately represent the flow of active and reactive power between the grid and the MG. Overall, the efficacy of the suggested secondary and tertiary control schemes has been successfully validated through simulations using MATLAB/Simulink and tests employing three-phase parallel-connected VSIs. They have shown how well the controller works to provide a system that can adapt to variations in distributed generation output and load demand while maintaining optimal power flow.

The next chapter, will involve an application of a three-phase PV MG, using the hierarchical control levels studied in the last two chapters.

Chapter IV: Improved Photovoltaic Microgrid System

IV.1 Introduction

In solar PV conversion, solar energy is converted into electricity through PV panels. These serve as a voltage generator to power a load. But the problem here is that the voltage supplied by these PVGs remains lower, that is why an adaptation stage (regulation) is required. This converter is used to adapt the energy drawn from the sun to suit the load and meet all the desired requirements. In itself, needs a switching controller.

To regulate the overall output power to the load, the PVGs must be able to communicate with each other.

The preceding chapters have given an overview of the study's scope and conducted a comprehensive analysis of the hierarchical control approach adopted for this research project. This chapter focuses on modeling a PV MG while considering the hierarchical control method. It begins by introducing the structure of the PVG and discussing the most commonly used analytical model for PVGs in section 2. Following that, section 3 delves into the DC-DC boost power converter and elucidates its operational principles. Moving forward to section 4, the MPPT controller is briefly elaborated, with emphasis on the P&O method. Finally, section 5 presents the simulation results and discussions pertaining to the entire PV system, encompassing two PVGs controlled by an MPPT-controlled boost converter, interconnected to the PCC through a three-phase voltage source inverter (VSI) based on hierarchical control.

IV.2 Power Source: Photovoltaic Solar Generator

IV.2.1 Generalities

The term «Photovoltaic» is a Latin word, «photon» means light and «volta» in reference to the Italian physicist (Alessandro VOLTA) who gives his name to the unit of measurement of the electric voltage [16].

Unlike passive solar energy, which uses the structural elements of a building to heat/cool it, and active solar energy, which uses a heat carrier (liquid or gaseous) to transport and store heat from the sun (water heater), photovoltaic energy is not a form of thermal energy [18], but rather is the direct conversion of light into electricity via a solar cell.

The PV effect was discovered in 1839 by the French physicist ALEXADRE EDMOND BECQUEREL who demonstrated that it was a direct conversion of light into electrical energy. However, at that time, there was no practical use of this discovery. In 1905, Albert EINSTEIN wrote that light can enter inside atoms and that the collision between photons and atoms can bring electrons out of their orbits and thus allow the creation of an electric current. It was not until the 1950s that researchers at Bell Telephone in the United States were able to manufacture the first silicon-based cell, the primary element of a PV system [5] [16] [18].

The solar cell is the basic element of a PVG and PV conversion in general. It is comparable to a photosensitive diode [20]. It is an optoelectronic component made from semiconductor materials, most often, silicon because it is the most common material on earth. It is found in nature in the form of silica stone (it is sand roughly), but has a high degree of purity.

A PV cell consists of two thin layers of semiconductor doped differently (one is doped in P generally with boron and the other in N generally with phosphorus) thus creating a PN junction. The N layer has a surplus of electrons (charge-), and the P layer has an electron deficit (charge+). When a photon of light, of sufficient energy, hits an atom on the negative part of this cell (the N layer), it excites an electron and pulls it out of its molecular structure, thus creating a free electron (-) and a hole (+), when the electron-pair hole is created, negative charges will be separated from positive charges (the free electron moves to the N side while the hole migrates to the P side). A potential difference is therefore created (varying between 0.3 V and 0.7 V depending on the material used, its layout as well as the temperature of the cell and its aging rate [21]) between the two layers and a current is manifested inside the crystalline matter if a resistance (bulb for example) is placed between its contacts.

Fig. IV.1 gives the structure, as well as the working principle of a PV cell.

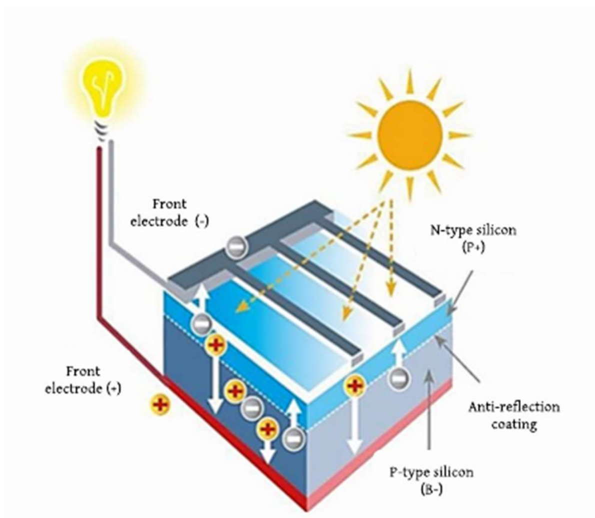

Fig.IV. 1 PV cell functional principal

The efficiency of a PV cell depends considerably on its structure and composition. A lot of research has focused on this area, and this is how we have developed, in a very diverse way, PV cell technologies. We find that the actual yield of PV cells decreases compared to theoretical calculations and obtained in the laboratory, which explains the influence of the weather conditions that we will discuss later. The electrical power produced by an industrialized cell is very low with a voltage of less than one volt (0.6 to 0.7 V) and a more or less low current. To raise the voltage/current, the cells are marketed as PV modules.

A PV solar generator is a system that converts solar radiation into electricity. It is generally composed of a PV panel array producing direct current, arranged in multiple series-connected strings of panels, which can be further interconnected in a parallel configuration. In addition to a converter optimizing the operating point of the generator and converting the electrical voltage to the desired level.

A GPV is used to produce and generate electrical energy from sunlight (solar radiation, insolation). Typically, a GPV consists of PV cells. PV devices are available as sets of PV cells connected in series and/or in parallel combined into a single waterproof element (protection against moisture, shock and other nuisances), commonly called PV modules.

The serial connection of several PV modules constitutes a PV chain. It should be mentioned that the number of PV modules connected in series in the same PV chain is related to the voltage required at the output [26].

Finally, a PV array is formed of two or more PV chains connected in parallel, in order to generate the required power.

The attached Fig.IV.2 illustrates the GPV structure.

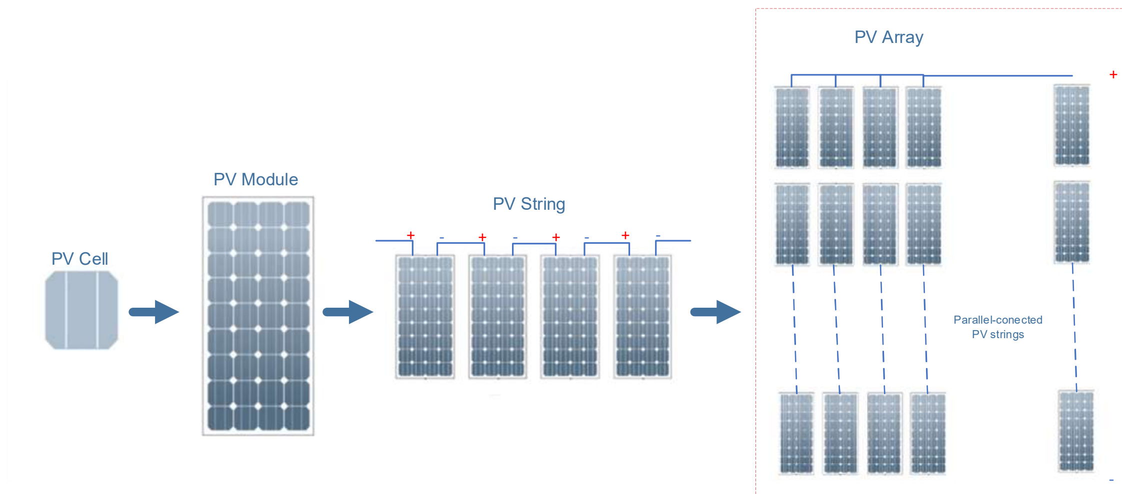

Fig.IV. 2 Structure of a PVG

IV.2.2 Equivalent circuit of a solar cell

A PV cell can be represented by the equivalent electrical circuit shown in Fig. IV.3. According to this model, it consists of a diode that represents the PN junction of the cell connected in parallel to a current source whose current amplitude depends on the radiation intensity [24], In addition, since a PV cell is not perfect in real life, the model must include both, series (R_s) and shunt (R_{sh}) resistors.

In fact, the shunt resistor R_{sh} characterizes the leakage current on the cell surface due to the non-ideality of the PN junction and impurities near the junction, while the R_s represents the different contact resistances and semiconductor resistance. Usually, R_s is very small while R_{sh}

is very high [25]. These resistors will have some influence on the I-V (current-voltage) characteristic of the cell.

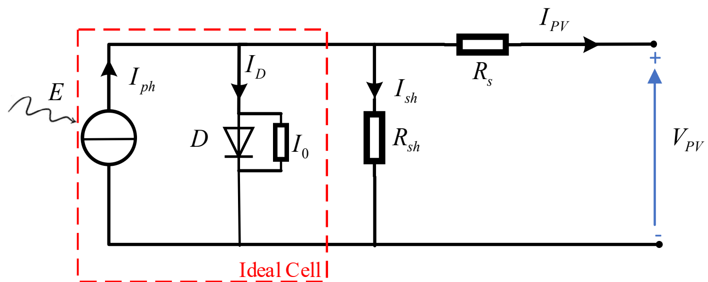

Fig. IV. 3 Equivalent circuit of a solar cell

IV.2.3 Characteristic equations

Based on this equivalent circuit, the PV cell is seen as a current source with the PV effect. The output current can be expressed as follows:

$$I_{PV} = I_{ph} - I_D - I_{sh} \qquad \text{(IV.1)}$$

Where:

I_{PV} : PV cell's output current [A]

I_{ph} : Photo-current which is proportional to the intensity of irradiation G [A]

I_D: Diode current [A] given by the following equation:

$$I_D = I_s\left(\exp\left(\frac{V_{PV} + R_s I_{PV}}{V_t}\right) - 1\right) \qquad \text{(IV.2)}$$

V_{PV} : output voltage of the PV cells [V]

V_t : thermal voltage of the diode such as $V_t = \dfrac{nkT}{q}$

I_s : Saturation current [A]

q : Elementary charge [1.6022×10^{-19} C]

n: Diode ideality factor ($1 \langle N \langle 3$; 1 for an ideal diode)

k : Boltzmann's constant [1.3806×10^{-23} J / K]

T : cell temperature [K]

I_{sh} : Shunt current [A]

$$I_{sh} = \frac{V_{PV} + R_s I_{PV}}{R_{sh}} = \frac{V_{sh}}{R_{sh}} \qquad \text{(IV.3)}$$

Hence, the voltage across these elements is:

$$V_{sh} = V_{PV} + R_s I_{PV} \qquad \text{(IV.4)}$$

Where:

V_{sh}: voltage applied to the resistor R_{sh} and diode D [V]

R_s: Series resistor [Ω]

From these equations, the characteristic equation of a PV cell, that relates PV cell parameters to the output current and voltage can be expressed as:

$$I_{PV} = I_{ph} - I_s\left(\exp\left(\frac{(V_{PV} + R_s I_{PV})}{V_t}\right) - 1\right) - \frac{V_{PV} + R_s I_{PV}}{R_{sh}} \qquad \text{(IV.5)}$$

Since Equation (IV.5) includes the output current I_{PV} on both sides, it has no general analytical solution. Hence, I_{PV} can be determined for a given voltage V_{PV}.

It should be noted that the current I_{PV} is defined as the short-circuit current (I_{sc}) when $V_{PV} = 0$ (short-circuit operating). This is the highest current value generated by the cell. Then, for a low R_s and I_s, and a high R_{sh} values, it can be expressed by:

$$I_{sc} = I_{ph} \qquad \text{(IV.6)}$$

Knowing that the photocurrent I_{ph} varies with irradiance and temperature, equation (IV.6) becomes:

$$I_{sc} = I_{ph} = \left[I_s + k\left(T - T_0\right)\right]\frac{G}{G_0} \qquad \text{(IV.7)}$$

Where:

I_s: the saturation current of the diode, is assumed to vary with temperature according to the expression:

$$I_s = I_{rs}\left(\frac{T}{T_0}\right)^3 \exp\left[\frac{E_{g0}\left({}^1\!/_{T_0} - {}^1\!/_T\right)}{V_t}\right] \qquad \text{(IV.8)}$$

Where, I_{rs} is the reverse saturation current given by:

$$I_{rs} = \frac{I_{sc}}{\exp\left(\frac{V_{oc}}{V_t}\right) - 1} \qquad \text{(IV.9)}$$

On the other hand, the voltage V_{PV} is defined as the open circuit voltage V_{oc} when $I_{PV} = 0$ (open circuit operating), it is the maximum voltage of a solar cell or PV generator, expressed as:

$$V_{oc} = V_t \ln\left(\frac{I_{ph}}{I_o}\right) \qquad \text{(IV.10)}$$

At the open-circuit condition ($V_{PV} = V_{oc}$ and $I_{PV} = 0$), the equation (IV.6) becomes:

$$I_{ph} = I_D + I_{sh} = I_s\left(\exp\left(\frac{V_{oc}}{V_t}\right) - 1\right) + \frac{V_{oc}}{R_{sh}} \qquad \text{(IV.11)}$$

Notes:

• The temperature affects both the ideality factor and the resistors. The model is simplified by setting these variables, as well as I_{sc} and V_{oc} at STC (STC: Standard Test Conditions, $G_0 = 1000 W/m^2$ and $T_0 = 25°C$ and $AM_{1.5}$ spectrum).

• The nominal power of the PV cells depends strongly on the surface of the cell and the technology of the PV cells.

• Based on the model of the PV cell given by Equation (IV.5), the mathematical model of the output current of a PVG composed of several PV cells connected in series and in parallel will therefore be given by :

$$I_{GPV} = N_p\left[I_{ph} - I_s\left(\exp\left(\frac{V_{PV} + R_s I_{PV}}{V_t N_s}\right) - 1\right) - \frac{V_{PV} + R_s I_{PV}}{R_{sh} N_s}\right] \qquad \text{(IV.12)}$$

With N_s and N_p are the number of series and parallel connected PV cells, respectively.

IV.2.4 PV module Characteristics

Fig. IV.4 shows the current-voltage (I-V) and power-voltage (P-V) characteristics of a PV cell at a fixed temperature (25°C) and a certain irradiation environment (1000W/m²).

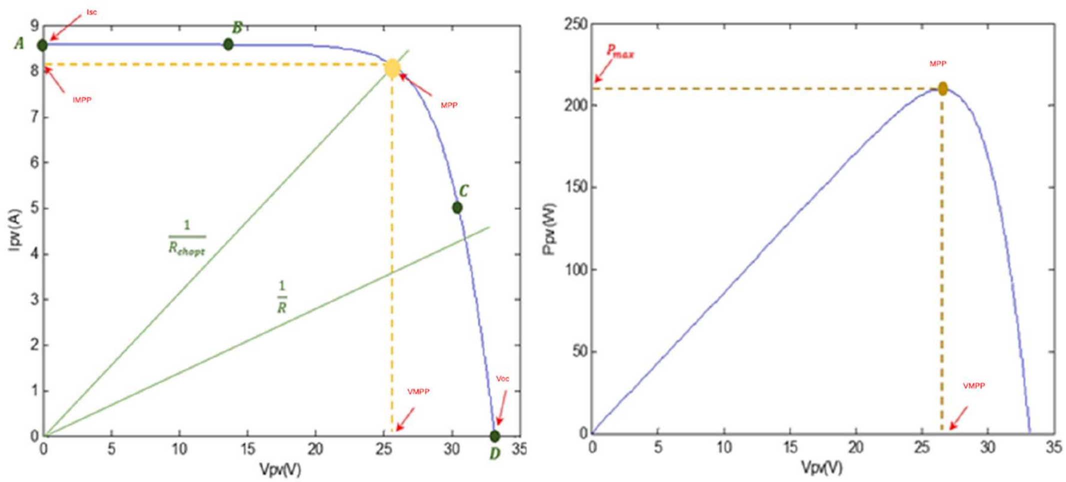

Fig.IV. 4 PV characteristics (a) current-voltage (I-V) (b) power-voltage (P-V)

The results obtained, confirm that actually, the characteristic I-V of the module are non-linear, and that there is a Maximum Power Point (MPP) in which the module operates at its maximum power. This is the maximum electrical power that the module can provide, which is associated with a maximum voltage V_{MPP} and a maximum current I_{MPP}. When it comes to maximum power under STC (25° and 1000 w/m²), we then speak of peak power, measured in watts-peak (W_c).

If a variable serial resistor (R_{chopt}) is connected to the terminal of the module, the point of operation is determined by the intersection of the current-voltage curve and the current-voltage characteristics of the load.

The characteristic of the resistive load is a line with a slope I/V= 1/R_chopt ;

If the resistance is small, the PVG operates in the region A to B only (as a constant current source), and if the resistance is large, it operates in the region C to D of the curve (as a constant voltage source) [29], it can therefore be said that the impedance of the load dictates the operating condition of the PV module.

The PVG is also characterized by two main parameters, the fill factor (FF) and the conversion yield (η). The FF is the ratio of the maximum power that can be delivered to the load on the product of I_{sc} and V_{oc}:

$$FF = \frac{P_{\max}}{I_{sc}V_{oc}} = \frac{\mathrm{I}_{MPP}V_{MPP}}{I_{sc}V_{oc}} \qquad \text{(IV.13)}$$

For cells with medium efficiency, the FF takes values of order 0.7 to 0.85. It decreases if the temperature increases.

While η is the ratio of the maximum electrical power that can be extracted, to the incident radiation power (P_{inc}) on the surface of the cell. It reflects the conversion quality of solar energy into electrical energy.

$$\eta = \frac{P_{\max}}{P_{inc}} = \frac{I_{MPP}V_{MPP}}{S \times G} = \frac{I_{sc}V_{oc}FF}{P_{inc}} \qquad \text{(IV.14)}$$

Irradiation and temperature are the most important parameters affecting the behavior of the module. Figs.IV.5 (a) and (b) illustrate respectively the I-V and P-V characteristics of the simulated module at a temperature of 25°C at different levels of irradiance (ranging from 200W/m² to 1000 W/m² with a move of 200 W/m²), while Figs.IV.6 (a) and (b) depict the I-V and P-V characteristics of the same module under an irradiance of 1000 W/m² at different temperatures (ranging from -25°C to 75°C with a move of 25°C).

It can be seen that the large variations in the level of solar irradiance cause relatively large variations in the optimal current, unlike the voltage, which varies very little (Fig.IV.5 (b)), consequently, the variation of the MPP is proportional to the variation in solar irradiance (Fig.IV.6(b)). This implies that the MPPs are about the same voltage.

Furthermore, the current of the short circuit I_{sc} remains very insensitive to the variation of the temperature but the voltage of the open circuit V_{oc} decreases by increasing the temperature which causes a decrease of the power at the output of the module. Therefore, it can be noted that the influence of temperature is not negligible on the characteristic of a PVG, so a lower temperature level gives a greater open circuit voltage (V_{oc}) and a higher output power and vice versa.

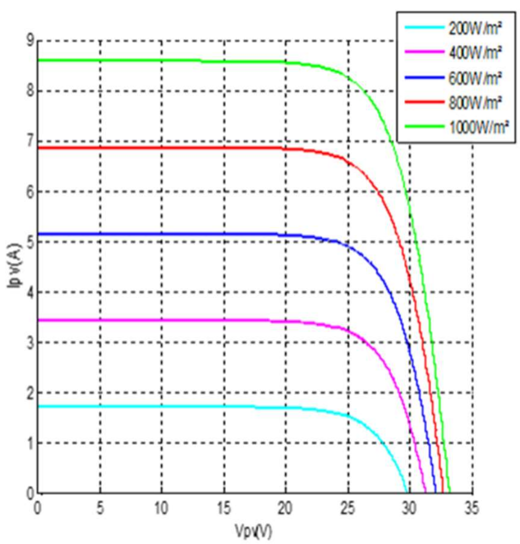

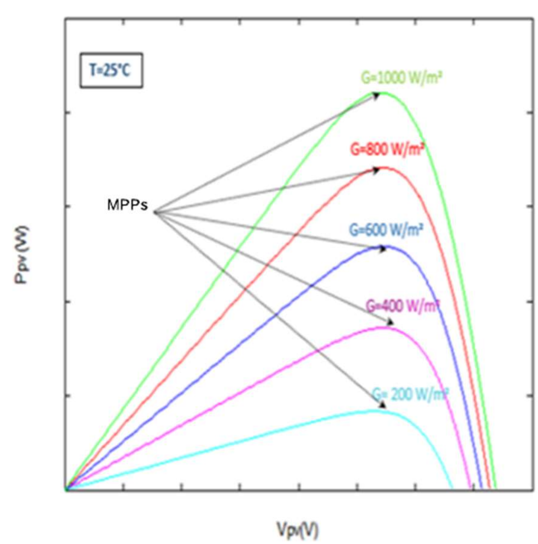

Fig.IV. 5 PV characteristics under temperature variation (a) I-V (b) P-V

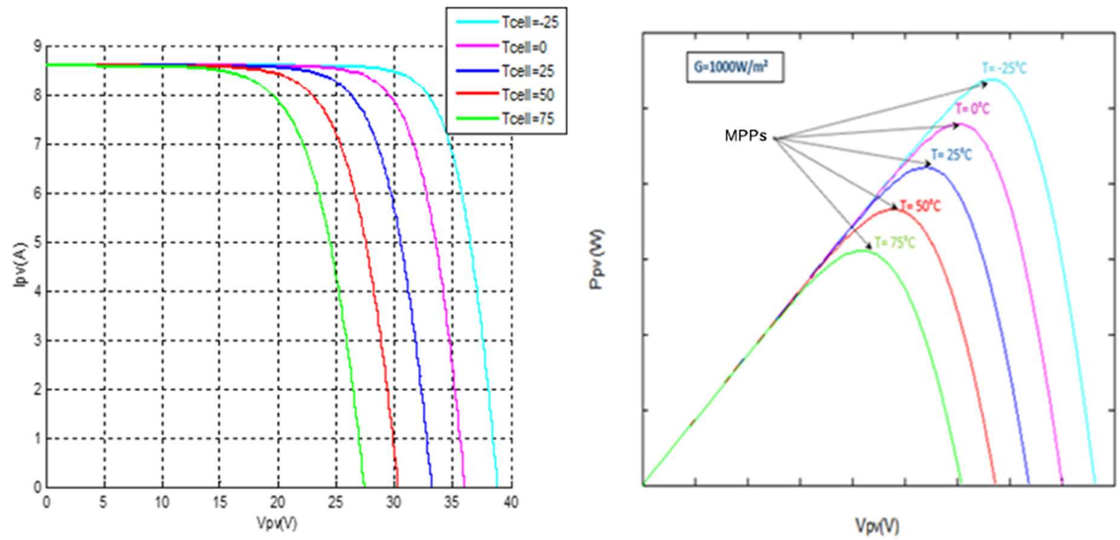

Fig.IV. 6 PV characteristics under irradiation variation (a) I-V (b) P-V

IV.3 Power Converter: Adaptation Stage

A DC-DC converter, also called a chopper, is an electrical circuit that serves as an interface between two stages in order to transform, not the nature of the quantities since they always remain continuous, but rather their values. While trying to save at best, the total transfer of energy is something that is obtained only with a high conversion efficiency [30].

In the context of PV, a DC/DC converter has a dual function: on the one hand, it is used to adapt the form of energy to the needs of a load, typically by providing a continuous voltage of adjustable average value from a fixed DC voltage source. On the other hand, it is in charge of stabilizing this flow of energy by filtering as much as possible the fluctuations of the source [31].

The DC/DC converter can increase or decrease the voltage of the PV system according to the load requirements [32]. If the voltage delivered at the output is lower than the voltage applied at the input, the chopper is said to be the Buck converter, otherwise, that is, if the voltage at the output is higher than at the input, the chopper is said to be the boost converter. There are also choppers that are both buck and boost called Buck-Boost.

IV.3.1 Generalities

The PVG provides a low voltage that we have to adapt to the rated voltage of the load. In addition, it is essential that the efficiency is maintained high to avoid power dissipation and to avoid excessive heating in electronic components. From a control perspective, the Boost converter is the most suitable for this type of conversion, so a thorough investigation of this converter is needed.

A DC/DC converter consists essentially of at least two semiconductors: a K switch and a D diode and at least one energy storage element: a C capacitor or an L inductance or both in combination. Capacitor filters are added to the converter output to reduce the ripple of the output voltage [32]. Depending on the position of the switch and the diode, different types of voltage converters can be made.

As its name indicates, the DC-DC boost converter boosts the voltage to a higher level, at steady state operation, the output voltage V_{out} is always higher than the input voltage V_{in}. As shown in its basic form in Fig.IV.7 the circuit of this converter is composed of an inductor (L), a diode (D) in series, a filter capacitor (C), used to stabilize the output voltage and an $IGBT$ or a $MOSFET$ power switch (S) in parallel.

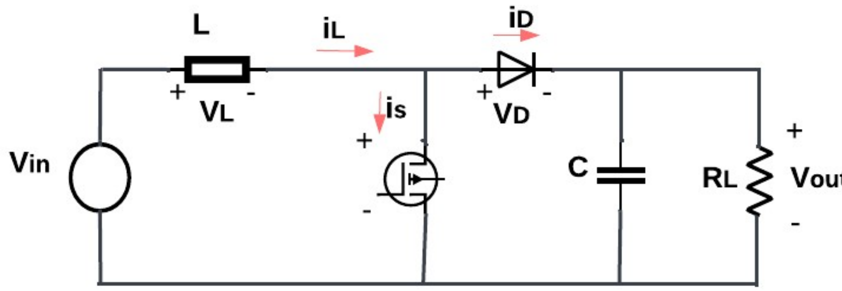

Fig.IV. 7 Electrical circuit of a boost DC/DC converter.

IV.3.2 Operation principle

In the application of power electronics, the principle of operation of a chopper is based on the use of switches in order to vary the operation of an electric circuit over a given period, in order to achieve a desired operation [30].

The converter is characterized by a switching frequency $f_s = 1/T_s$, at which the switch S is turned ON and OFF, and a duty ratio $\alpha = T_{ON}/T_s$, which is the time when the switch S is ON. S is controlled by a PWM signal of fixed switching period T_s and variable duty cycle α. The conduction of the two switches is complimentary, when S is closed D is open; and when S is open, D is closed. During each period, S is closed from moment 0 to αT_s and opened from αT_s to T_s [31].

Fig.IV.8. depicts the boost's operation principal based on the idealized waveforms of the currents (left) and voltages(right) while respecting the following assumptions:

- The switching elements (MOSFET and diode) of the converter are ideal in order to avoid the use of complex mathematics.
- The transistor and the diode output capacitance, the load inductances and switching losses are neglected.
- The passive components of the converter (R , L , C) are frequency independent, linear, and time-invariant.
- The current never cancels in the inductor.
- For both DC and AC components, the input voltage source's output impedance is zero.

- In the first period $\left[0-\alpha T_s\right]$ S is ON, the diode is reverse biased $V_D=-V_{out}$, while the voltage through the inductor is $V_L=V_{in}$, hence, the current increases linearly with a slope of V_{in}/V_{out}, leading to an increase in the magnetic energy. The switch and inductor currents are equal. At the time $t=\alpha T_s$, the current in the inductance reaches its maximum value $I_{\max}$.
- In the second period $\left[\alpha T_s-T_s\right]$ the switch opens, the inductor behaves as a current source and triggers the diode to turn ON. The voltage through the inductor becomes $V_L=V_{in}-V_{out}$. Hence, the inductor current decreases with a slope of $V_{in}-V_{out}/L$. The diode current matches the inductor current, and the energy is sent to the filter capacitor C and the load resistance RL from the inductor L.
- The switch is turned on once again at a time $t=T_s$, completing the cycle.

<u>Notes:</u>

The average value of the output voltage V_{out}:

$$V_{out}=\frac{1}{1-\alpha}V_{in} \qquad \text{(IV.15)}$$

The gain is as follows:

$$\frac{V_{out}}{V_{in}}=\frac{1}{1-\alpha} \qquad \text{(IV.16)}$$

The cyclic ratio α being between 0 and 1, the gain in tension is much higher than or equal to 1 which justifies the name Boost converter.

The output voltage of the converter can be controlled by varying its input voltage or cyclic ratio.

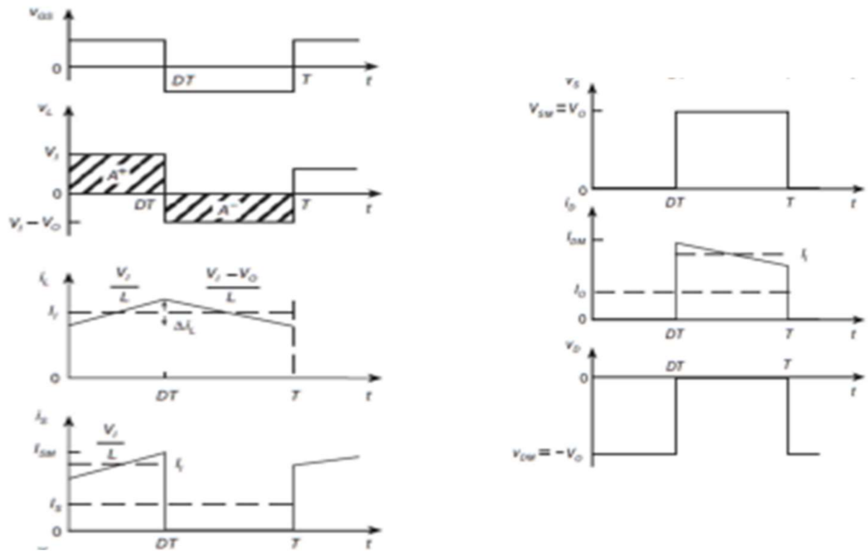

Fig.IV. 8 Ideal current and voltage waveform in PWM boost converter.

The boost converter faces risks from voltage surges, especially during the initial turn-on and when the output voltage is lower than the input. To address this, adding a diode between the input and output helps by creating a peak rectifier function. This diode allows energy flow from input to output when needed and prevents damage to the converter.

In the PV power conversion system, PV panels are regarded as a current source (I_{PV}). They supply a voltage source (V_{PV}), which serves as the DC-DC boost converter's input. The converter is represented as a current source $i_{L.PV}$ which is determined by the modulated voltage V_{PVm}, and the PV voltage.

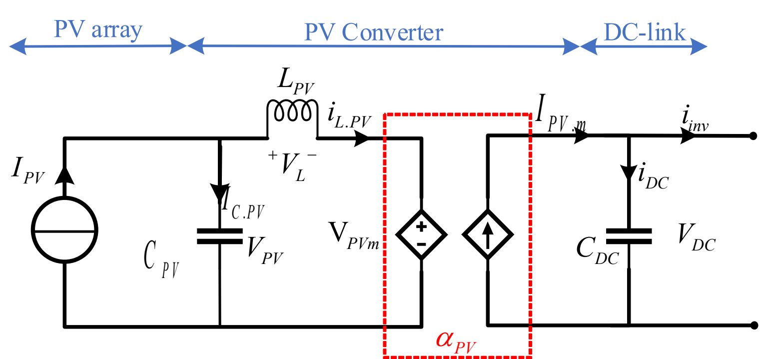

Fig.IV. 9 Equivalent electrical diagram of PV power conversion system

$$\frac{d}{dt} i_{L.PV} = \frac{1}{L_{PV}} \left(V_{PV} - V_{PVm} \right) \qquad \text{(IV.17)}$$

The capacitor and filter losses are not considered. The PV panels' voltage V_{PV} can be stabilized using the capacitor C_{PV}. The PV current (i_{PV}) and the filtered current ($i_{L.PV}$) can be used to model this capacitor:

$$\begin{cases} \frac{d}{dt}\mathrm{V}_{PV} = \frac{1}{C_{PV}} i_{C.PV} \\ i_{C.PV} = i_{PV} - i_{L.PV} \end{cases} \qquad \text{(IV.18)}$$

$i_{C.PV}$ denotes the capacitor injected current. The duty cycle ratio (α_{PV}) and the DC-link voltage (V_{DC}) are used to calculate the voltage V_{PVm} of the converter terminals as follows:

$$\begin{cases} \mathrm{V}_{PVm} = \alpha_{PV} V_{DC} \\ i_{PVm} = \alpha_{PV} i_{L.PV} \end{cases} \qquad \text{(IV.19)}$$

IV.4 MPPT Based on Voltage or Current Control (VMPPT and CMPPT)

IV.4.1 Generalities

Each PV module is characterized by a non-linear curve that depends strongly on external conditions (level of irradiation, temperature of the cells, shading, nature of the load fed, etc.), and as we have seen, these curves present, under uniform conditions, a single peak named the MPP, at which the module operates with maximum efficiency.

Because, the MPP position depends on the level of irradiation and the temperature of the cells, it is never constant over time. The possible solution to deal with this, is to use a tracking command. The latter aims to monitor these changes and ensure that the power supplied by the generator is as close as possible to the maximum power available or a specific power value for any operating conditions (radiation, temperature, load characteristics). This can be achieved by combining an MPPT controller with the electronic power converter.

An MPPT controller is used to adjust and achieve the proper duty cycle of the PWM DC-DC converter. This technique was first used in the 1970s for aerospace applications by the company «Honeywell» and the research center «NASA»[26]. And since then, great work has been done to improve the performance of PV systems through the development of new MPPTs or existing upgrades, their algorithms can be more or less complex depending on the type of implementation chosen and the performance sought. Several algorithms are present in the literature, they differ among themselves by their complexity, the number of sensors required, the speed of convergence, cost, and efficiency [39]. In practice, within PV systems, contrary to the irradiation, the ambient temperature doesn't fluctuate abruptly, so the voltage doesn't too, as a result. A basic P&O method; which is one of the most widely used methods due to the simplicity of its reasoning and ease of implementation [1]; is sufficient for the need of this research work.

Fig.IV.10 shows the schema of the implementation of an MPPT command in a PV conversion system. This command is done automatically to adapt to variable weather conditions, and varies the cyclic ratio of the DC-DC converter according to the evolution of its input parameters (I_{PV} and V_{PV} and consequently the power of the PVG) so that the power supplied is the maximum (P_{MPP}) available at its output [36].

This is a real-time pursuit. The position of the MPP varies in most of the time, it happens more or less quickly depending on the operating conditions.

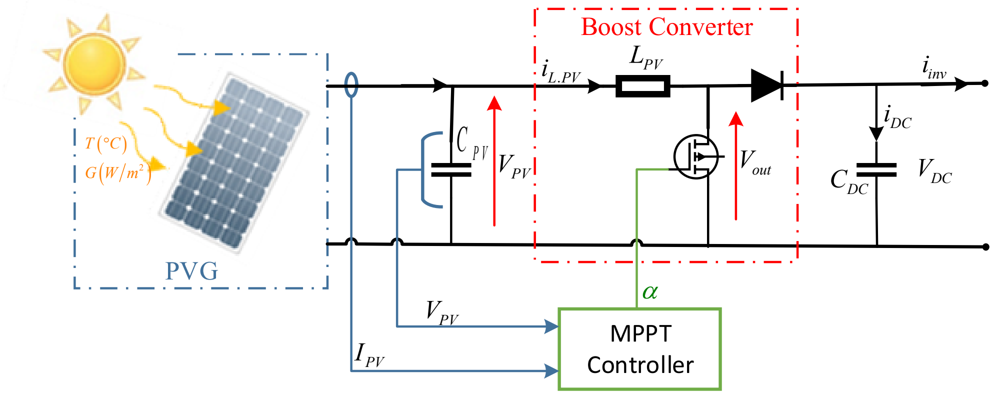

Fig.IV. 10 Controlled PV system.

During the operation of the PVG, several disturbances can modify the MPP. Fig.IV.11 illustrates a case of disturbances and shows the behavior of the PVG against them.

Suppose a PVG operates under a C_1 condition with a single MPP_1. The PV system, in case the pursuit is assured, manages to extract the maximum power by making the operating point coincide with the MPP. At some point, the C_1 working condition switches to another condition C_2, of course different. Based on this new condition, the duty cycle will be adjusted so that the initial voltage V_{MPP_1} is assigned to the value V_{MPP_2} which will match the operating point to the new maximum power point MPP_2 on the new feature; (following the yellow arrows).

Otherwise, corresponding to the absence of a continuation, and therefore to the absence of adjustment of the voltage of the operating point; the PVG keeps the same initial voltage V_{MPP_1} , but as the working condition has changed, the operating point has migrated to the new feature by assigning a power P that is less than the max power that could be produced in this new working condition (green arrows).

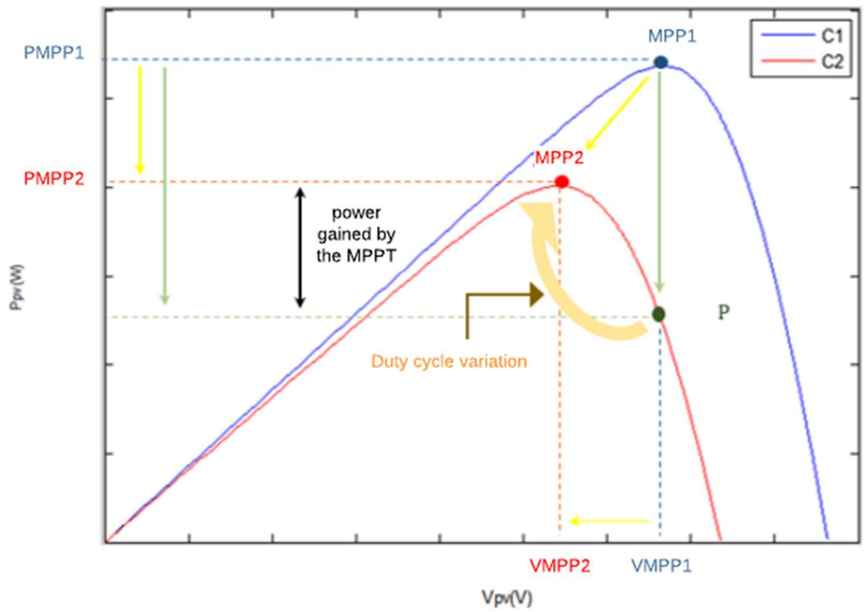

Fig.IV. 11 MPPT working principle.

IV.4.2 P&O

The Perturb and Observe (P&O) is considered as a sampling method [25], it is based on changing the operating point until it coincides with the MPP, which is in fact the result of several iterations. It consists of perturbing the system by increasing or decreasing the operating voltage of the module and observing what occurs at the output level of the power, hence, it justifies its name : Perturb and Observe, according to this observation, the algorithm decides on the act to be done during the next iteration. Fig. IV.12 shows the cases considered for this technique, and summarized in Table IV.1.

If the voltage disturbance of the PVG is in a given direction, and the extracted power increases ($P_{PV} \rangle\ 0$), this means that the Functional Point (FP) has moved towards the MPP and, therefore, the voltage must be disturbed in the same direction. Otherwise, if the drawn power decreases ($P_{PV} \langle\ 0$), it means that the FP has moved away from the PPM and therefore the direction of the voltage disturbance must be reversed.

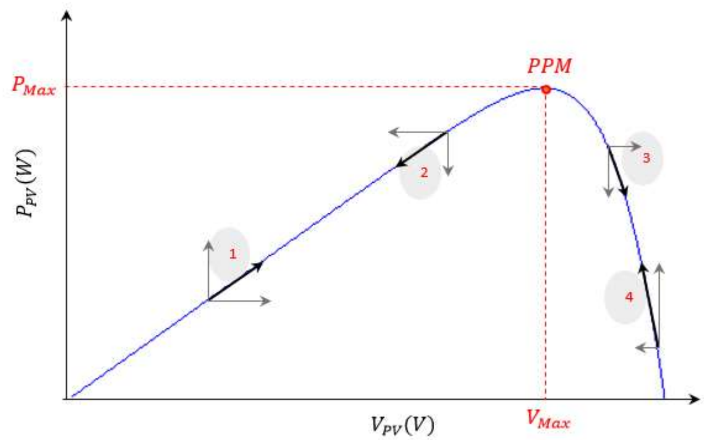

Fig.IV. 12 P&O principal diagram

Table IV. 1 P&O MPPT possible tracking directions

Case n°	ΔV_{PV}	ΔP_{PV}	$\frac{\Delta P_{PV}}{\Delta V_{PV}}$	Tracking direction	control action
1	+	+	+	Good	Increment $V_{ref} = V_{ref} + C$
2	-	-	+	Bad	Increment $V_{ref} = V_{ref} + C$
3	+	-	-	Good	Decrement $V_{ref} = V_{ref} - C$
4	-	+	-	Bad	Decrement $V_{ref} = V_{ref} - C$

Fig.IV.13 shows the classical algorithm associated with the P&O MPPT control technique, where the evolution of the power is analyzed at each sampling moment from the past and present values of current and voltage.

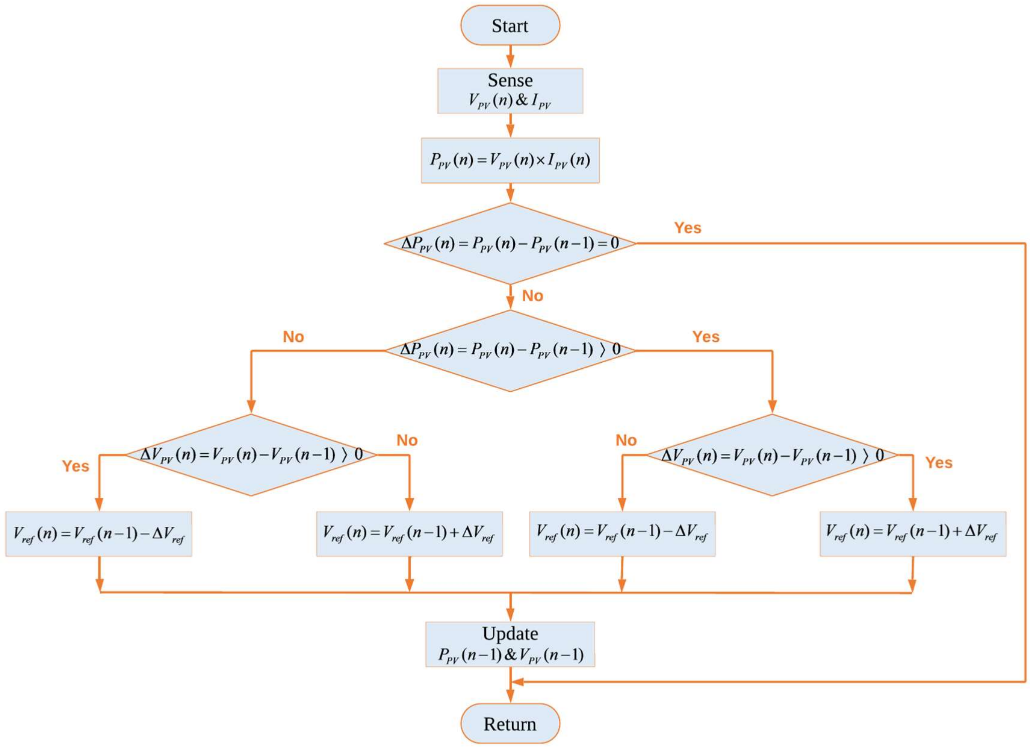

Fig.IV. 13 P&O flowchart

IV.5 Simulation

The system considered in this study is made up of two 2kW rated power PV arrays. As illustrated in Fig.IV.14. Each PV array output power is processed by a P&O MPPT-based DC-DC converter and the connection to the grid utility is performed by a three-phase inverter according to the grid restrictions. The inverter is controlled by the hierarchical control presented in previous chapters.

The electrical characteristics of the used PVG are specified in Table IV.2. According to the irradiation profiles of Fig.IV.15(a), the power generated by each PVG is illustrated in Fig.IV.15(b),

Table IV. 2 Technical specifications of photovoltaic array

Parameter	value
Maximum power per module	2000 W
Short circuit current per cell	4.8 V
Open circuit voltage per cell	21.7 V
Number of modules in series	5
Number of modules in parallel	3

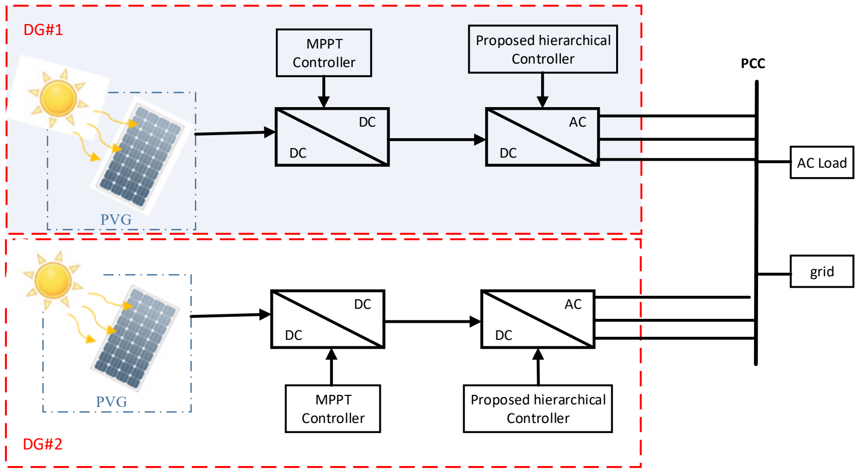

Fig.IV. 14 Block diagram of the simulation

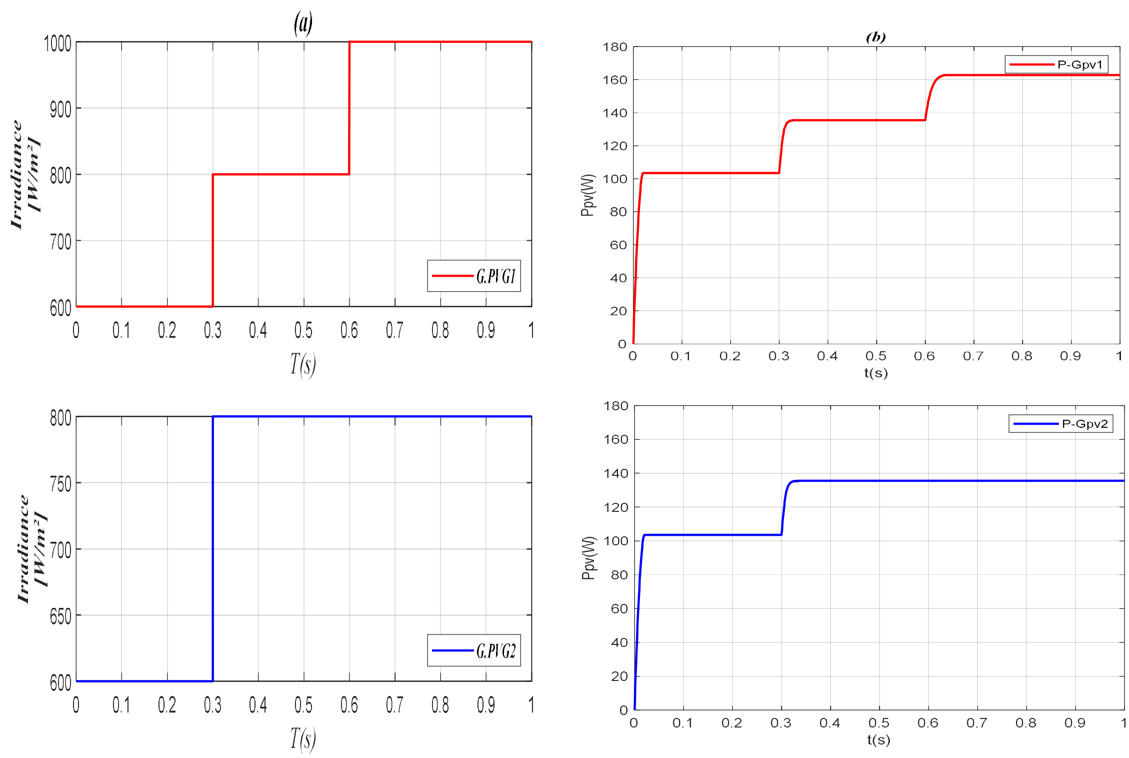

Fig.IV. 15 (a) Irradiation profiles (b) Corresponding generated power.

When the PVG operates under uniform conditions, its P-V characteristic curve exhibits a single MPP. However, if some parts of the PVG are shaded, two or more power peaks, depending on the number of irradiation levels, result in the P-V characteristic curve as can be seen from Fig.IV.15(b).

The studied PVMG along with the designed controller, is tested considering the case studies listed below, noting that they all start with no-load, and then a common load is added at t=0.1s, where only the primary control is activated. The secondary control is activated later at t=0.5s.

Case 01: Uniform Condition

In the first test, the two PVGs are exposed to the same irradiation level set to 850W/m^2. Meaning that both of them generate the same power rate.

Case 02: Shading Condition

In this case, PVG#02 is shaded, which means that the irradiation level drops from 850W/m^2 to 500W/m^2, hence, the generated power from the two units is not the same.

Case 03: Generator disconnection

In this case, a failure occurs in the second PV array at t=0.7s, which leads to the disconnection of this later.

Case 04: On-grid mode

In this case, the tertiary control is activated, and the two PVGs are not exposed to irradiation (i.e. night), the load is then fed from the grid.

Figs.IV.16-23 show the obtained results of this simulation tests, where the active power, voltage and current of the PVGs, grid and at the PCC are illustrated.

In Fig.IV.16, the active power is shared equally between the two generators when they are exposed to the same irradiation level. At t=0.5s, when the secondary control was activated, the frequency and amplitude are restored to their nominal values. In addition, the voltage and current are maintained stable as shown in Fig.17, meaning that the proposed controller is working as required with the PVMG.

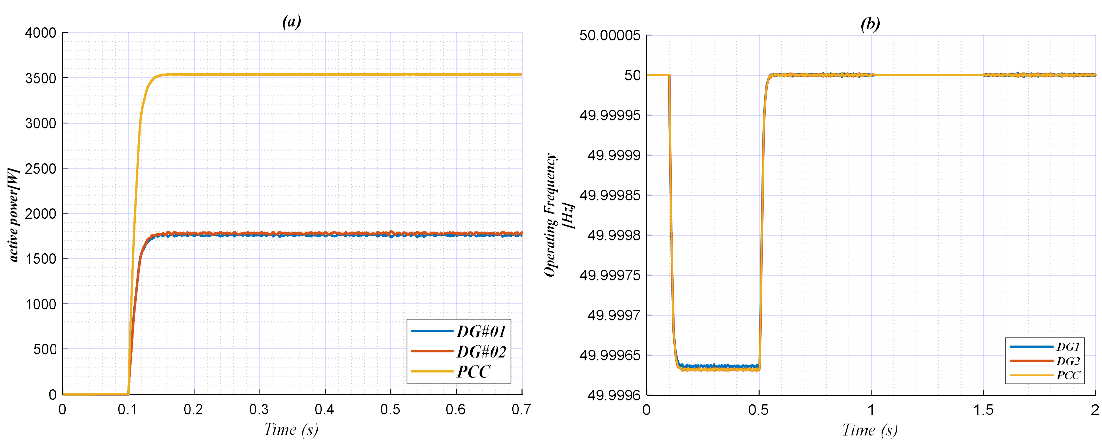

Fig.IV. 16 Obtained generated power in response to case 01

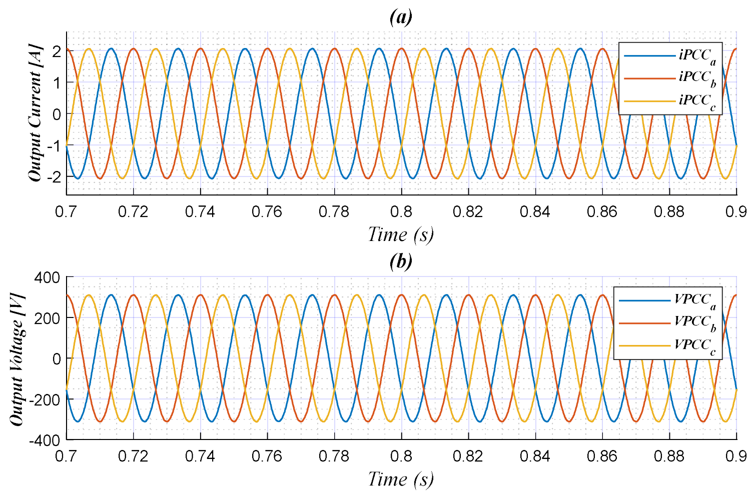

Fig.IV. 17 (a) Current and (b) voltage waveforms in response to case 01

In the case of the shading condition, the load power is shared between PVGs but with different rates, so that PVG#01 generates more than PVG#02 as illustrated in Fig.IV.18.

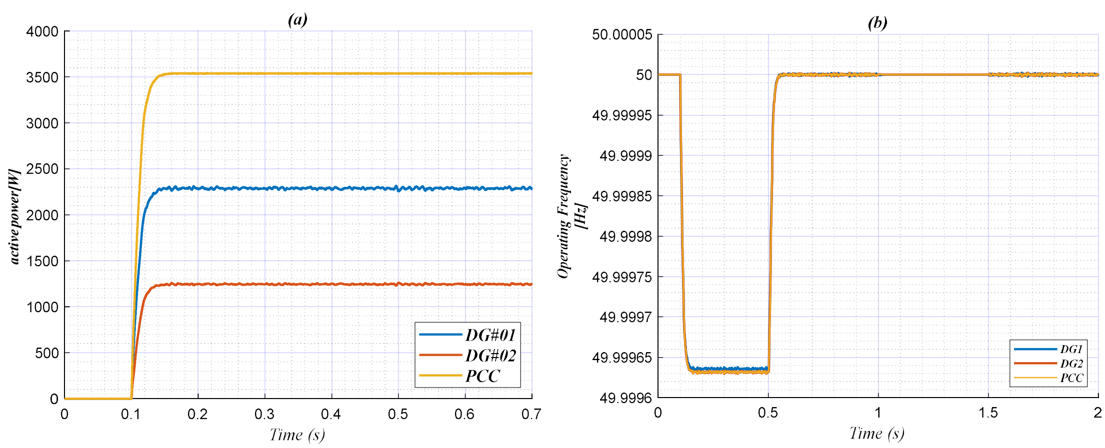

Fig.IV. 18 Obtained (a) generated power and (b) frequency in response to case 02

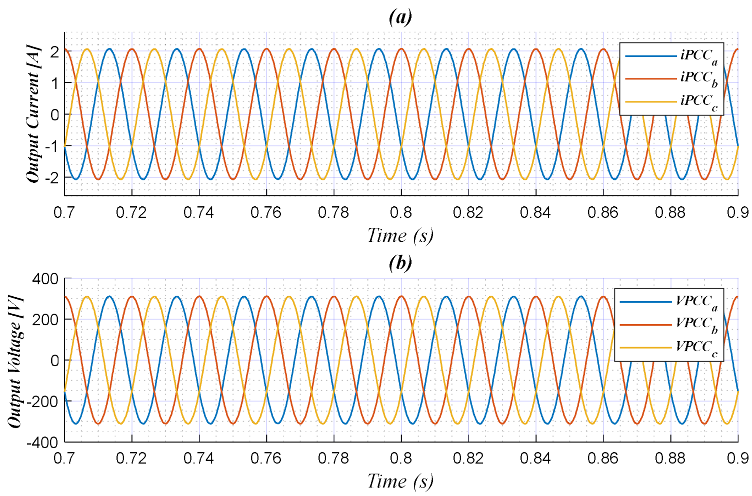

Fig.IV. 19 (a) Current and (b) voltage waveforms in response to case 02

Fig.IV.20 represents the active power generated in the case of the disconnection of PVG#02 at t=0.8s. It can be seen that this failure didn't affect the operation of the controller, where the PVG#01 continued generating the required power to the common load.

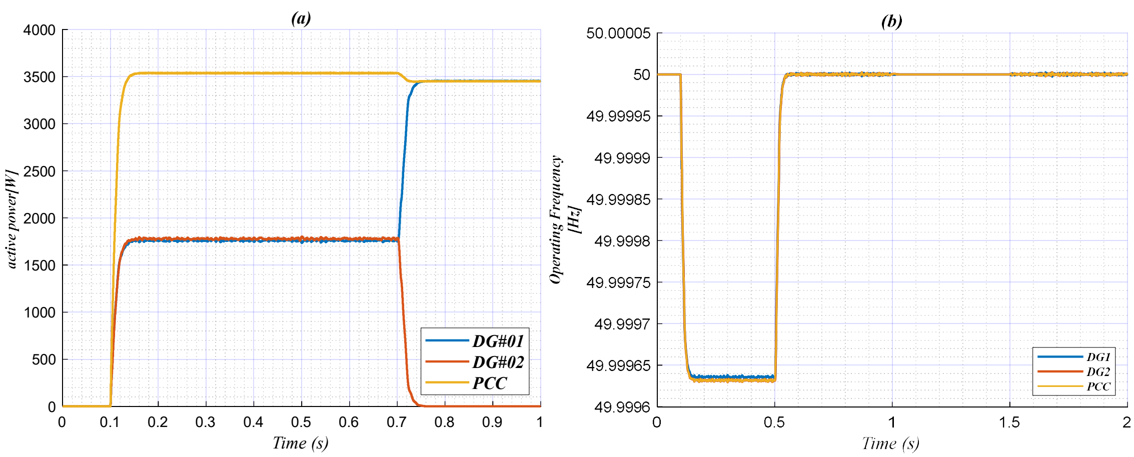

Fig.IV. 20 Obtained (a) generated power and (b) frequency in response to case 03

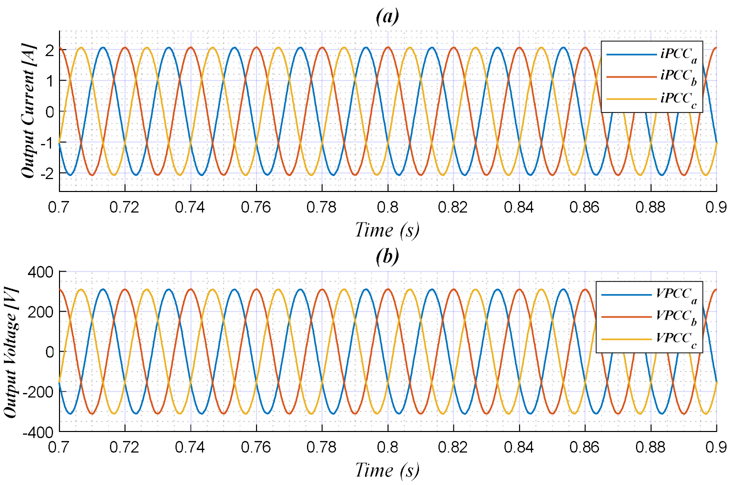

Fig.IV. 21 (a) Current and (b) voltage waveforms in response to case 03

In the last scenario, it is considered that the PVGs are not lighted, in this case, the main grid takes the responsibility of feeding the load, as shown in Fig.IV.22,

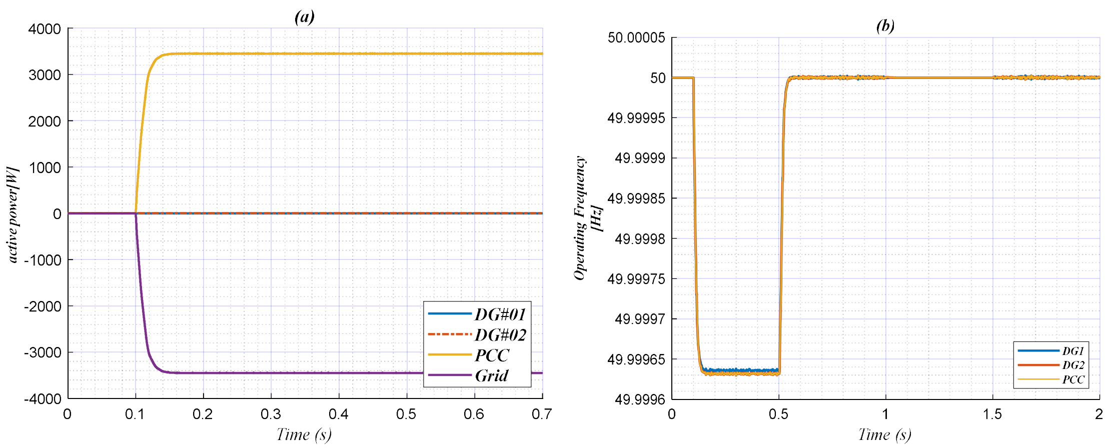

Fig.IV. 22 Obtained (a) generated power and (b) frequency in response to case 04

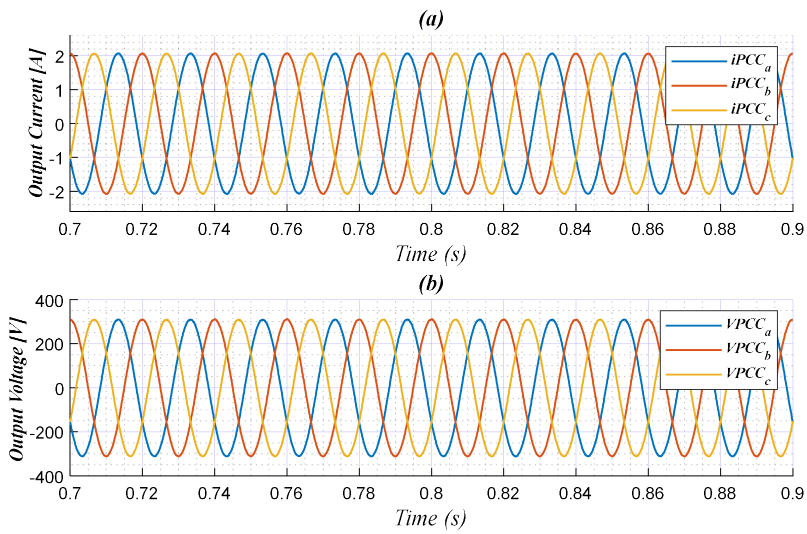

Fig.IV. 23 Current and voltage waveforms in response to case 04

IV.6 Conclusion

In this chapter, the proposed hierarchical control for three-phase droop-controlled VSIs-interfaced *PVMG* during islanded and grid-connected mode operation was addressed. The system was simulated under various conditions to validate the results of the previous chapters using the MATLAB/Simulink software framework.

Firstly, the designed primary control successfully achieved its objectives of attaining the desired references as well as sharing the load between the different PV arrays. In addition, the results have proved the robustness of the designed secondary control in effectively recovering the frequency and amplitude nominal values with good transient and steady-state responses, even under different load conditions. Finally, the obtained results of the power flow control of the PVMG operating in grid-supporting mode have demonstrated the effectiveness of the designed controller in providing a system that can immediately respond to changes in load.

All in all, the presented results in this chapter have successfully validated the effectiveness of the proposed hierarchical control model, including primary, secondary, and tertiary schemes, for three-phase *PVMG*. In addition, it confirmed the developed modeling approach and revealed that the expected transient responses are achieved based on the suggested tuning guideline given in the previous chapters.

Conclusion and future works

The primary aim of this thesis was to model, analyze, and design hierarchical control schemes for a three-phase PV MG during islanding and grid-connection operations. It addressed the control context and problem statement in the general introduction. And subsequently provided an overview of the main contributions, outcomes, and organizational structure of the thesis. The following is a summary of the contributions of the MG control strategies employed in each chapter.

Chapter 1 provided a comprehensive examination of the MG landscape, encompassing its background, definition, research interests, various configurations, advantages, architectures, and motivations. The hierarchical control structure of AC MGs, consisting of primary, secondary, and tertiary control levels, was delineated along with a literature review and associated challenges.

Secondary and tertiary control techniques for three-phase parallel-connected VSIs within AC MG were initially designed in Chapter 3 and were based on the DESOGI-FLL method. A modeling technique was suggested for the specified secondary frequency and amplitude restoration control loops, in addition, a methodical tuning recommendation for choosing the restoration control settings correctly was offered. Furthermore, the synchronization control-loops architecture and modeling were shown. To confirm the efficacy and resilience of the proposed control layers design, simulations were carried out.

The fourth chapter concentrated on modeling the PV MG controlled by the proposed hierarchical control, taking into account the MPPT-controlled DC-DC converter.

Based on the results discussions, one can conclude that:

- The designed secondary control achieves voltage amplitude and frequency restoration to nominal values with the desired transient responses in terms of response time and without overshoot, as well as it has improved the reactive power-sharing.
- The effectiveness and robustness of the designed secondary control are confirmed in ensuring efficient and stable operation of the autonomous MG under different operating conditions and even in the presence of the DC component.
- The simulation tests validate the secondary control proposal in keeping the frequency and voltage amplitude close to their nominal values under various disturbances.
- The synchronization algorithm ensures a seamless transition from islanding mode to grid-connected mode.
- The tertiary can manage optimally the active and reactive exchange between the droop-controlled VSI-based MG and the main grid.

- The proper tracking of the frequency and amplitude of the voltage grid is guaranteed with excellent transient and steady-state performance.

- Stable operation of the grid-connected MG is assured under different grid voltage disturbances which contain the DC component and load changes.

On the basis of the promising findings presented in this thesis, work on the remaining issues is continuing and will be presented in the future by:

- Applying the same design and modeling approaches, for the distributed MG.

- Implementing the designed hierarchical control scheme in hardware, for three-phase VSIs.

Bibliography

[1] E. Hosseini, and G. Shahgholian, “Output power levelling for DFIG wind turbine system using intelligent pitch angle control,” *Automatika,* vol. 58, no. 4, pp. 363-374, , 2017.

[2] G. Shahgholian, S. Eshtehardiha, H. Mahdavi-Nasab, and M. R. Yousefi, "A novel approach in automatic control based on the genetic algorithm in STATCOM for improvement power system transient stability." pp. 414-419.

[3] G. Shahgholian, M. Mahdavian, M. Janghorbani, I. Eshaghpour, and E. Ganji, "Analysis and simulation of UPFC in electrical power system for power flow control." pp. 62-65.

[4] https://www.statista.com/aboutus/our-research-commitment.

[5] I. Chaouki, and K. V. Fedorovich, “Using a Micro-grid to solve the problem of power outages and shortages in southern Algeria during the summer,” *IOP Conference Series: Earth and Environmental Science,* vol. 1045, no. 1, pp. 012010, , 2022.

[6] https://www.cder.dz/?lang=en.

[7] Y. Han, H. Li, L. Xu, X. Zhao, and J. M. Guerrero, “Analysis of Washout Filter-Based Power Sharing Strategy—An Equivalent Secondary Controller for Islanded Microgrid Without LBC Lines,” *IEEE Transactions on Smart Grid,* vol. 9, no. 5, pp. 4061-4076, 2018.

[8] J. G. d. Matos, F. S. F. e. Silva, and L. A. d. S. Ribeiro, “Power Control in AC Isolated Microgrids With Renewable Energy Sources and Energy Storage Systems,” *IEEE Transactions on Industrial Electronics,* vol. 62, no. 6, pp. 3490-3498, 2015.

[9] D. Xu, Y. Dai, C. Yang, and X. Yan, “Adaptive fuzzy sliding mode command-filtered backstepping control for islanded PV microgrid with energy storage system,” *Journal of the Franklin Institute,* vol. 356, no. 4, pp. 1880-1898, 2019.

[10] M. Aryanezhad, “Management and coordination of LTC, SVR, shunt capacitor and energy storage with high PV penetration in power distribution system for voltage regulation and power loss minimization,” *International Journal of Electrical Power & Energy Systems,* vol. 100, pp. 178-192, 2018.

[11] A. Mehrizi-Sani, and R. Iravani, “Potential-Function Based Control of a Microgrid in Islanded and Grid-Connected Modes,” *IEEE Transactions on Power Systems,* vol. 25, no. 4, pp. 1883-1891, 2010.

[12] W. Liu, T. Tarasiuk, M. Gorniak, M. Savaghebi, J. C. Vasquez, C. L. Su, and J. M. Guerrero, “Power Quality Assessment in Shipboard Microgrids Under Unbalanced and Harmonic AC Bus Voltage,” *IEEE Transactions on Industry Applications,* vol. 55, no. 1, pp. 765-775, 2019.

[13] A. Ranjbaran, and M. Ebadian, “A power sharing scheme for voltage unbalance and harmonics compensation in an islanded microgrid,” *Electric Power Systems Research,* vol. 155, pp. 153-163, 2018.

[14] S. Choudhury, “A comprehensive review on issues, investigations, control and protection trends, technical challenges and future directions for Microgrid technology,” *International Transactions on Electrical Energy Systems,* vol. 30, no. 9, pp. e12446, 2020.

[15] A. Vasilakis, I. Zafeiratou, D. T. Lagos, and N. D. Hatziargyriou, “The Evolution of Research in Microgrids Control,” *IEEE Open Access Journal of Power and Energy,* vol. 7, pp. 331-343, 2020.

[16] A. Mohammed, S. S. Refaat, S. Bayhan, and H. Abu-Rub, “AC Microgrid Control and Management Strategies: Evaluation and Review,” *IEEE Power Electronics Magazine,* vol. 6, no. 2, pp. 18-31, 2019.

[17] S. Sen, and V. Kumar, “Microgrid control: A comprehensive survey,” *Annual Reviews in Control,* vol. 45, pp. 118-151, 2018.

[18] S. M. Kaviri, M. Pahlevani, P. Jain, and A. Bakhshai, "A review of AC microgrid control methods." pp. 1-8.

[19] A. Shalchi, M. Abbasi, E. Abbasi, B. Tousi, and G. B. Gharehpetian, “New DTR line selection method in a power system comprising DTR, ESS, and RES for increasing RES integration and minimising load shedding,” *IET Generation, Transmission & Distribution,* vol. 14, no. 25, pp. 6319-6329, 2020.

[20] K. Gholami, M. Abbasi, A. Azizivahed, and L. Li, “An efficient bi-objective approach for dynamic economic emission dispatch of renewable-integrated microgrids,” *Journal of Ambient Intelligence and Humanized Computing,* vol. 14, no. 8, pp. 10695-10714, 2023.

[21] T. Morstyn, B. Hredzak, and V. G. Agelidis, “Control Strategies for Microgrids With Distributed Energy Storage Systems: An Overview,” *IEEE Transactions on Smart Grid,* vol. 9, no. 4, pp. 3652-3666, 2018.

[22] A. Tuladhar, J. Hua, T. Unger, and K. Mauch, “Control of parallel inverters in distributed AC power systems with consideration of line impedance effect,” *IEEE Transactions on Industry Applications,* vol. 36, no. 1, pp. 131-138, 2000.

[23] K. S. Rajesh, S. S. Dash, R. Rajagopal, and R. Sridhar, “A review on control of ac microgrid,” *Renewable and Sustainable Energy Reviews,* vol. 71, pp. 814-819, 2017.

[24] S. Parhizi, H. Lotfi, A. Khodaei, and S. Bahramirad, “State of the Art in Research on Microgrids: A Review,” *IEEE Access,* vol. 3, pp. 890-925, 2015.

[25] L. Viswanathan, and S. Kumar, “A review: Control strategies for power quality improvement in microgrid,” *International Journal of Renewable Energy Research,* vol. 8, pp. 150-165, 01/01, 2018.

[26] “IEEE Standard for the Specification of Microgrid Controllers,” *IEEE Std 2030.7-2017*, pp. 1-43, 2018.

[27] D. T. Ton, and M. A. Smith, “The U.S. Department of Energy's Microgrid Initiative,” *The Electricity Journal,* vol. 25, no. 8, pp. 84-94 , 2012.

[28] O. Palizban, and K. Kauhaniemi, "Microgrid control principles in island mode operation." pp. 1-6.

[29] W. Al-Saedi, S. W. Lachowicz, D. Habibi, and O. Bass, “Power flow control in grid-connected microgrid operation using Particle Swarm Optimization under variable load conditions,” *International Journal of Electrical Power & Energy Systems,* vol. 49, pp. 76-85, 2013.

[30] C. A. Marnay, C.; Joos, G.; Ash, K.; Bando, S.; Braun, M.; Chatzivasileiadis, S.; Driesen, J.; Hatziargyriou, N.; Iravani, R.; et al, “Microgrid Evolution Roadmap Engineering, Economics, and Experience,” in 2015 International Symposium on Smart Electric Distribution Systems and Technologies (EDST15).

[31] F. M. A.-S. Magdi S. Mahmoud "control methods for microgrids," *Control and Optimization of Distributed Generation Systems*: power systems, springer, 2015.

[32] D. E. Olivares, A. Mehrizi-Sani, A. H. Etemadi, C. A. Cañizares, R. Iravani, M. Kazerani, A. H. Hajimiragha, O. Gomis-Bellmunt, M. Saeedifard, R. Palma-Behnke, G. A. Jiménez-Estévez, and N. D. Hatziargyriou, “Trends in Microgrid Control,” *IEEE Transactions on Smart Grid,* vol. 5, no. 4, pp. 1905-1919, 2014.

[33] A. Hirsch, Y. Parag, and J. Guerrero, “Microgrids: A review of technologies, key drivers, and outstanding issues,” *Renewable and Sustainable Energy Reviews,* vol. 90, pp. 402-411, 2018.

[34] P. P. Barker, and R. W. D. Mello, "Determining the impact of distributed generation on power systems. I. Radial distribution systems." pp. 1645-1656 vol. 3.

[35] X. Hou, Y. Sun, X. Zhang, G. Zhang, J. Lu, and F. Blaabjerg, “A Self-Synchronized Decentralized Control for Series-Connected H-Bridge Rectifiers,” *IEEE Transactions on Power Electronics,* vol. 34, no. 8, pp. 7136-7142, 2019.

[36] J. He, Y. Li, C. Wang, Y. Pan, C. Zhang, and X. Xing, “Hybrid Microgrid With Parallel- and Series-Connected Microconverters,” *IEEE Transactions on Power Electronics,* vol. 33, no. 6, pp. 4817-4831, 2018.

[37] X. Ge, H. Han, W. Yuan, Y. Sun, M. Su, X. Zhang, and K. L. Hai, "An Integrated Series-Parallel Microgrid Structure and its Unified Distributed Control." pp. 1-6.

[38] Y. Wang, Z. Chen, X. Wang, Y. Tian, Y. Tan, and C. Yang, “An Estimator-Based Distributed Voltage-Predictive Control Strategy for AC Islanded Microgrids,” *IEEE Transactions on Power Electronics,* vol. 30, no. 7, pp. 3934-3951, 2015.

[39] W. Yuan, Y. Wang, X. Ge, X. Hou, and H. Han, “A Unified Distributed Control Strategy for Hybrid Cascaded-Parallel Microgrid,” *IEEE Transactions on Energy Conversion,* vol. 34, no. 4, pp. 2029-2040, 2019.

[40] X. Wei, X. Xiangning, and C. Pengwei, “Overview of key microgrid technologies,” *International Transactions on Electrical Energy Systems,* vol. 28, no. 7, pp. e2566, 2018.

[41] Y. Yoldaş, A. Önen, S. M. Muyeen, A. V. Vasilakos, and İ. Alan, “Enhancing smart grid with microgrids: Challenges and opportunities,” *Renewable and Sustainable Energy Reviews,* vol. 72, pp. 205-214, 2017/05/01/, 2017.

[42] E. Unamuno, and J. A. Barrena, “Hybrid ac/dc microgrids—Part I: Review and classification of topologies,” *Renewable and Sustainable Energy Reviews,* vol. 52, pp. 1251-1259, 2015/12/01/, 2015.

[43] J. M. Guerrero, J. C. Vasquez, J. Matas, L. G. d. Vicuna, and M. Castilla, “Hierarchical Control of Droop-Controlled AC and DC Microgrids—A General Approach Toward Standardization,” *IEEE Transactions on Industrial Electronics,* vol. 58, no. 1, pp. 158-172, 2011.

[44] M. Farrokhabadi, C. A. Cañizares, J. W. Simpson-Porco, E. Nasr, L. Fan, P. A. Mendoza-Araya, R. Tonkoski, U. Tamrakar, N. Hatziargyriou, D. Lagos, R. W. Wies, M. Paolone, M. Liserre, L. Meegahapola, M. Kabalan, A. H. Hajimiragha, D. Peralta, M. A. Elizondo, K. P. Schneider, F. K. Tuffner, and J. Reilly, “Microgrid Stability Definitions, Analysis, and Examples,” *IEEE Transactions on Power Systems,* vol. 35, no. 1, pp. 13-29, 2020.

[45] X. Zhu, X.-q. Han, W.-p. Qin, and P. Wang, “Past, today and future development of micro-grids in China,” *Renewable and Sustainable Energy Reviews,* vol. 42, pp. 1453-1463, 2015/02/01/, 2015.

[46] J. J. Justo, F. Mwasilu, J. Lee, and J.-W. Jung, “AC-microgrids versus DC-microgrids with distributed energy resources: A review,” *Renewable and Sustainable Energy Reviews,* vol. 24, pp. 387-405, 2013.

[47] I. Patrao, E. Figueres, G. Garcerá, and R. González-Medina, “Microgrid architectures for low voltage distributed generation,” *Renewable and Sustainable Energy Reviews,* vol. 43, pp. 415-424 , 2015.

[48] L. Che, and M. Shahidehpour, “DC Microgrids: Economic Operation and Enhancement of Resilience by Hierarchical Control,” *IEEE Transactions on Smart Grid,* vol. 5, no. 5, pp. 2517-2526, 2014.

[49] E. Planas, J. Andreu, J. I. Gárate, I. Martínez de Alegría, and E. Ibarra, “AC and DC technology in microgrids: A review,” *Renewable and Sustainable Energy Reviews,* vol. 43, pp. 726-749, 2015.

[50] M. A. R. Tavakkoli, A.; Hassibi, H. , “Simulation and analysis of a compact electronic infrastructure for DC micro-grid: Necessity and challenges.,” *Smart Grid Renew. Energy 2012, 3, 73.* .

[51] H. Kakigano, Y. Miura, and T. Ise, “Low-Voltage Bipolar-Type DC Microgrid for Super High Quality Distribution,” *IEEE Transactions on Power Electronics,* vol. 25, no. 12, pp. 3066-3075, 2010.

[52] G. Ding, F. Gao, S. Zhang, P. C. Loh, and F. Blaabjerg, “Control of hybrid AC/DC microgrid under islanding operational conditions,” *Journal of Modern Power Systems and Clean Energy,* vol. 2, no. 3, pp. 223-232, 2014.

[53] M. N. Ambia, H. M. Hasanien, A. Al-Durra, and S. M. Muyeen, “Harmony Search Algorithm-Based Controller Parameters Optimization for a Distributed-Generation System,” *IEEE Transactions on Power Delivery,* vol. 30, no. 1, pp. 246-255, 2015.

[54] F. Nejabatkhah, Y. W. Li, and H. Tian, “Power Quality Control of Smart Hybrid AC/DC Microgrids: An Overview,” *IEEE Access,* vol. 7, pp. 52295-52318, 2019.

[55] F. Hassan, and J. Geza, "Control, Monitoring, and Protection Strategies," *Microgrid Planning and Design: A Concise Guide*, pp. 65-90: IEEE, 2019.

[56] T. Prabaksorn, R. T. Naayagi, and S. S. Lee, "Modelling and Simulation of Microgrid in Grid-Connected Mode and Islanded Mode." pp. 1-8.

[57] N. Nasser, and M. Fazeli, “Buffered-Microgrid Structure for Future Power Networks; a Seamless Microgrid Control,” *IEEE Transactions on Smart Grid,* vol. 12, no. 1, pp. 131-140, 2021.

[58] N. Pogaku, M. Prodanovic, and T. C. Green, “Modeling, Analysis and Testing of Autonomous Operation of an Inverter-Based Microgrid,” *IEEE Transactions on Power Electronics,* vol. 22, no. 2, pp. 613-625, 2007.

[59] Y. A. R. I. Mohamed, and E. F. El-Saadany, “Adaptive Decentralized Droop Controller to Preserve Power Sharing Stability of Paralleled Inverters in Distributed Generation Microgrids,” *IEEE Transactions on Power Electronics,* vol. 23, no. 6, pp. 2806-2816, 2008.

[60] T. L. Lee, and P. T. Cheng, “Design of a New Cooperative Harmonic Filtering Strategy for Distributed Generation Interface Converters in an Islanding Network,” *IEEE Transactions on Power Electronics,* vol. 22, no. 5, pp. 1919-1927, 2007.

[61] Q. Li, Z. Xu, and L. Yang, “Recent advancements on the development of microgrids,” *Journal of Modern Power Systems and Clean Energy,* vol. 2, no. 3, pp. 206-211, 2014.

[62] M. El-Hendawi, H. A. Gabbar, G. El-Saady, and E.-N. A. Ibrahim, “Control and EMS of a Grid-Connected Microgrid with Economical Analysis,” *Energies,* vol. 11, no. 1, pp. 129, 2018.

[63] E. Kabalcı, "Hierarchical Control in Microgrid," pp. 381-401, 2019.

[64] H. R. Baghaee, M. Mirsalim, G. B. Gharehpetian, and H. A. Talebi, “Unbalanced harmonic power sharing and voltage compensation of microgrids using radial basis function neural network-based harmonic power-flow calculations for distributed and decentralised control structures,” *IET Generation, Transmission & Distribution,* vol. 12, no. 7, pp. 1518-1530, 2018.

[65] L. Meng, F. Tang, M. Savaghebi, J. C. Vasquez, and J. M. Guerrero, “Tertiary Control of Voltage Unbalance Compensation for Optimal Power Quality in Islanded Microgrids,” *IEEE Transactions on Energy Conversion,* vol. 29, no. 4, pp. 802-815, 2014.

[66] C. D. Korkas, S. Baldi, I. Michailidis, and E. B. Kosmatopoulos, “Occupancy-based demand response and thermal comfort optimization in microgrids with renewable energy sources and energy storage,” *Applied Energy,* vol. 163, pp. 93-104, 2016.

[67] B. Aluisio, M. Dicorato, G. Forte, G. Litrico, and M. Trovato, “Integration of heat production and thermal comfort models in microgrid operation planning,” *Sustainable Energy, Grids and Networks,* vol. 16, pp. 37-54, 2018/12/01/, 2018.

[68] Y. Liu, N. Yu, W. Wang, X. Guan, Z. Xu, B. Dong, and T. Liu, “Coordinating the operations of smart buildings in smart grids,” *Applied Energy,* vol. 228, pp. 2510-2525, 2018.

[69] Y. Guan, J. C. Vasquez, and J. M. Guerrero, "Hierarchical controlled grid-connected microgrid based on a novel autonomous current sharing controller." pp. 2333-2340.

[70] M. H. Cintuglu, T. Youssef, and O. A. Mohammed, “Development and Application of a Real-Time Testbed for Multiagent System Interoperability: A Case Study on Hierarchical Microgrid Control,” *IEEE Transactions on Smart Grid,* vol. 9, no. 3, pp. 1759-1768, 2018.

[71] C. X. Dou, and B. Liu, “Multi-Agent Based Hierarchical Hybrid Control for Smart Microgrid,” *IEEE Transactions on Smart Grid,* vol. 4, no. 2, pp. 771-778, 2013.

[72] M. Nassourou, V. Puig, J. Blesa, and C. Ocampo-Martinez, "Economic model predictive control for energy dispatch of a smart micro-grid system." pp. 0944-0949.

[73] P. R. C. Mendes, L. V. Isorna, C. Bordons, and J. E. Normey-Rico, “Energy management of an experimental microgrid coupled to a V2G system,” *Journal of Power Sources,* vol. 327, pp. 702-713, 2016.

[74] D. Wang, J. Qiu, L. Reedman, K. Meng, and L. L. Lai, “Two-stage energy management for networked microgrids with high renewable penetration,” *Applied Energy,* vol. 226, pp. 39-48, 2018.

[75] F. J. Heredia, M. D. Cuadrado, and C. Corchero, “On optimal participation in the electricity markets of wind power plants with battery energy storage systems,” *Computers & Operations Research,* vol. 96, pp. 316-329, 2018.

[76] J. C. Vasquez, J. M. Guerrero, M. Savaghebi, J. Eloy-Garcia, and R. Teodorescu, “Modeling, Analysis, and Design of Stationary-Reference-Frame Droop-Controlled Parallel Three-Phase Voltage Source Inverters,” *IEEE Transactions on Industrial Electronics,* vol. 60, no. 4, pp. 1271-1280, 2013.

[77] J. M. Guerrero, L. G. d. Vicuna, J. Matas, M. Castilla, and J. Miret, “A wireless controller to enhance dynamic performance of parallel inverters in distributed generation systems,” *IEEE Transactions on Power Electronics,* vol. 19, no. 5, pp. 1205-1213, 2004.

[78] Z. Jiang, and X. Yu, "Active power — Voltage control scheme for islanding operation of inverter-interfaced microgrids." pp. 1-7.

[79] J. M. Guerrero, V. Luis Garcia de, J. Matas, M. Castilla, and J. Miret, “Output impedance design of parallel-connected UPS inverters with wireless load-sharing control,” *IEEE Transactions on Industrial Electronics,* vol. 52, no. 4, pp. 1126-1135, 2005.

[80] S. Sinha, S. Ghosh, and P. Bajpai, “Power sharing through interlinking converters in adaptive droop controlled multiple microgrid system,” *International Journal of Electrical Power & Energy Systems,* vol. 128, pp. 106649 , 2021.

[81] W. Yao, M. Chen, J. Matas, J. M. Guerrero, and Z. M. Qian, “Design and Analysis of the Droop Control Method for Parallel Inverters Considering the Impact of the Complex Impedance on the Power Sharing,” *IEEE Transactions on Industrial Electronics,* vol. 58, no. 2, pp. 576-588, 2011.

[82] U. B. Tayab, M. A. B. Roslan, L. J. Hwai, and M. Kashif, “A review of droop control techniques for microgrid,” *Renewable and Sustainable Energy Reviews,* vol. 76, pp. 717-727, 2017.

[83] L. Meng, A. Luna, E. R. Díaz, B. Sun, T. Dragicevic, M. Savaghebi, J. C. Vasquez, J. M. Guerrero, M. Graells, and F. Andrade, “Flexible System Integration and Advanced Hierarchical Control Architectures in the Microgrid Research Laboratory of Aalborg University,” *IEEE Transactions on Industry Applications,* vol. 52, no. 2, pp. 1736-1749, 2016.

[84] R. Hidalgo-León, C. Sanchez-Zurita, P. Jácome-Ruiz, J. Wu, and Y. Muñoz-Jadan, "Roles, challenges, and approaches of droop control methods for microgrids." pp. 1-6.

[85] A. Micallef, M. Apap, C. Spiteri-Staines, and J. M. Guerrero, “Single-Phase Microgrid With Seamless Transition Capabilities Between Modes of Operation,” *IEEE Transactions on Smart Grid,* vol. 6, no. 6, pp. 2736-2745, 2015.

[86] M. Anwar, M. I. Marei, and A. A. El-Sattar, "Generalized droop-based control for an islanded microgrid." pp. 717-722.

[87] R. Moslemi, and J. Mohammadpour, “Accurate reactive power control of autonomous microgrids using an adaptive virtual inductance loop,” *Electric Power Systems Research,* vol. 129, pp. 142-149, 2015.

[88] V. Verma, and G. G. Talpur, "Decentralized Master-Slave operation of microgrid using current controlled distributed generation sources." pp. 1-6.

[89] G. G. Talapur, H. M. Suryawanshi, A. B. Shitole, R. R. Deshmukh, and M. S. Ballal, "Master-slave control based reliable micro-Grid with back-to-back voltage source converter as master DG." pp. 310-315.

[90] L. K. Vedulla, and M. K. Mishra, "PSO based power sharing scheme for an islanded DC microgrid system." pp. 392-397.

[91] J. M. Guerrero, M. Chandorkar, T. L. Lee, and P. C. Loh, “Advanced Control Architectures for Intelligent Microgrids—Part I: Decentralized and Hierarchical Control,” *IEEE Transactions on Industrial Electronics,* vol. 60, no. 4, pp. 1254-1262, 2013.

[92] H. Ye, Y. Liu, W. Pei, and L. Kong, "Efficient droop-based primary frequency control from variable-speed wind turbines and energy storage systems." pp. 1-5.

[93] A. Bendib, A. Kherbachi, K. Kara, and A. Chouder, "Droop controller based primary control scheme for parallel-connected single-phase inverters in islanded AC microgrid." pp. 1-6.

[94] J. W. Simpson-Porco, F. Dörfler, and F. Bullo, “Synchronization and power sharing for droop-controlled inverters in islanded microgrids,” *Automatica,* vol. 49, no. 9, pp. 2603-2611, 2013.

[95] H. Mahmood, D. Michaelson, and J. Jiang, “A Power Management Strategy for PV/Battery Hybrid Systems in Islanded Microgrids,” *IEEE Journal of Emerging and Selected Topics in Power Electronics,* vol. 2, no. 4, pp. 870-882, 2014.

[96] Y. Wang, H. Jiang, L. Zhou, and P. Xing, "An Improved Adaptive Droop Control Strategy for Power Sharing in Micro-Grid." pp. 50-53.

[97] A. Bidram, and A. Davoudi, “Hierarchical Structure of Microgrids Control System,” *IEEE Transactions on Smart Grid,* vol. 3, no. 4, pp. 1963-1976, 2012.

[98] T. V. Vu, S. Paran, F. Diaz-Franco, T. El-Mezyani, and C. S. Edrington, “An Alternative Distributed Control Architecture for Improvement in the Transient Response of DC Microgrids,” *IEEE Transactions on Industrial Electronics,* vol. 64, no. 1, pp. 574-584, 2017.

[99] F. Alam, M. Ashfaq, S. S. Zaidi, and A. Y. Memon, "Robust droop control design for a hybrid AC/DC microgrid." pp. 1-6.

[100] Y. Han, H. Li, P. Shen, E. A. A. Coelho, and J. M. Guerrero, “Review of Active and Reactive Power Sharing Strategies in Hierarchical Controlled Microgrids,” *IEEE Transactions on Power Electronics,* vol. 32, no. 3, pp. 2427-2451, 2017.

[101] H. Han, Y. Liu, Y. Sun, M. Su, and J. M. Guerrero, “An Improved Droop Control Strategy for Reactive Power Sharing in Islanded Microgrid,” *IEEE Transactions on Power Electronics,* vol. 30, no. 6, pp. 3133-3141, 2015.

[102] Y. Gupta, K. Chatterjee, and S. Doolla, “A Simple Control Scheme for Improving Reactive Power Sharing in Islanded Microgrid,” *IEEE Transactions on Power Systems,* vol. 35, no. 4, pp. 3158-3169, 2020.

[103] L. Li, Y. Han, P. Yang, Q. Huang, Z. Zhang, and Y. Xu, "A New Distributed Control Strategy for DC Microgrids with Droop Coefficient Correction and DC Bus Voltage Restoration." pp. 3908-3913.

[104] X. Hoa Thi Pham, “Power sharing strategy in islanded microgrids using improved droop control,” *Electric Power Systems Research,* vol. 180, pp. 106164, 2020/03/01/, 2020.

[105] Z. Shuai, S. Mo, J. Wang, Z. J. Shen, W. Tian, and Y. Feng, “Droop control method for load share and voltage regulation in high-voltage microgrids,” *Journal of Modern Power Systems and Clean Energy,* vol. 4, no. 1, pp. 76-86, 2016.

[106] J. Kim, J. M. Guerrero, P. Rodriguez, R. Teodorescu, and K. Nam, “Mode Adaptive Droop Control With Virtual Output Impedances for an Inverter-Based Flexible AC Microgrid,” *IEEE Transactions on Power Electronics,* vol. 26, no. 3, pp. 689-701, 2011.

[107] L. Haoming, C. Yi, L. Shanshan, and H. Yunhe, "Improved droop control of isolated microgrid with virtual impedance." pp. 1-5.

[108] A. S. Vijay, N. Parth, S. Doolla, and M. C. Chandorkar, “An Adaptive Virtual Impedance Control for Improving Power Sharing Among Inverters in Islanded AC Microgrids,” *IEEE Transactions on Smart Grid,* vol. 12, no. 4, pp. 2991-3003, 2021.

[109] J. M. Alcala, M. Castilla, L. G. d. Vicuña, J. Miret, and J. C. Vasquez, “Virtual Impedance Loop for Droop-Controlled Single-Phase Parallel Inverters Using a Second-Order General-Integrator Scheme,” *IEEE Transactions on Power Electronics,* vol. 25, no. 12, pp. 2993-3002, 2010.

[110] A. Kherbachi, A. Chouder, A. Bendib, K. Kara, and S. Barkat, “Enhanced structure of second-order generalized integrator frequency-locked loop suitable for DC-offset rejection in single-phase systems,” *Electric Power Systems Research,* vol. 170, pp. 348-357, 2019.

[111] M. Savaghebi, A. Jalilian, J. C. Vasquez, and J. M. Guerrero, “Secondary Control Scheme for Voltage Unbalance Compensation in an Islanded Droop-Controlled Microgrid,” *IEEE Transactions on Smart Grid,* vol. 3, no. 2, pp. 797-807, 2012.

[112] X. Wang, J. M. Guerrero, F. Blaabjerg, and Z. Chen, "Secondary voltage control for harmonics suppression in islanded microgrids." pp. 1-8.

[113] M. Savaghebi, A. Jalilian, J. C. Vasquez, J. M. Guerrero, and T. L. Lee, "Voltage harmonic compensation of a microgrid operating in islanded and grid-connected modes." pp. 1-1.

[114] Y. Khayat, Q. Shafiee, R. Heydari, M. Naderi, T. Dragičević, J. W. Simpson-Porco, F. Dörfler, M. Fathi, F. Blaabjerg, J. M. Guerrero, and H. Bevrani, “On the Secondary

Control Architectures of AC Microgrids: An Overview," *IEEE Transactions on Power Electronics,* vol. 35, no. 6, pp. 6482-6500, 2020.

[115] Q. Shafiee, J. M. Guerrero, and J. C. Vasquez, "Distributed Secondary Control for Islanded Microgrids—A Novel Approach," *IEEE Transactions on Power Electronics,* vol. 29, no. 2, pp. 1018-1031, 2014.

[116] G. Agundis-Tinajero, J. Segundo-Ramírez, N. Visairo-Cruz, M. Savaghebi, J. M. Guerrero, and E. Barocio, "Power flow modeling of islanded AC microgrids with hierarchical control," *International Journal of Electrical Power & Energy Systems,* vol. 105, pp. 28-36, 2019.

[117] T. Dragičević, R. Heydari, and F. Blaabjerg, "Super-high bandwidth secondary control of AC microgrids." pp. 3036-3042.

[118] R. V. A. Neves, R. Q. Machado, V. A. Oliveira, X. Wang, and F. Blaabjerg, "Multitask Fuzzy Secondary Controller for AC Microgrid Operating in Stand-Alone and Grid-Tied Mode," *IEEE Transactions on Smart Grid,* vol. 10, no. 5, pp. 5640-5649, 2019.

[119] Q. Shafiee, S. Č, T. Dragičević, P. Popovski, J. C. Vasquez, and J. M. Guerrero, "Robust Networked Control Scheme for Distributed Secondary Control of Islanded Microgrids," *IEEE Transactions on Industrial Electronics,* vol. 61, no. 10, pp. 5363-5374, 2014.

[120] Y. Xu, H. Sun, W. Gu, Y. Xu, and Z. Li, "Optimal Distributed Control for Secondary Frequency and Voltage Regulation in an Islanded Microgrid," *IEEE Transactions on Industrial Informatics,* vol. 15, no. 1, pp. 225-235, 2019.

[121] B. Wei, Y. Gui, S. Trujillo, J. M. Guerrero, J. C. Vásquez, and A. Marzàbal, "Distributed Average Integral Secondary Control for Modular UPS Systems-Based Microgrids," *IEEE Transactions on Power Electronics,* vol. 34, no. 7, pp. 6922-6936, 2019.

[122] S. Golestan, J. M. Guerrero, and J. C. Vasquez, "DC-Offset Rejection in Phase-Locked Loops: A Novel Approach," *IEEE Transactions on Industrial Electronics,* vol. 63, no. 8, pp. 4942-4946, 2016.

[123] S. Golestan, J. M. Guerrero, and G. B. Gharehpetian, "Five Approaches to Deal With Problem of DC Offset in Phase-Locked Loop Algorithms: Design Considerations and Performance Evaluations," *IEEE Transactions on Power Electronics,* vol. 31, no. 1, pp. 648-661, 2016.

[124] H. Ahmed, and M. Benbouzid, "Demodulation type single-phase PLL with DC offset rejection," *Electronics Letters,* vol. 56, no. 7, pp. 344-347, 2020.

[125] M. Fan, Z. Dai, Y. Yang, M. Xie, L. He, and G. Du, "Four Consecutive Samples Based Frequency Estimation for Single-Phase Grids With DC Offsets," *IEEE Transactions on Industrial Electronics,* vol. 68, no. 10, pp. 9598-9606, 2021.

[126] B. Liu, M. An, H. Wang, Y. Chen, Z. Zhang, C. Xu, S. Song, and Z. Lv, "A Simple Approach to Reject DC Offset for Single-Phase Synchronous Reference Frame PLL in Grid-Tied Converters," *IEEE Access,* vol. 8, pp. 112297-112308, 2020.

[127] M. Savaghebi, A. Jalilian, J. C. Vasquez, and J. M. Guerrero, "Secondary Control for Voltage Quality Enhancement in Microgrids," *IEEE Transactions on Smart Grid,* vol. 3, no. 4, pp. 1893-1902, 2012.

[128] H. Bevrani, M. R. Feizi, and S. Ataee, "Robust Frequency Control in an Islanded Microgrid:Synthesis Approaches," *IEEE Transactions on Smart Grid,* vol. 7, no. 2, pp. 706-717, 2016.

[129] Z. Yi, Y. Xu, W. Gu, and Z. Fei, "Distributed Model Predictive Control Based Secondary Frequency Regulation for a Microgrid With Massive Distributed Resources," *IEEE Transactions on Sustainable Energy,* vol. 12, no. 2, pp. 1078-1089, 2021.

[130] E. A. Coelho, D. Wu, J. M. Guerrero, J. C. Vasquez, T. Dragičević, C. Stefanović, and P. Popovski, "Small-Signal Analysis of the Microgrid Secondary Control Considering a Communication Time Delay," *IEEE Transactions on Industrial Electronics,* vol. 63, no. 10, pp. 6257-6269, 2016.

[131] G. Lou, W. Gu, X. Lu, Y. Xu, and H. Hong, "Distributed Secondary Voltage Control in Islanded Microgrids With Consideration of Communication Network and Time Delays," *IEEE Transactions on Smart Grid,* vol. 11, no. 5, pp. 3702-3715, 2020.

[132] S. Golestan, M. Monfared, F. D. Freijedo, and J. M. Guerrero, "Design and Tuning of a Modified Power-Based PLL for Single-Phase Grid-Connected Power Conditioning Systems," *IEEE Transactions on Power Electronics,* vol. 27, no. 8, pp. 3639-3650, 2012.

[133] D. Wu, T. Dragicevic, J. C. Vasquez, J. M. Guerrero, and Y. Guan, "Secondary coordinated control of islanded microgrids based on consensus algorithms." pp. 4290-4297.

[134] M. Chen, and X. Xiao, "Hierarchical frequency control strategy of hybrid droop/VSG-based islanded microgrids," *Electric Power Systems Research,* vol. 155, pp. 131-143, 2018/02/01/, 2018.

[135] A. Micallef, M. Apap, C. Spiteri-Staines, J. M. Guerrero, and J. C. Vasquez, "Reactive Power Sharing and Voltage Harmonic Distortion Compensation of Droop Controlled Single Phase Islanded Microgrids," *IEEE Transactions on Smart Grid,* vol. 5, no. 3, pp. 1149-1158, 2014.

[136] X. Zhao, L. Meng, M. Savaghebi, J. C. Vasquez, J. M. Guerrero, and X. Wu, "A dynamic consensus algorithm based low-voltage ride-through operation of power converters in grid-interactive microgrids." pp. 3660-3665.

[137] M. A. Awal, H. Yu, H. Tu, S. M. Lukic, and I. Husain, "Hierarchical Control for Virtual Oscillator Based Grid-Connected and Islanded Microgrids," *IEEE Transactions on Power Electronics,* vol. 35, no. 1, pp. 988-1001, 2020.

[138] O. Palizban, K. Kauhaniemi, and J. M. Guerrero, "Microgrids in active network management—Part I: Hierarchical control, energy storage, virtual power plants, and market participation," *Renewable and Sustainable Energy Reviews,* vol. 36, pp. 428-439, 2014.

[139] K. D. B. K. Vanthournout, E. Haesen, J. V. D. Keybus, G. Deconinck, and R. Belman, "Agora: Distributed Tertiary Control of Distributed Resources," in 15th Power Systems Computation Conference (PSCC15), Liege, Belgium, 2005.

[140] V. N. A. Bidram, A.Davoudi, and F.L Lewis, "Control and Modeling of Microgrids," *Cooperative Synchronization in Distributed Microgrid Control*: Advances in Industrial Control, Springer, Cham, 2017.

[141] J. Rocabert, A. Luna, F. Blaabjerg, and P. Rodríguez, "Control of Power Converters in AC Microgrids," *IEEE Transactions on Power Electronics,* vol. 27, no. 11, pp. 4734-4749, 2012.

[142] F. Delfino, G. Ferro, M. Robba, and M. Rossi, "An architecture for the optimal control of tertiary and secondary levels in small-size islanded microgrids," *International Journal of Electrical Power & Energy Systems,* vol. 103, pp. 75-88, 2018.

[143] Z. Zhang, C. Dou, D. Yue, B. Zhang, and W. Luo, "A decentralized control method for frequency restoration and accurate reactive power sharing in islanded microgrids," *Journal of the Franklin Institute,* vol. 355, no. 17, pp. 8874-8890, 2018.

[144] X. Zhao-xia, Z. Mingke, H. Yu, J. M. Guerrero, and J. C. Vasquez, "Coordinated Primary and Secondary Frequency Support Between Microgrid and Weak Grid," *IEEE Transactions on Sustainable Energy,* vol. 10, no. 4, pp. 1718-1730, 2019.

[145] F. Guo, C. Wen, J. Mao, and Y. D. Song, “Distributed Secondary Voltage and Frequency Restoration Control of Droop-Controlled Inverter-Based Microgrids,” *IEEE Transactions on Industrial Electronics,* vol. 62, no. 7, pp. 4355-4364, 2015.

[146] X. Zhou, L. Zhou, Y. Chen, Z. Shuai, J. M. Guerrero, A. Luo, W. Wu, and L. Yang, “Robust Grid-Current-Feedback Resonance Suppression Method for LCL-Type Grid-Connected Inverter Connected to Weak Grid,” *IEEE Journal of Emerging and Selected Topics in Power Electronics,* vol. 6, no. 4, pp. 2126-2137, 2018.

[147] A. Bendib, A. Kherbachi, A. Chouder, H. Ahmed, and K. Kara, “Advanced control scheme and dynamic phasor modelling of grid-tied droop-controlled inverters,” *IET Renewable Power Generation,* vol. n/a, no. n/a.

[148] M. Castilla, L. G. de Vicuña, and J. Miret, "Control of Power Converters in AC Microgrids," *Microgrids Design and Implementation*, A. C. Zambroni de Souza and M. Castilla, eds., pp. 139-170: Springer Verlag, 2019.

[149] P. Rodriguez, A. Luna, I. Candela, R. Teodorescu, and F. Blaabjerg, "Grid synchronization of power converters using multiple second order generalized integrators." pp. 755-760.

[150] A. Bendib, A. Chouder, K. Kara, A. Kherbachi, S. Barkat, and W. Issa, “New modeling approach of secondary control layer for autonomous single-phase microgrids,” *Journal of the Franklin Institute,* vol. 356, no. 13, pp. 6842-6874, 2019/09/01/, 2019.

[151] A. M. Bouzid, J. M. Guerrero, A. Cheriti, M. Bouhamida, P. Sicard, and M. Benghanem, “A survey on control of electric power distributed generation systems for microgrid applications,” *Renewable and Sustainable Energy Reviews,* vol. 44, pp. 751-766, 2015.

[152] X. Guo, Z. Lu, B. Wang, X. Sun, L. Wang, and J. M. Guerrero, “Dynamic Phasors-Based Modeling and Stability Analysis of Droop-Controlled Inverters for Microgrid Applications,” *IEEE Transactions on Smart Grid,* vol. 5, no. 6, pp. 2980-2987, 2014.

[153] B.-J. Kim, H.-J. Kum, J.-M. Park, and C.-Y. Won, “Analysis, Design and Implementation of Droop-Controlled Parallel-Inverters Using Dynamic Phasor Model and SOGI-FLL in Microgrid Applications,” *Energies,* vol. 11, no. 7, pp. 1683, 2018.

[154] L. Wang, X. Q. Guo, H. R. Gu, W. Y. Wu, and J. M. Guerrero, "Precise modeling based on dynamic phasors for droop-controlled parallel-connected inverters." pp. 475-480.